



UNIVERSITY OF
BIRMINGHAM

From Surface Science to Catalysis:
Lab-Scale Vacuum Deposited Catalyst
Production

Author: Ross Griffin

June 5, 2020

A Thesis Submitted to the University of Birmingham for the
Degree of Doctor of Philosophy

Nanoscale Physics Research Laboratory
in collaboration with Johnson Matthey
University of Birmingham

UNIVERSITY OF
BIRMINGHAM

University of Birmingham Research Archive

e-theses repository

This unpublished thesis/dissertation is copyright of the author and/or third parties. The intellectual property rights of the author or third parties in respect of this work are as defined by The Copyright Designs and Patents Act 1988 or as modified by any successor legislation.

Any use made of information contained in this thesis/dissertation must be in accordance with that legislation and must be properly acknowledged. Further distribution or reproduction in any format is prohibited without the permission of the copyright holder.

Abstract

This thesis outlines the adaptation of surface techniques to nanoparticle catalyst production. The work covers the scale up of the Matrix Assembly Cluster Source (MACS), the design and development of new apparatus, dubbed the Clean Catalyst Source (CCS) and the effectiveness of catalysts produced by these systems. All samples are characterised using atomic resolution Scanning Transmission Electron Microscopy (STEM). Produced catalysts are compared to those produced by Incipient Wetness Impregnation (IWI) as a model chemical synthesis method where appropriate to highlight the differences between in-vacuum and conventional solvent based production methods.

MACS produced Gold and palladium clusters are deposited onto alumina and silica powders using the MACS producing ~1g of catalyst. Produced samples are tested for their activity in the oxidation of carbon monoxide, the reduction of 4-nitrophenol to 4-aminophenol in the presence of sodium borohydride, and the selective hydrogenation of 1-pentyne to 1-pentene as desired. All samples demonstrate activity for these reactions with the exception of gold for hydrogenation. MACS samples demonstrate similar activities to impregnated analogues at far lower loadings with cluster beam samples demonstrating high (95%) selectivity to the production of 1-pentene. Samples deposited using the MACS without matrix formation i.e; atomic rather than cluster deposition demonstrate similar structures and indistinguishable catalytic behaviour.

As a result of this similar behaviour, a new apparatus was developed and its design; based on direct sputtering of metals onto oxide powders is presented. The system uses a 10mA, 600V ion source to sputter a 150x150mm metal foil target onto a piezo fluidised bed of support particles. These are tipped between covered hoppers to ensure even coating over multiple depositions. 3g of support is coated in 5 minutes, producing $\sim 1.1 \pm 0.4nm$ metal clusters by surface agglomeration. Binary palladium copper particles are produced by sequential deposition and found to be alloyed with a metallic ratio standard deviation of 0.2. This value can be halved by co-sputtering of compound (as opposed to alloyed) targets, but is not pursued due to the decreased flexibility of such systems. Samples are tested for their activity in the oxidation of carbon monoxide and the selective hydrogenation of 1-pentyne. CCS samples demonstrate similar light off temperatures and selectivities for these reactions when compared with MACS samples indicating that the in-vacuum or solvent free formation is dictating catalyst behaviour, as opposed to the cluster formation. Addition of copper to palladium samples results in a small decrease in selectivity contrary to expectations. Minor differences in catalytic behaviour were seen in $\sim 20\%$ Cu binary particles across other test reactions.

Finally a molybdenum sublayer is used as a surface modifier to produce molybdenum nucleated, molybdenum surrounded and molybdenum supported palladium nanoparticles, using a $10m^2g^{-1}$ alumina support. These samples were tested for their active surface area using carbon monoxide chemisorption and their retention of hydrogen through temperature programmed desorption. Samples are also tested for their activity in the oxidation of carbon

monoxide and the selective hydrogenation of 1-pentyne. Samples demonstrate high (95%) selectivity to the formation of 1-pentene as seen previously. Molybdenum containing structures demonstrate a slight activity suppression and associated selectivity increase. Molybdenum surrounded and nucleated particles demonstrate an increased resistance to sintering with little effect on catalytic activity. This work demonstrates the use of a simple technique to quickly produce large (across $30m^2$) structures for lab scale catalytic testing.

Acknowledgements

I would like to thank my supervisor, Dr Quanmin Guo for taking me on as a student, enabling me to continue my postgraduate studies, as well as for his help and guidance throughout the research.

I would like to thank Dr Laura Ashfield for her supervision, advice and access to the facilities at Johnson Matthey, Sonning Common.

I would like to thank Dr Peter Ellis for his supervision, introduction to Johnson Matthey and his many patient explanations of the world of heterogeneous catalysis. I feel we can finally speak the same language on some of these topics.

I would like to thank Prof. Richard Palmer for persuading me to pursue, and later accepting me for a PhD position.

I would like to thank Dr Wolfgang Theis for our many discussions on a wide range of scientific topics, all interesting, some even relevant.

I thank Chris Brown for his technical expertise on everything involving catalytic testing and chemical synthesis of catalysts and his seemingly infinite patience with my desires for various tests and equipment. I am very grateful for his work, knowledge and company during my secondments to JM.

I would like to thank Dr Peter (J) Ellis for his assistance and knowledge of chemisorption techniques as well as for access to his lab and equipment at JMTC.

I would like to thank my mentors at NPRL: Dr William Terry, Dr Lu Cao and Dr Vitor Oiko, though all have since moved on to new projects,

your assistance in the early stages of this work was as much appreciated as the life lessons for surviving the academic world.

Finally, I would like to thank my colleagues and friends at NPRL for their friendship and many excellent (scientific or otherwise) debates throughout the course of the PhD, I wish you all the greatest success, whatever your futures may hold. I would specifically like to thank Patrick Harrison and Alex Pattison for playing devil's advocate, and helping me talk my way through problems.

Contents

1	Introduction	4
2	Background	7
2.1	Cluster Sources	7
2.1.1	Gas Condensation Magnetron Cluster Sources	8
2.1.2	Laser Ablation Cluster Sources	10
2.1.3	Matrix Assembly Cluster Source (MACS)	12
2.2	Heterogeneous Catalysts	17
2.2.1	Choice of Metal	18
2.2.2	Choice of Support	19
2.2.3	Test Reactions	21
2.3	Direct Atomic Deposition	28
2.3.1	Sputter Coating	29
2.3.2	Surface Agglomeration	30
2.3.3	Thin Film Catalysis	33
2.3.4	Powder Fluidisation	33
2.3.5	High Current Ion Sources for Thin Film Deposition	34
2.4	Scanning Transmission Electron Microscopy	37
2.4.1	Equipment	37
2.4.2	Image Analysis	39
2.5	Chemical Analysis	42
2.5.1	Inductively Coupled Plasma Mass Spectroscopy	43
2.5.2	Temperature Programmed Desorption	45
2.5.3	Chemisorption Testing	46
3	Formation of catalysts using the Matrix Assembly Cluster Source	48
3.1	Introduction	48
3.2	Experimental Setup	49
3.2.1	MACS Instrument	49
3.2.2	MACS Parameters	51

3.3	MACS Flux	52
3.3.1	Beam Shape	52
3.3.2	Flux Measurement	53
3.4	Sample Production and STEM Analysis	54
3.4.1	Gold on Alumina	54
3.4.2	Gold on Silica	56
3.4.3	Palladium on Alumina	57
3.4.4	Palladium on Silica	57
3.4.5	Sample Summary	58
3.5	Loading	59
3.5.1	Impregnated Material	61
3.5.2	Agitation Effects	61
3.6	Catalysis Results	62
3.6.1	Carbon Monoxide Oxidation	63
3.6.2	4-Nitrophenol Reduction	65
3.6.3	Selective hydrogenation of 1-Pentyne	67
3.7	Post Catalysis Analysis	69
3.8	Matrix-less deposition	71
3.9	Summary and Conclusion	75
4	The Clean Catalyst Source	79
4.1	Introduction	79
4.2	Initial tests	80
4.2.1	Equipment	80
4.2.2	Test Samples	82
4.3	The Clean Catalyst Source Design	88
4.3.1	Target	88
4.3.2	Powder Tray	90
4.3.3	Full System Set up	94
4.4	Standard Operating Procedure	95
4.4.1	Inserting Powdered Support	95
4.4.2	Pumping Down	97
4.4.3	Deposition	97
4.4.4	Venting	98
4.4.5	Retrieving Sample	99
4.5	System Characterisation	99
4.6	Initial Samples	101
4.6.1	Method Refinement	101
4.6.2	Monometallic Homogeneity	103
4.6.3	Binary Homogeneity	104
4.7	Catalytic Testing	107

4.7.1	Carbon Monoxide Oxidation	110
4.7.2	1-Pentyne Hydrogenation	114
4.8	Conclusion	117
5	Molybdenum Palladium Alloys	121
5.1	Sample Production	123
5.1.1	TEM Grid Depositions	123
5.1.2	Glass Ground Supports	126
5.1.3	Catalyst Formation	127
5.1.4	Sample Summary	132
5.2	Surface Area Testing	133
5.2.1	Temperature Programmed Desorption of Hydrogen	134
5.2.2	Chemisorption of Carbon Monoxide	136
5.3	Catalyst Damage	138
5.4	Catalysis	144
5.4.1	Carbon Monoxide Oxidation	144
5.4.2	1-Pentyne Hydrogenation	146
5.5	Summary and Conclusion	147
6	Conclusions	151

Chapter 1

Introduction

Catalysis is a vital part of human industrial processes, it is likely that every single synthetic item in view of the reader has come into contact with a catalyst at some point during its formation. For the vast majority of catalytic research, catalysts have been discovered by a process of informed trial and error based on extensive literature and general catalysis theory. While this method is no doubt effective, it would be far more desirable to design a catalyst, simulated or otherwise, produce it and have it perform as intended. While this is certainly performed with reasonable effectiveness, it is far from the most efficient method, and in general it is still more efficient to produce a range of catalysts and simply test them for a given application. In pursuit of ‘catalysis by design’, techniques that promise further control over catalyst production are being pursued. In order to gain such control, we may look to surface science and nanotechnology, both fields that have experience manipulating structures on the nanoscale. As a result of this physicists have been turning their attention to the ‘black art’ of catalysis for the past

twenty years[1]. Such work requires collaboration between fields as well as a re-calibration of what is required in terms of equipment, moving from the microscopic realm of physics to the generally macroscopic realm of catalysis.

A primary challenge in catalysis is that of specificity: a model catalyst for a specific reaction in highly specific conditions is of as little interest in the real world as a generic catalyst that achieves middling performance over a wide range of reactions. As such, the field is generally divided into generic microscopic analysis of component reactions[2, 3, 4] and macroscopic catalyst production that may make gestures to the microscopic interpretation but naturally focus on their final catalytic performance[5, 6]. Catalysts for these studies are consistently produced by entirely separate methods, notably direct deposition in vacuum for microscopic fields and solvent based chemical synthesis for macroscopic analysis. As such there are likely disparities between these samples, in particular at interface or defect sites where solvent anions may remain. There may also be effects caused by (lack of) the solvent's liquid flow properties[7] or by the deposition of ionic vs neutral species [8]. In recent years, and within the collaborations of our work, efforts have been made to scale up the cluster flux of cluster sources in order to apply the expertise developed in the microscopic realm of cluster physics[9, 10, 8, 11, 12]. It should be noted that the work discussed here; scaling up from microscopic methods, is performed only due to the authors' backgrounds. The process of scaling down the production of catalysts and analysing their microscopic properties; surface chemistry, is a similar field approached from the opposite direction[13, 14].

These methods, often alongside computer modelling[15] directly or oth-

erwise, serve the goal of catalysis by design. In recent years, with the advent of more powerful modelling methods, microscopy techniques and an enormous backlog of data we are moving towards a more informed mode of catalyst production, which, at the very least will provide potentially useful alternatives to existing methodology. It is hoped that on the evidence of this work, and others like it that physical deposition methods will find their place alongside the aforementioned methodology in catalyst production and testing.

The most common ‘surface science come catalyst production’ method is cluster deposition. As such, a cluster source specifically designed to scale up production is the starting point of this work. This source is used to produce palladium and gold clusters on silica and alumina powders to make simple catalysts. These are tested for their activity in carbon monoxide oxidation, the selective hydrogenation of 1-pentyne and the reduction of 4-nitrophenol by sodium borohydride. The project then transitions to a direct sputtering, atomic deposition method, relying on surface agglomeration for cluster formation. A new system is designed, built and used to produce palladium and palladium/copper binary particles on alumina at a similar scale to the cluster source system. The catalytic behaviour of these samples is measured and compared with those produced by the cluster source. Finally the direct deposition system is used to produce differing surface structures by modification of the alumina support with molybdenum prior to palladium deposition. Once again, these catalysts are tested for catalytic response, and compared to previous samples.

Chapter 2

Background

2.1 Cluster Sources

Nanoscale cluster physics is a branch of research involved in the production and characterisation of two to ten thousand atom structures. These structures are usually on the order of a few nanometers diameter and possess a variety of structures, though most commonly seen are high N (~ 20) polyhedra[16, 17]. Throughout this thesis and available literature, nanoscale clusters are referred to almost interchangeably as ‘clusters’ (Physics) or ‘nanoparticles’ (Chemistry). As cluster physics generally is interested in the simplest possible structures, ‘cluster’ generally refers to smaller $< 2nm$ particles, while ‘nanoparticles’ is used generally to describe all sub micron particles.

Cluster sources are many and varied, though most adhere to the principle of atomising a bulk material and condensing it to form clusters in the gas phase. Few limits are set on material choice for cluster formation, as the methods used are primarily physical: laser ablation, thermal evaporation,

physical sputtering using noble gases and so on. As these processes are usually performed in a high vacuum environment, and the processes themselves broadly inert, very little chemical contamination can occur during production. Differences between cluster sources vary greatly, specialising them for their individual roles in research. The major categories of cluster source are covered here: laser ablation and magnetron sputtering. Examples of sources that have been adapted for catalyst production are focused on.

2.1.1 Gas Condensation Magnetron Cluster Sources

Magnetron based cluster sources are some of the most commonly used due to their high sputter rates and flexibility. Magnetron ‘heads’ comprise of a solid target sputtered by a plasma of heavy gas, most commonly argon which is generated by a large DC or radio frequency (for insulating targets) electric field [9]. Plasma density is intensified by a multi-pole permanent or electro-magnet, placed behind the target, which causes charged particles to follow helical paths around the magnetic field lines, confining them close to the surface of the target. This results in uneven ‘racetrack’ wear of the target at the poles of the magnetic field. Efforts have been made to reduce this by producing the plasma in separate chambers before impacting the surface of the target, for a ‘High Target Utilization Sputtering’ method [18]. However due to the increased complexity, required chamber design, as well as the insignificant change in produced samples, this technology has not been widely adopted in the scientific community. The first magnetron sources as we would recognise them today were reported in 1986 [19] and are

now used for most cluster sources such as the one used in related work [9] by other authors[10, 20, 21]. The produced sputtered metal must be cooled and undergo metal/metal collisions in the gas phase to form clusters. This process is referred to as condensation. Clusters produced by such systems are condensed in the same chamber as the magnetron plasma and thus are predominantly charged by ion interaction. This allows for E-field manipulation and mass selection by mass filters such as the parallel plate design seen in figure 2.1[22].

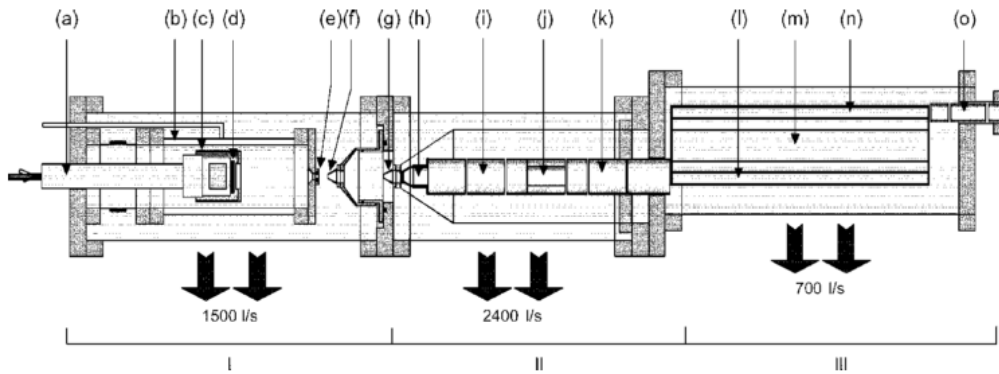


Figure 2.1: An example of a gas condensation, mass selecting magnetron cluster source, reproduced from [9], showing (a) magnetron mount, (b) liquid nitrogen chamber (c) dark space shield, (d) sputtering target, (e) adjustable nozzle (f) skimmer, (g) skimmer, (h) extraction lens, (i) first einzel lens, (j) deflection plates, (k) second einzel lens, (l) TOF mass filter acceleration region, (m) TOF field free region, (n) TOF deceleration region, (o) third einzel lens.

Systems such as this are used primarily for the investigation of the fundamental properties of nano-scale clusters, however due to the extended passage of the cluster beam ($\sim 5\text{m}$), the multiple skimming apertures required to form a beam rather than a ‘spray’ and finally the size selection which simply removes all clusters that do not fit the size requirement, the final cluster

beam equates to only $\sim 1.5 \times 10^{-8}$ g per hour. This would require approximately a year of continual operation to deposit the quantity of metal used for samples in this work. By removing the size selection and designing a shorter travel system, the rate can be brought up to approximately 1×10^{-4} g per hour[23, 24]. Such systems can be used to produce catalysts that are active on the scale laboratory experimentation.

2.1.2 Laser Ablation Cluster Sources

Another method of liberating atoms from bulk material is the process of laser ablation. A high intensity laser excites free electrons via the inverse Bremsstrahlung process. Energy is transferred through multiple electronic transitions to the lattice, breaking bonds and forming a plasma of atomised material at the surface of the target[25]. This metallic plasma can be condensed into clusters, usually by the pulsed introduction of gas. Such a system is usually described as a pulsed laser ablation cluster source or PLA. Laser ablation is not restricted to a high vacuum environment as many sputtering systems are, and as such it is possible to perform in a liquid medium[26]. In such a system, the choice of liquid determines the aggregation of clusters, and there is somewhat less control over the process as there may be in vacuum based gas-condensation systems such as[27].

The individual designs of such cluster sources varies from instrument to instrument, but most use a high power *ps*, *fs* or constant laser to ablate a target. Gas is then introduced (pulsed or constant) to condense clusters and transport them away from the target. In the example shown in figure

2.2 a conical nozzle allows for supersonic gas expansion, forming a spray of clusters. Off axis clusters are removed with a skimmer to form a cluster beam.

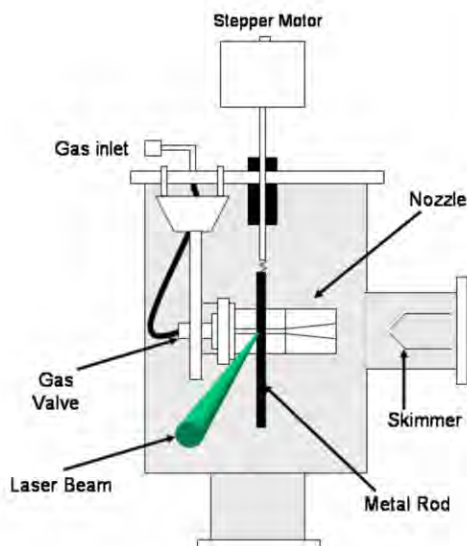


Figure 2.2: An example of a gas condensation pulsed laser ablation cluster source, reproduced from [27] showing a target rod externally mounted laser, pulsed gas valve, expansion nozzle and collimating skimmer. The cluster source shown here is used in conjunction with a quadropole mass filter and cluster beam ion optics in-situ investigations in a second chamber.

Control over such a source is achieved by tuning the gas pulses' length and intensity, as well as the gas used. A higher heat capacity will initiate faster agglomeration and larger cluster sizes. The source shown in figure 2.2 can be tuned to produce an average cluster size of two to one hundred atoms, restricting it to exceptionally small clusters. Production of charged clusters makes this a flexible method for mass selection and deposition energy variation. These sources have been used to create catalysts[28], however appear to retain issues of low flux in the main.

2.1.3 Matrix Assembly Cluster Source (MACS)

[†]The MACS is a cluster source based on the formation of a compound matrix of condensed solid gas (i.e: $Ar_{(s)}$ @ 17K) and cluster material; attempting to combine the atomisation and condensation steps into a single sputtering process. As all cluster material used for this work was metal, it will be referred to as metal for the remainder of the project, though there is no reason why non-metals could not be used with this method.

In order to condense the matrix, a copper plate is cooled to ~ 20 K while inert gas (Ar in normal usage) and metal are co-condensed onto the plate. The gas is leaked into the chamber and condenses from vapour, while the metal is thermally evaporated. This forms a gas/metal matrix. The matrix is then sputtered by Ar^+ ions at 1-3keV. Clusters are ripened and released during the sputtering process.

Operating Theory

While still up for debate, the full theory of operation is that metal atoms land on the matrix of solid argon and diffuse on the surface, forming small seed clusters that are enveloped by condensing argon. Figure 2.3 shows the operation of the MACS in both transmission and reflection modes, where the clusters are collected from the ‘transmission’ of momentum through or ‘reflection’ of ions off the matrix respectively.

During sputtering, two main processes occur: a collision cascade and

[†]Due to the recent and disrupted nature of this work, few published resources exist. Much of this section references two previous PhD theses from the group[29, 30] and two papers[23, 31]. These are the best resources for further reading.

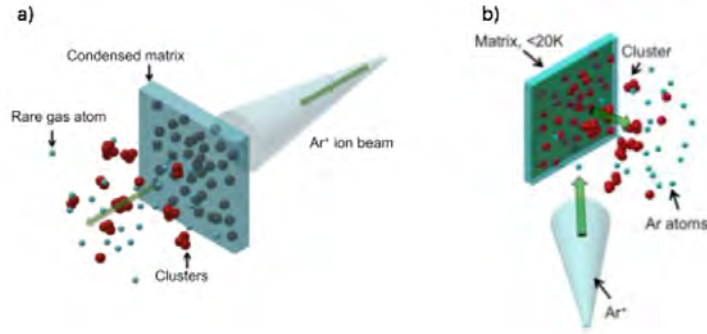


Figure 2.3: Two modes of operation for the MACS. Reproduced from [29]. Transmission mode (a) uses a quantifoil grid of $1.3 - 25\mu\text{m}$ wide bars, separating $1.2 - 37\mu\text{m}$ holes as the matrix support. Reflection mode uses a Cu plate and clusters are ejected normal to the plate

thermal spike [32, 33]. The collision cascade serves to rearrange the matrix. Metal/metal collisions cause further aggregation, ripening small clusters and forming new seed clusters. Larger clusters present in the matrix may be damaged by impact, but this is considered negligible as the majority of atoms affected by a collision cascade are at low energy, as the shock-wave spreads through the material. Furthermore, direct ion-cluster collision at high energy is statistically unlikely due to the low concentration of metal in the matrix. A thermal spike also occurs around the point of ion impact, causing local matrix sublimation. This sublimation causes a pressure spike, ejecting a small amount of material. This forms the cluster ‘spray’ in reflection mode.

While this document focuses on reflection mode, as this was the mode used throughout the work shown here, the MACS was developed in transmission mode. In transmission mode, the matrix is built on a quantifoil grid, such that the solid Ar may span the grid vacancies. A range of quantifoil grid geometries can be used in order to maximise either the transmission (hole to bar ratio) or to maximise matrix vacancy coverage. In transmission mode,

clusters that are ejected must pass through the matrix or at least acquire momentum from ions to be ejected. As such produced clusters must have travelled through the matrix, likely acquiring further atoms to form small clusters. While glancing sputtering off the edges of the quantifoil is also likely to release some material, a collimated ion beam should restrict this.

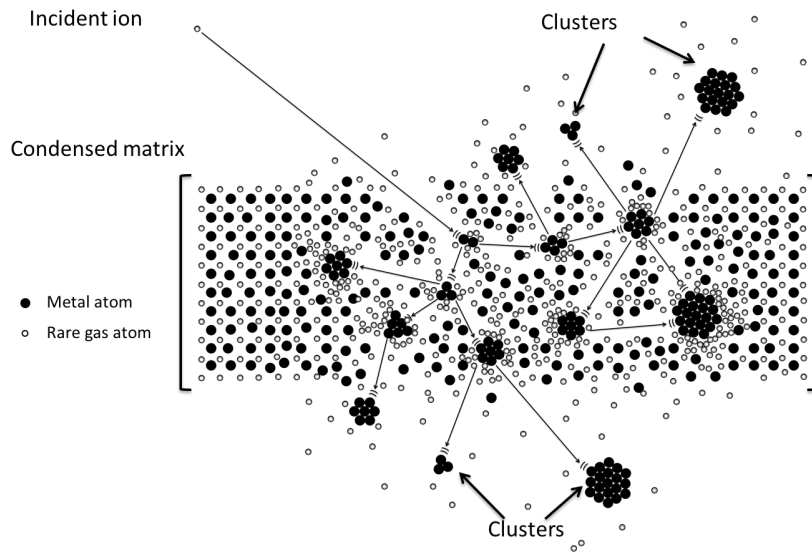


Figure 2.4: Diagram demonstrating an example of an ion induced collision cascade through a matrix, ripening and expelling rare gas, metal atoms and clusters. The matrix shown is a representation; matrices will be disordered and have low metal concentration. Reproduced from [29]

Figure 2.4 shows a representation of a collision cascade within the matrix, illustrating the processes discussed here.

Clusters produced by the MACS are primarily uncharged, with 16% positively charged, and 13% negatively charged[29], making the source more suited to direct deposition, rather than mass selection, which would require a secondary, non-interfering ionisation step before the cluster beam could be manipulated. The lack of natural charge, and the relatively even posi-

tive/negative split between charge carriers serves to decrease charging effects when depositing onto insulating supports.

Size Control

Due to the uncharged nature of MACS clusters and the desire for high cluster flux, mass selection similar to those described earlier in this section is undesirable. In many systems the mean size of clusters can be tuned by adjusting the condensation parameters. In the MACS unit these are determined by the concentration of metal in the matrix. Increased metal concentration leads to an increased likelihood of metal/metal collisions and hence formation of clusters in both the condensation and sputtering phases of production, producing larger clusters on average. By considering the impingement rate of gas atoms on a surface and the deposition rate of metal atoms (equations 2.1 and 2.2 respectively), we derive an equation for the matrix loading. A sticking coefficient of 1 is assumed for both gas and metal.

$$\Gamma_g = \frac{P}{\sqrt{2\pi m_g k_b T_g}} \quad (2.1)$$

$$\Gamma_m = \frac{\nu \rho_m}{m_m} \quad (2.2)$$

$$\text{Matrix Loading} = \frac{\Gamma_m}{\Gamma_m + \Gamma_g} = \frac{\frac{\nu \rho_m}{m_m}}{\frac{\nu \rho_m}{m_m} + \frac{P}{\sqrt{2\pi m_g k_b T_g}}} \quad (2.3)$$

Γ_g is the flux of gas atoms, P is the pressure, m_g is the atomic/molecular mass of the gas, k_b is the Boltzmann constant and T_g is the gas temperature.

Γ_m is the deposited flux of metal atoms, ν is the vertical metal deposition rate in ms^{-1} , ρ_m is the metal's density and m_m is the atomic mass of the metal in question. The matrix loading is calculated as a fractional atomic composition, usually quoted as a percentage of metal. The relationship between metal matrix loading and produced cluster size has been published in [31] and is reproduced in figure 2.5

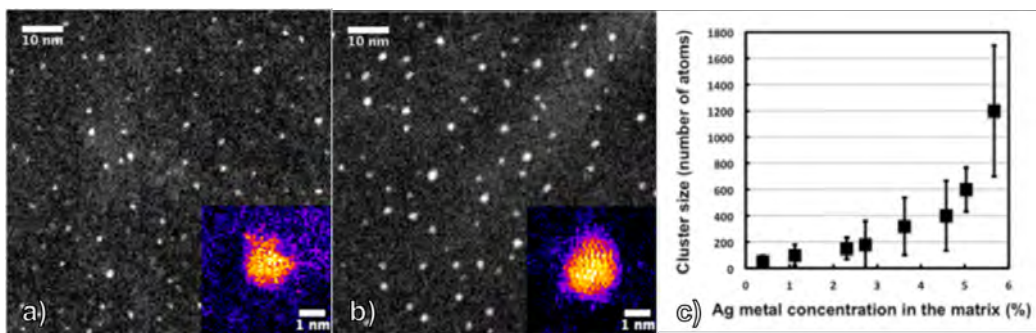


Figure 2.5: Reproduced from [31] showing examples of silver clusters produced by matrices of different loadings. a) Shows clusters from a 2.3% Ag matrix. b) Shows clusters from a 3.6% Ag matrix. c) Shows the dependence of cluster size on matrix loading. Cluster size is a numerical average and error is quoted from distribution width. *NB: This work was done in transmission mode.*

Thanks to the scalability and size control of the MACS method it appears to be well suited to the production of lab-scale quantities of catalyst for the assessment of macroscopic catalytic activity of small clusters. Size distributions were shown to become bi-modal at higher matrix loadings [29], making these unsuitable for model catalyst production.

2.2 Heterogeneous Catalysts

Catalytic materials in general are far too varied and extensive to list here but vary from bulk surfaces[2] to thin films[34] to nano-structured surfaces[35]. Moving towards atomic dimensions we see cluster based catalysts over a wide range of sizes. Cluster catalysts consist of clusters mounted on a broadly inert support for stabilisation and catalyst optimisation. Clusters are usually metallic and supports are usually oxides or carbonic, though many variations exist. Large ($\sim 100\text{nm}$) clusters take advantage of the increased surface area/volume ratio that such a distribution of material results in when compared to the bulk, while smaller clusters also manipulate the electronic structure, atomic coordination and hence bonding characteristics of the reaction[36]. At smaller sizes we move onto mono-atomic catalysts[37]. The extent to which single atoms partake in a reaction is a topic for debate, and naturally reaction specific, but they must be considered in many systems due to the rate of detachment and re-attachment from cluster material under reaction conditions. This effect is particularly obvious under the bombardment of an electron beam in an electron microscope, similar to thermal conditions of $\sim 250^\circ\text{C}$ [38]. Zeolites and enzymes may not fit into this catalysis ‘scale’ neatly, but must also be mentioned here. While zeolitic catalysts often work in similar ways to standard catalysts, their size tunable porous structure allows for selectivity enhancement in similar ways to the ‘lock and key’ model as enzymes[39]. Enzymes themselves while usually considered homogeneous can demonstrate heterogeneous properties, and can be immobilised for use as pseudo-heterogeneous catalysts[40]. The work presented in

this thesis focuses on metal/metal oxide heterogeneous cluster catalysts, and as such, these are what will be discussed from now.

2.2.1 Choice of Metal

A coarse method of manipulating a catalyst's performance is to change the cluster material. Many metals are only active for a few reactions, and as such improvements in catalysis of a single reaction usually come from metals of the same group, or others with similar properties. For fine tuning of a catalyst's activity, a secondary metal may be added at varying quantities to tune a desired or tune out an undesired property of a catalyst. In this work silver, gold and palladium are used, primarily for convenience rather than specific catalytic properties. Silver is a useful material for testing, being comparatively cheap, noble and having a fairly low melting point for thermal evaporation. This makes it an ideal metal for initial production and imaging. Silver based catalysts have been shown to be active in carbon monoxide oxidation[41], and 4-nitrophenol reduction[42]. These are often present in reduction catalysts and occasionally used as additions for hydrogenation catalysts[43], though usually with a Platinum Group Metal (PGM) as the active component. Gold is used in this work for its high mass, thus high contrast in HAADF-STEM, and highly inert nature. This makes it ideal for production, storage and in depth characterisation of samples. Gold is also a fairly common catalytic material, enabling access to literature for material analyses[44, 45]. Finally palladium is used for sample creation. Palladium is the lowest melting point PGM, making it the easiest to work with

for these purposes, and as with many PGMs is an active catalyst for many reactions due to its ability to activate H_2 in hydrogenation[46, 47], and O_2 in oxidation[48, 49].

2.2.2 Choice of Support

The choice of support is of critical importance to the formation stage of a catalyst, particularly in the case of wet chemical methods [50], and remains of key importance during its use [51]. However, supports are often chosen for their physical properties as required by the reactor or their surface area or porosity.

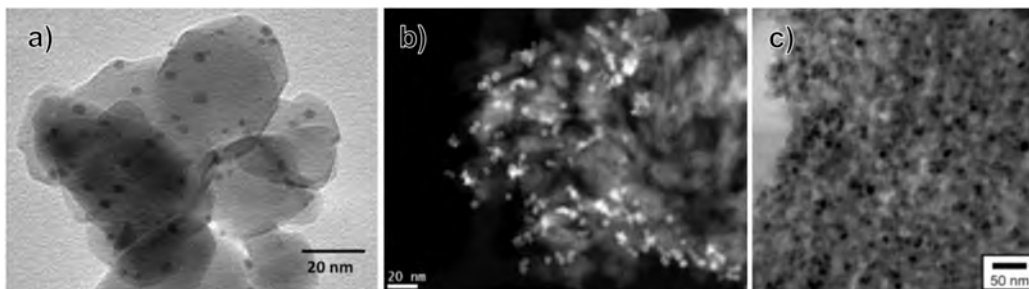


Figure 2.6: Examples of electron microscopy images of catalytic materials showing a) gold clusters on a titanium oxide support [52] (TEM), b) Platinum/Tin binary clusters deposited on γ -alumina [23] (HAADF-STEM) and c) Platinum/Cobalt binary clusters deposited on silica [53](BF-STEM)

There are many factors to consider when selecting a support, though final catalytic performance is of primary importance. As discussed, the support may have a significant effect on the performance of the catalyst, and reaction mechanisms are often proposed at the cluster/support interface[54]. In certain cases the support donates oxygen to the reactants[42] and as such the oxygen affinity of the support will affect the rate of the reaction, hence

the prevalence of cerium oxides as a support[55].

The physical behaviour of the support may also indirectly affect its activity in many real world reactors. A support that fluidises well may present a greater effective active area than a support that agglomerates. Systems that rely on agitation for deposition onto powders require suitable supports that agitate well and allow for a homogeneous deposition across the powder's surface. The support's thermal conductivity and physical strength are also important considerations in larger reactors.

Metal Loading

Finally we must consider a support's surface area. A larger surface area will allow for a greater loading, dependent on cluster size. As the methods illustrated throughout this work are based on line of sight deposition, porosity in supports is undesirable. This highlights one of the major weaknesses of these in-vacuum methods; high activity catalysts in many areas have high loading of the order of 5% , requiring high surface area supports, usually achieved by high porosity[56]. The natural way to achieve a high surface area in non-porous supports is to decrease the particle size, but this often results in the powder becoming difficult to work with. Low mass particles are more likely to agitate out of an open container, and are more vulnerable to charging effects. By making a few assumptions we can put approximate numbers on the maximal loading achievable for a given support particle size. The assumptions used here are that a metal cluster takes up a circular area of radius twice that of the cluster itself, allowing for separated, non aggregating clusters. Assuming spherical clusters and support particles and that cluster

density is approximately equal to bulk metal density, an order of magnitude estimate of the maximal loading can be made:

$$M_c = \frac{4}{3}\pi r_c^3 \rho_c \quad M_s = \frac{4}{3}\pi r_s^3 \rho_s \quad N_c = \frac{1}{2} \frac{4\pi r_s^2}{\pi r_c^2}$$

$$Loading_{max} = \frac{M_c N_c}{M_s} = \frac{8r_c \rho_c}{r_s \rho_s} \quad (2.4)$$

where M_c is the mass of a cluster, M_s is the mass of a support particle, r_c is the mean cluster radius, r_s is the mean support particle radius, and ρ_c and ρ_s are the cluster material and support densities, respectively. As we can see from equation 2.4, the maximal fractional loading scales linearly with the cluster size and the inverse of the support particle size. As cluster surface area scales by r_c^2 , increasing cluster size has a negative impact on the maximum achievable active area. If one considers the active area to be the perimeter interface $\propto r_c$, the effect of cluster size disappears. This leaves the support particle size as the primary dictating factor in metal loading. Applying some reasonable values to these equations for a palladium/alumina sample with support diameter of twenty microns and a cluster diameter of two nanometers, the maximal loading becomes approximately 0.25wt%. This is comparatively low, with catalysts typically residing in the 1% to 5% range.

2.2.3 Test Reactions

Test reactions can be an almost limitless range of standard chemical reactions performed in the presence of a catalyst. While catalytic reaction mechanisms

vary from reaction to reaction, most reactions can be said to follow the ‘active site’ model of catalysis where reactant(s) bond to the catalyst’s active site, react together, form a product, and desorb. This alternate reaction pathway has a lower activation energy and hence can occur at lower temperatures, or simply run faster. The active site of a catalyst is simply the point which possesses the optimal energy of adsorption to allow reactants to adsorb and products to desorb. An adsorption energy that is too low will mean that the reactants will not adsorb under the desired thermal conditions. An adsorption energy that is too high will mean that reactants, products or contaminants bond too strongly to allow further reactants to adsorb and take their place. This gives rise to the standard ‘volcano plot’ for catalyst activity (figure 2.7).

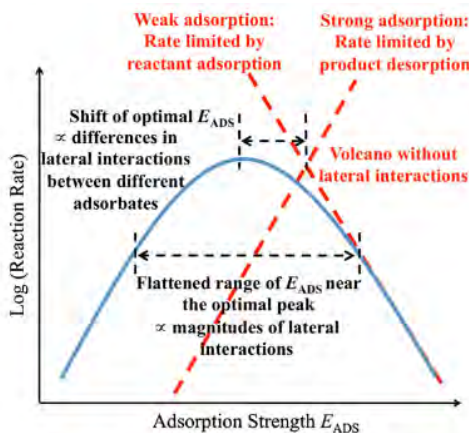


Figure 2.7: An example of the standard ‘volcano plot’ for catalytic activity, reproduced from [57] showing how the difference in adsorption strength classically affects the reaction rate and how the differing adsorption of reactants and products can shift the optimal adsorption strength

Catalytic performance consists of activity and selectivity, and the ability to retain these properties over time: durability. Catalytic activity is generally

quoted as the percentage conversion of the reactant, however this is highly dependent on the reactor in question, and is, as such, only a valid measurement when similar reactions are carefully controlled. In order to generalise catalytic activity, it can be normalised by the total quantity of metal, or the total number of surface atoms. Which of these normalisation methods used will be case dependent, whether energetic or surface area effects are being investigated. Selectivity is simply the ratio of desired product to total conversion, and is thus far more reaction dependent.

Carbon Monoxide Oxidation

The oxidation of carbon monoxide is possibly one of the most universally studied reactions[52, 41, 58, 42]. Being a relatively simple, single product reaction makes it an ideal model for testing catalyst activity, and is used as such. There are also applications in automotive and industrial combustion systems where removal of toxic carbon monoxide is required. Carbon monoxide oxidation in the presence of excess hydrogen[59] is studied for contaminant removal in fuel cell catalysts, and performance tends to improve in wet conditions[55]. These additions would be the natural path of progression for this catalytic testing, but are not covered in this thesis.

A basic understanding of the mechanism of a reaction is essential in result interpretation and is shown in figure 2.8. While it must be noted that the work shown is on gold, the key consideration for all mechanisms is that they rely on adsorbed CO reacting with ‘activated’ monoatomic oxygen. As such the reaction relies on the dual activation of oxygen and CO forming surface CO_2 which then desorbes: a Langmuir-Hinshelwood mechanism[61].

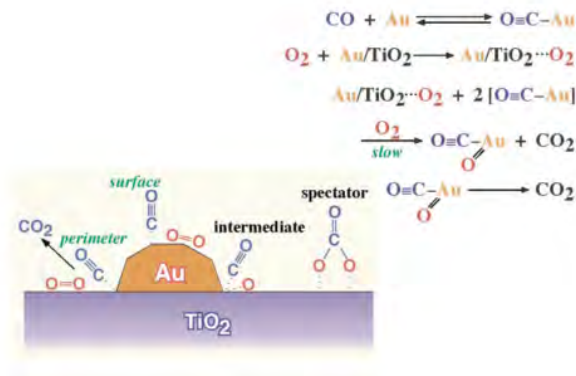


Figure 2.8: Summary the of reaction mechanism for carbon monoxide oxidation on Au at low temperatures, making use of the cluster support interface site. Showing the adsorption of CO onto the Au surface, O_2 activating at the perimeter, and the rate limiting combination of the two species. Reproduced from[60].

The primary difference between gold and palladium is that palladium will activate O_2 on the palladium surface: the support/cluster interface is not required for activity[62, 63, 64].

Gold sits on the other end of this spectrum, generally thought of as too inert to activate oxygen. By use of small clusters and oxide supports this classic inactivity was famously overcome[60]. Due to the reduced energy of adsorption of gold, oxygen does not adsorb to the surface. As such, oxygen is scavenged from the support and replaced from the atmosphere as can be shown by anaerobic reactions[65] or by isotopic labelling as done by Haruta[60].

The exothermic nature of the oxidation of carbon monoxide leads to a positive feedback loop, heating the surface of the catalyst and spiking the reactivity. As with many reactions in usual circumstances this would be the point at which the light off temperature of the catalyst is measured, however

lower activity catalysts may not observe this light off, and hence the method shown in figure 2.9 is used. This method fits the Boltzmann factor to the initial conversion of carbon monoxide:

$$Y = a + e^{k(T-T_0)} \quad (2.5)$$

Equation 2.5 is a simple offset exponential fit, with Y representing the conversion, a being an offset $< 1\%$ to allow for detector drift, k is a fitted constant, T is reaction temperature and T_0 is the light off (1% conversion) temperature. An exponential prefactor is omitted to prevent race conditions during fitting.

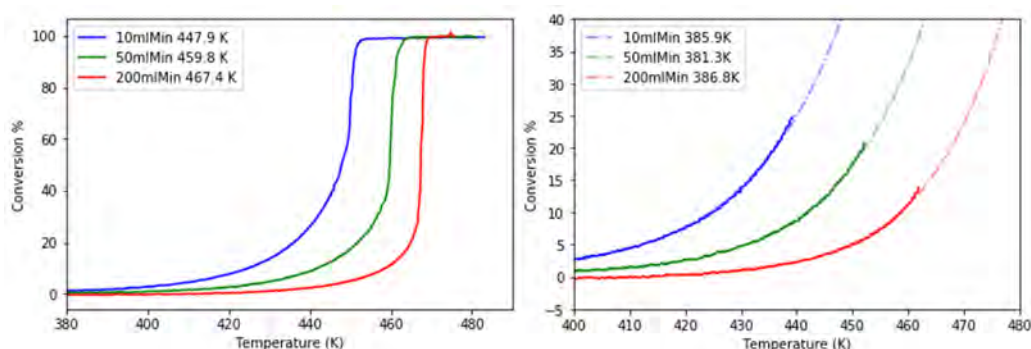


Figure 2.9: The catalytic response of a single impregnated Pd/Al₂O₃ sample at increasing flow rates demonstrating the progress of the reaction (left) and the reduced effect seen by exponential fitting (right). Temperatures given for the overall reaction are listed in the legend, and are the temperatures at which 50% conversion occurs (T50s). Temperatures listed for the fits are offsets for the exponential functions demonstrating a severely reduced spread of values. Data is cut at decreasing intervals due to the differing conversions at which the reactions deviate from the exponential. Fits are scaled, fit and re-scaled to account for flow rate variations.

Fitting exponentials from first principles causes the relationship between flow rate and light off temperature to decrease, assisting in analysis of low

flow rate samples, and offering more insight into the fundamental behaviour of the catalyst. As such, despite the variation in the reaction conditions, light off temperatures remain relatively consistent. It must be mentioned that to achieve this, the data is scaled by the flow rate before fitting such that the light off temperature relates to a set quantity of CO converted, rather than a percentage.

4-Nitrophenol Reduction

Similarly to CO oxidation, 4-nitrophenol reduction is a fairly common benchmark reaction for catalytic testing[66], though usually used for quick tests on exceptionally low loading catalysts due to the relatively simple experimental setup, low equipment requirements and the ability to detect changes in very low concentrations of 4-Nitrophenol. 4-Nitrophenol reduction is performed in the presence of a reducing agent, usually sodium borohydride $NaBH_4$ to provide H^- ions, forming 4-aminophenol. This is done at room temperature in the aqueous phase. the reaction progression is measured by ultraviolet and visible spectroscopy (UV-Vis). This is used to measure the decrease in peak intensity at a wavelength of $400nm$ (4-nitrophenol). 4-Aminophenol also demonstrates a peak in the UV-Vis spectrum at $\sim 300nm$, but due to its relatively low intensity this is not usually quantified, but is confirmed to rise as the reaction progresses.

There are two mechanisms proposed for the reduction of 4-nitrophenol. Khalavka et al.[68] propose a hydride adsorption Eley Rideal method, but a standard Langmuir Hinshelwood reaction is generally accepted[69, 70, 67]. The rate limiting step of this reaction is thought to be the adsorption of the

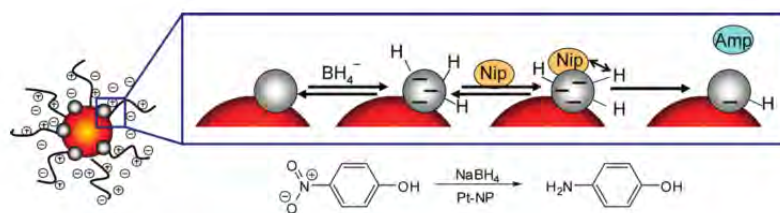


Figure 2.10: The Langmuir - Hinshelwood mechanism for the reduction of 4-*NP* by $NaBH_4$ in the presence of a *Pt* catalyst on a polystyrene support. Nip: Nitrophenol, Amp: Aminophenol. Reproduced from [67]

reactants to the catalyst.

1-Pentyne Hydrogenation

Partial hydrogenation of alkynes is an important industrial consideration, and is a challenging reaction to perform with high selectivity and activity[46]. Also of note is the industrially common hydrogenation of ethyne impurities in ethene feedstock for polymer production, converting contaminant into feedstock[71]. Interest in this reaction lies partially in promising results from cluster beam sources using *Pd*, *PdSn* and *PdTl* on oxide supports in related work[23, 12]

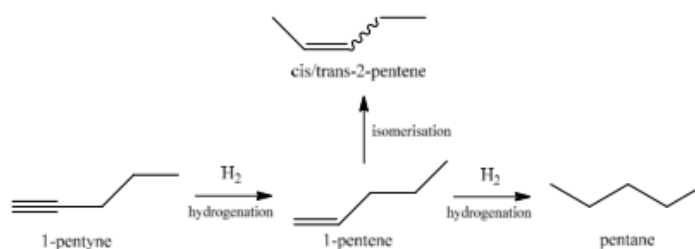


Figure 2.11: The hydrogenation of 1-pentyne to form 1-pentene, geometric isomers of 2-pentene and full hydrogenation to pentane. Reproduced from [23]

Selective hydrogenation of 1-pentyne offers a deeper insight into the

stereo-selectivity of a catalyst due to the possibility of producing cis/trans 2-pentene by migration of the double bond. Specific mechanisms for 1-pentyne hydrogenation are based on the similar ethyne hydrogenation, but all reactions have a varying number of potential mechanisms for explanation of the selectivity, notably from the formation of palladium hydride or carbide underlayers[72, 73] or overlayers[74, 75]. Selectivity in these cases appears to be due to the incorporation of carbon into the Pd lattice[46] in various ways. As such, receptivity of the palladium particles to carbon integration may be the key factor in such reactions' selectivity. Smaller palladium particles may require less carbon laydown to achieve high selectivity[76].

2.3 Direct Atomic Deposition

The methods for the latter half of this work sit between sputter deposited thin film catalysis and cluster deposition. These methods could be described as 'incomplete thin film' catalysis, but these surfaces have much in common with standard deposited clusters of similar size. This qualification is necessary due to the difference in formation of individual clusters. Clusters formed in the gas phase will conform to surface tension and produce spherical particles. On deposition these may deform to varying extents dependent on the materials used, the surface/cluster interaction, deposition energy, deposition temperature and, importantly cluster size. Larger clusters are more likely to fragment on impact, or create surface defects[21]. Smaller $\sim 1\text{nm}$ clusters as dealt with in this work may conform to the surface, forming hemispheres as is observed from the island/cluster formation used for catalyst produc-

tion. It is also worth noting that at least some of the surfaces in the MACS work will be coated in similar ways, as even under ideal working conditions, a number of isolated atoms will be released from the matrix. These will gather around the interface of deposited clusters or nucleate at defect sites, forming island structures as would be produced by atomic (as opposed to cluster) deposition. There is a question to be asked here: is it possible to catalytically distinguish between clusters formed in the gas phase and those formed by surface nucleation/agglomeration? This question becomes more relevant when the standard operating conditions of many catalysts is considered. It is reasonable to assume that clusters' crystalline structures differ between gas and surface formation with the effect of strain produced by the surface's crystal lattice. However, in the range of cluster sizes in this work, the reduced melting point and the harsh environmental conditions required for catalysis appears to be sufficient to induce structural rearrangement both in theory and practice[38, 77, 78]. As such whether these differences remain significant after even a single catalytic cycle is unclear. Based on arguments such as these, it may be possible to create catalysts similar to those produced by cluster deposition techniques quickly and easily, and with greater homogeneity.

2.3.1 Sputter Coating

Much of the historical information about sputter deposition and thin films is translated from two review articles by Greene[79, 80], and these are recommended for historical reading. The earliest vapour deposition systems

appeared in the mid 1600s and were chemical in nature. Due to the vacuum equipment required for sputter deposition as we refer to it in this work, sputter deposition systems did not appear until two centuries later, around the same time thermal evaporation techniques came into use. The initial setup in 1852 using an arc discharge between a steel needle and a silver plate[81] and was initially patented by Thomas Edison in 1894[82]. Sputter coating is the use of the physical momentum of gas particles and (usually, though not exclusively) ions to remove atoms from a surface. The threshold energy for this process is of the order of $30eV$ though naturally this varies somewhat between materials. The magnetron source was developed in the mid 1930s and uses a cathodic target, backed by a magnetic field, usually tripolar, in the geometry of the target. This causes transversely mobile ions to collide with the target, contributing to the sputtering effect. The magnetron has long been used for sputter coating due to its relative ease of use using a high voltage DC plasma (RF may be used, usually for insulating targets) and high sputter rate. While magnetron sputtering remains an attractive and indeed the most commonly used option for many applications there remain limitations. The local plasma is likely to cause charging issues when coating powders. While there are methods to circumvent this[24], they are usually complex and therefore expensive and often wasteful.

2.3.2 Surface Agglomeration

The primary difference between these methods and cluster deposition, as mentioned previously, is the process of agglomeration. In previous work ag-

glomeration was restricted to the matrix, or the gas phase in most other cluster deposition systems, in this work it is limited to the surface of the support. There are generally two modes of agglomeration for such a surface: heterogeneous and homogeneous agglomeration[83, 84]. Heterogeneous agglomeration involves the settling of mobile adatoms predominantly at defects or edge sites. Once settled, these adatoms act as nucleation sites for cluster growth, as more mobile atoms stick to the pinned atom, forming a cluster. Larger clusters become more stable due to their decreased surface energy [85] and more readily accept adatoms. Homogeneous agglomeration is the result of mobile adatom/adatom collisions on the surface, the dimer/trimer now acts as a nucleation site and clusters form around them. In this agglomeration mode, any factor that affects the diffusion length or rate of the adatoms will affect the final surface structure. It is important to note that we must consider the growth mode of material combinations. This depends on the relative binding strengths of the deposited material to the support and itself as shown in figure 2.12.

In cases where the deposited material is more strongly bonded to the surface than itself, a layer-by-layer growth mode occurs, as demonstrated in figure 2.12 (a). This growth mode is most commonly seen in noble gas surface adsorption. In the case where the material to be deposited adheres more strongly to itself than the support, islands appear, either at defect sites or nucleation points (see above). This is represented by figure 2.12 (c). The intermediate layer plus island growth mode is less commonly seen, though often mistaken for the Volmer-Weber mode, as monolayer(s) are difficult to distinguish from the support by many imaging methods. This intermediate

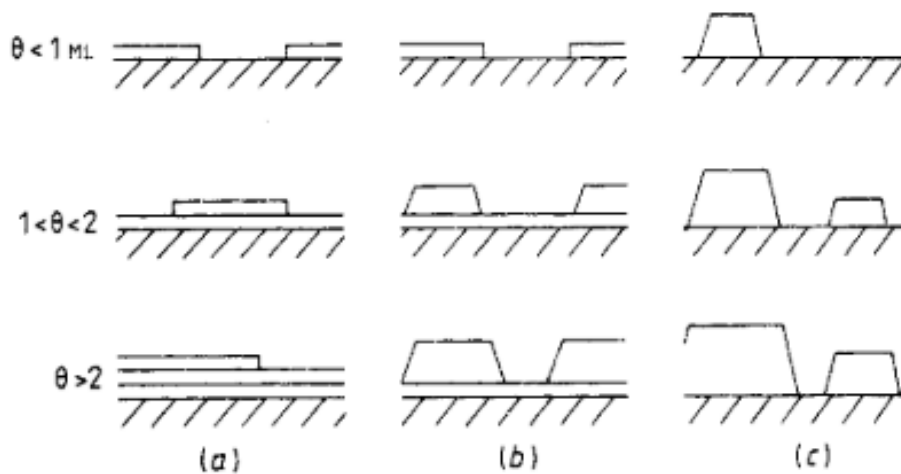


Figure 2.12: An illustration of the possible growth modes of thin films showing number of monolayers, Θ . (a) shows the layer by layer growth mode, the ‘Frank-Van Der Merwe’ growth mode, (b) Shows the layer plus island or Stranski-Krastanov growth mode, and (c) represents the island or Volmer-Weber growth mode. Reproduced from [86]

is formed wherever the formation of islands or clusters is unfavourable and is mediated through layers, such as a large lattice mismatch or molecular orientation.

Any catalytically active material demonstrating a Stranski-Krastanov or Volmer-Weber growth mode will appear to have similar surface structures (if not electronic response in the case of S-K) as a cluster beam source produced catalyst. As Volmer-Weber growth modes are seen in most metal/metal oxide systems, we can use these to mimic the cluster beam source catalysts.

2.3.3 Thin Film Catalysis

Simple sputter coating is often used for thin film catalysis[87, 88, 89]. Thin films offer benefits of cost and electronic confinement effects resulting in new and potentially useful behaviours [90]. Thin films are often cited as one to two monolayers, hence their inclusion here. The catalysts produced in this work are of the order of a few monolayers, as is much of the literature on thin film catalysis. Without corroborating surface imaging, it can be hard to tell, but we may be observing very similar effects across the two disciplines. Thin films are usually distinguished from nanoparticle arrays, but there is often cross over, particularly in the case of Stranski-Krastanov film growth.

2.3.4 Powder Fluidisation

Powder fluidisation is a method primarily used for achieving full surface utilisation for a powder bed catalyst. A fluidised bed reactor is usually the first choice for scaling up a reaction from the lab scale [91]. Fluidisation is achieved by passing gas evenly through the particulate bed causing particulate agitation. Similar agitation can be achieved with vibration, indeed in vacuum this is the only option. An unbalanced motor is a commonly used technique to shake a container for deposition. However, it was found by Baech et al.[92] that a vibrating bed set up causes larger particles to receive a greater share of the deposited material. This makes sense due to granular convection, or ‘the Brazil nut effect’. To circumvent this effect, a monolayer or few-layer powder is necessary, and likely a finer degree of control. To achieve this higher degree of powder control, piezo agitation can be used[93, 94]. These

systems are used consistently where powder transport is required, from 3D printing systems [95] or used as a directional transport system for powder through a tube [96]. Naturally for such a process, powder rheology is of key importance, and this varies greatly between materials. For the purposes of this work, we will concentrate on a powder's cohesiveness or flowability, as this is what will determine how well it fluidises. Powder flowability can be measured in several ways, the simplest being the angle of repose: the angle that the edges of a pile of powder make to the horizontal. This is akin to the wetting angle of a droplet on a surface, and is simply measured as $\arctan(h/r)$ where h is the maximum height possible to stack the powder on a circular platform of radius r [97]. A lower angle indicating a powder with a higher flowability. A powder can be said to be fully fluidised when this angle drops to zero. While there are many ways to characterise a powder's flow characteristics, this suffices for the purposes of this project.

2.3.5 High Current Ion Sources for Thin Film Deposition

Much of this section is based on Kaufmann and Robinson [98] and this is recommended for further reading. Kaufmann ion sources ('ion gun' used interchangeably), offer high current capabilities but require an exposed anode, which will need to be replaced periodically. The exposed anode can be removed in favour of a radio-frequency coupled plasma generation chamber, and as such, these RF ion guns are used primarily for reliable sputtering with reactive working gases, O_2 , Cl_2 and so on that would 'burn out' an exposed

anode. Broad beam ion sources were initially researched as a mass-efficient form of space propulsion[†] in the 1950s but are currently more likely to be found in surface science applications of thin film creation and sputtering, for a wide variety of projects. Broad beam ion sources fall into the gridded and non-gridded types. For a gridless source, ions are focused into a beam by the flow of emitted thermionic or secondary electrons from the cathode [99]. A gridded source uses a pair of grids, one grounded for shielding, and an acceleration grid aligned to provide an accelerating electric field[79].

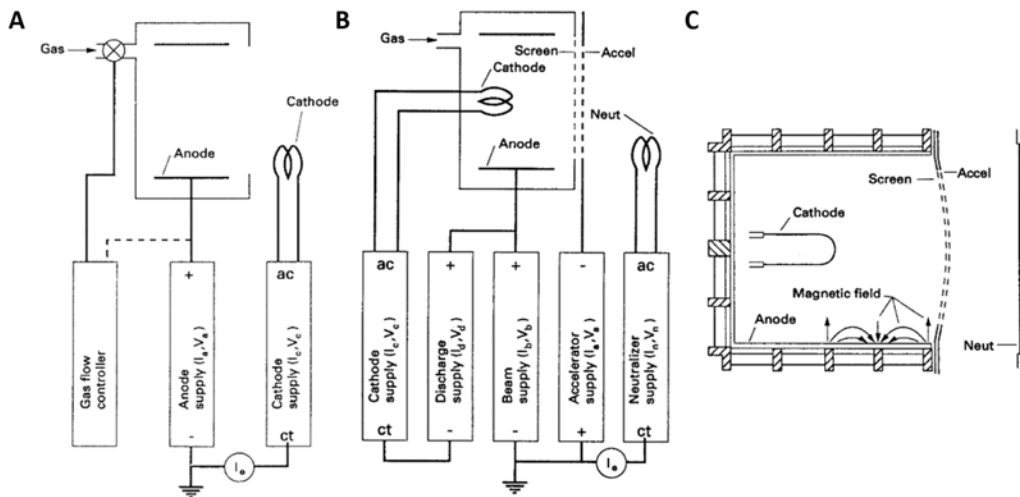


Figure 2.13: Schematic representation of A) gridless ion sources, B) gridded ion source and C) gridded broad beam ion source, More commonly known now as a Kaufman Ion Source. Reproduced from [98]. Note all diagrams are cross sections of cylindrical chambers

Low energy gridless ion sources are capable of producing high currents and low plasma potentials. Thus these sources require a high gas flow and are generally used for surface structure modification when sputtering is undesirable. Gridded ion sources offer an increased acceleration energy at the

[†]See VASIMIR for further reading on modern propulsion uses

expense of current, bringing the source into the region of sputtering efficiency. Due to the concentration of ions in between the grids in a gridded source, there is a limit to the current of the source given by Child's law[100]:

$$I_{max} = \frac{1}{9\pi} \sqrt{\frac{e}{m}} \frac{V^{\frac{3}{2}}}{l_g^2} \quad (2.6)$$

Where I_{max} is the maximum current achievable, (e/m) is the charge to mass ratio, V is the voltage of the accelerating grid and l_g is the gap between the grids. This is merely a theoretical maximum, and in practice the value is 20-50% of this due to the area for extraction is less than the beam area, due in the main to the grid itself. Also the region of acceleration is in practice larger than the gap between the grids[98].

As shown by equation 2.6 to achieve a high current ion source it is necessary to have a high beam area. Increasing the acceleration voltage, while not always desirable, has a limited range of efficiency for sputtering applications. Increasing V also requires an increase in grid separation to prevent arcing, particularly at the higher local pressures required for high current production.

Most sources in practice use magnetic fields permanent or electric to direct the flow of ions, as in figure 2.13. This increases the flux of the beam and decreasing sputtering of the anode.

In general, sputter yields fall off as a function of sputter energy, due to the relative proportion of energy absorbed into the bulk via collision cascade. If sputter yield is normalised by ion energy, the yield/eV peaks around 500eV with some material dependence. For this reason DC, gridded ion guns

are used for sputtering applications due to their high current and efficient sputtering voltage range.

2.4 Scanning Transmission Electron Microscopy

2.4.1 Equipment

Electron microscopes were initially designed in the 1930s. By using a high energy beam of electrons it is possible to probe far smaller objects than is possible with visible light due to their very short DeBroglie wavelength at high energy, such that a $200kV$ electron has a wavelength of $2.5pm$. The Scanning Transmission Electron Microscope (STEM) used for this work is an aberration corrected Jeol 2100F with a resolution of up to one angstrom.

Most STEMs use a Schottky emitter; a type of field emission electron gun (FEG) to generate electrons. This consists of a single crystal tungsten tip, coated with a zirconia film to reduce the work function. The tip is sharpened to nanometer dimensions to concentrate the electric field near the tip apex to allow for field emission to occur. Emitted electrons are accelerated to the desired energy ($200keV$ in this work) by a pair of anodes. The condenser lenses focus divergent electrons from the FEG while those that are not collimated well are removed by the aperture. The aberration correction used in this system is a CEOS GmbH double hexapole spherical aberration tuned to equal and opposite that of the condenser lenses. The beam is then focused to a point using the objective lens and passed through the sample. Subsequent electron detection is shown in figure 2.15.

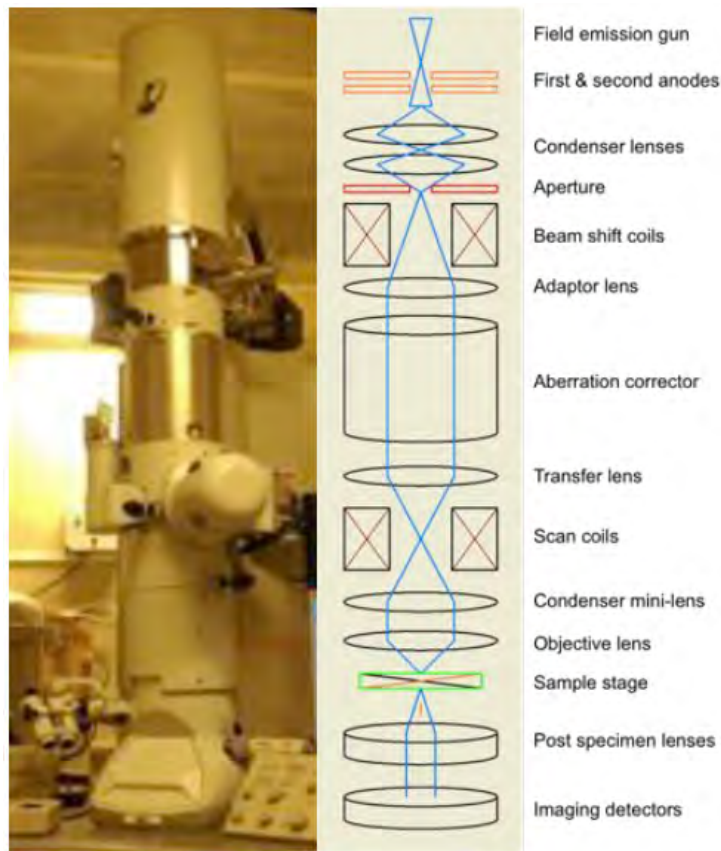


Figure 2.14: The Scanning transmission electron microscope with a CEOS GmbH aberration correction module used for this work, showing the instrument itself and a diagram of the lens system. Reproduced from [29]

A central circular detector picks up the transmitted electrons, delivering a Bright Field (BF) signal. Annular detectors of varying diameters pick up scattered electrons at increasing angles. Dark Field (DF) detectors are annular and detect scattered electrons, producing an inverted contrast DF signal. High Angle Annular Dark Field (HAADF) detectors are similar to DF detectors, simply with a larger collection angle, and thus detect high angle scattering from nuclei in the sample. Thus these pixels demonstrate a correlation of intensity with the proton number of the nucleus they scattered

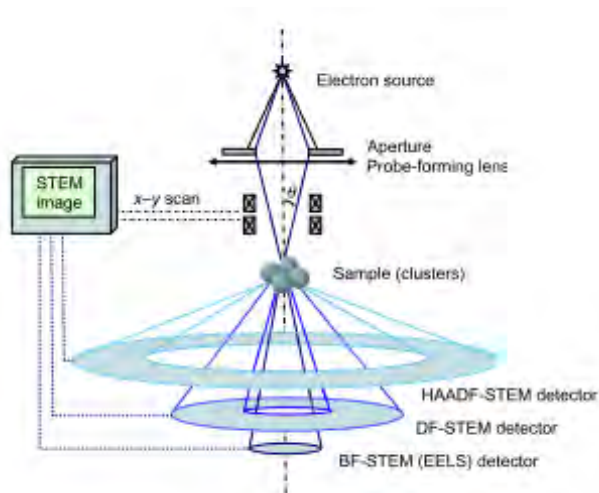


Figure 2.15: The scanning transmission electron microscope with an emphasis on available detectors, showing the locations of the bright field (BF) and Electron Energy Loss Spectroscopy (EELS) detectors, annular dark field (ADF) and High Angle Annular Dark Field detectors (HAADF). Reproduced from [101]

off (Z contrast).

A full image is built by scanning the beam over the surface, stopping for a pre-determined dwell time at locations desired for pixels in the image. The integrated current at each detector over this dwell time is recorded, giving a pixel intensity value. Pixels are built up in a (nominally) square array and a 2D array of intensity values is recorded to form an image.

2.4.2 Image Analysis

In terms of catalyst characterisation, STEM is generally used for size distribution analysis, as is the case throughout this work. There are also many important qualitative assessments of the catalysts that can be made, generally based on the surface structure of the metal: agglomerates, over-deposited ar-

eas, uneven depositions and so on. This section covers the analysis of STEM images to acquire a cluster size distribution. This is done in two ways over the course of the project: thresholding and edge detection methods, both using imageJ to analyse batches of dm3 images (produced by Gatan Digital Micrograph software).

Using thresholding requires a flat background, as the threshold is based on absolute pixel values, and on uneven backgrounds such as support particles this needs to be removed. This is done using a Gaussian blur (a convolution of the image with a Gaussian function in X and Y) of $\sigma \approx 4nm$ to generate a background image. This blurred image is then subtracted from the original image leaving a flattened background with the clusters highlighted. The contrast is rescaled and the image thresholded. Any pixel below the thresholded value is set to white, any above is set to black, by analysing the areas of grouped black pixels, and assuming spherical geometry the size of clusters is determined and plotted in a histogram. This process is illustrated by figure 2.16.

This method can be automated in the main, but thresholding proves unreliable and requires manual input to determine threshold values, introducing a source of human error. As such other methods were investigated. The method used for much of the work was an edge detection algorithm based on a Canny edge detector. As before the background of the image is removed. A Canny edge detector is run, highlighting the edges of clusters. The Canny edge detection algorithm offers more consistent sizing of clusters, but requires fine tuning for noise levels and requires a secondary filtering stage to remove noise. This is because short lines along step edges are picked

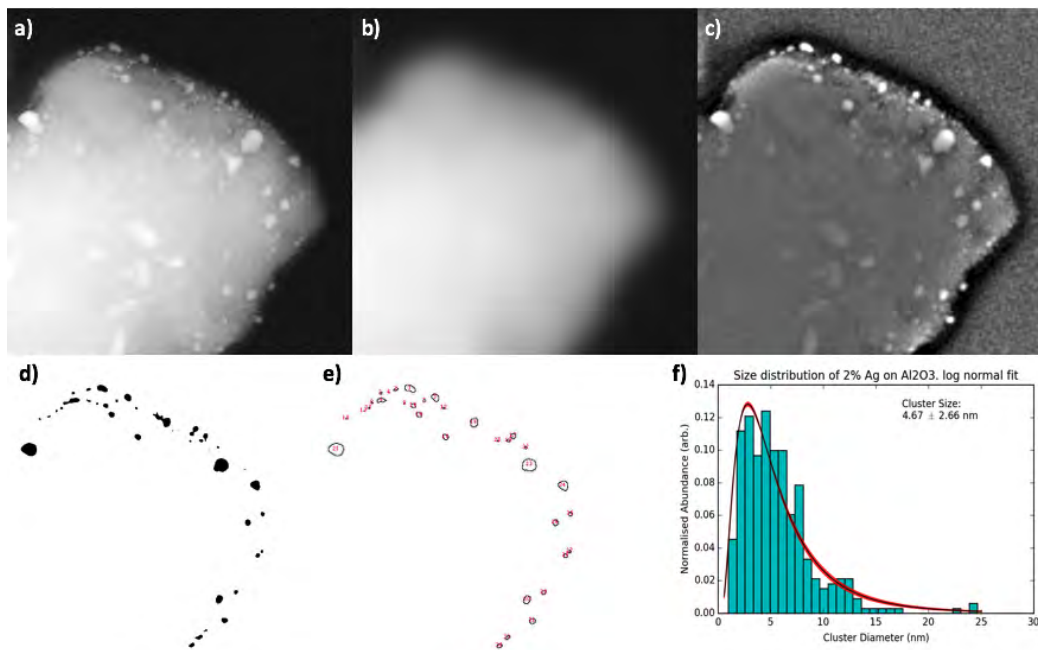


Figure 2.16: The thresholding method used to analyse a MACS Ag/Al₂O₃ STEM image, showing a) the original image, b) the background after a Gaussian blur of radius = 6nm, c) the result of subtracting (b) from (a), d) the thresholded image, isolating clusters, e) the clusters analysed and labelled and f) the size distribution obtained from a number of images.

up as clusters. As such this filtering consists of removing particles if they are both high aspect ratio and small with a linear cutoff allowing larger volume particles to have higher aspect ratios while low volume high aspect ratio ‘particles’ are filtered out. The filter cutoff will depend upon support used, image quality, and particle size/shape.

Both methods have been used through the project, giving consistent results, with the Canny macro favoured as it relies less on the judgement of the operator, and offers itself more smoothly to automation. Tuning parameters for the algorithm are: Canny parameters; Initial Gaussian blur radius, Canny thresholds high and low, and finally cut off point and gradient for the noise

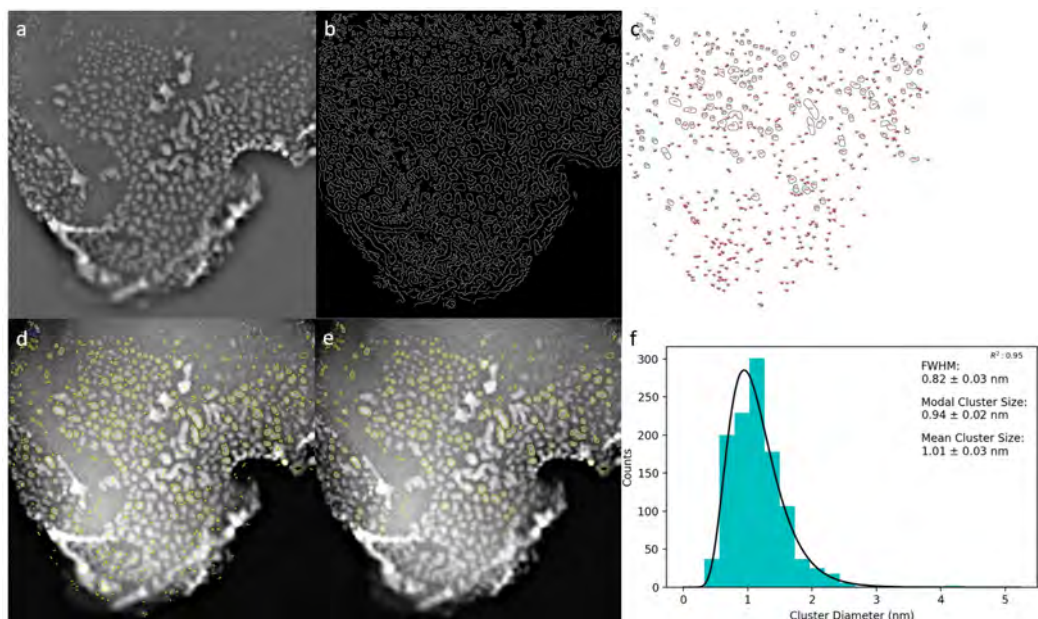


Figure 2.17: The Canny Edge detection method used to analyse a CCS Pd/Al₂O₃ sample, showing a) the background reduced image b) Image after Canny edge detection c) Particles detected from the Canny mask d) Particles overlay on original image e) Particles analysed post noise reduction f) The size distribution obtained from a number of images.

filtration. These factors are tuned for individual image sets to maximise the number of clusters accurately measured. This process is illustrated by figure 2.17.

2.5 Chemical Analysis

This project seeks to bridge the realms of chemical and physical testing methods. Chemical methods tend to give a macroscopic picture of the entire sample, while physical analysis tends to focus on the microscopic. As such, the microscopic case is often assumed to apply to the whole sample, but this is not necessarily the case. This will be discussed further in chapter 5. This

section will cover the theory of operation of the standard chemical analysis techniques used and their applications.

2.5.1 Inductively Coupled Plasma Mass Spectroscopy

Inductively Coupled Plasma Mass Spectroscopy (ICP-MS) is used to determine elemental composition and quantity within a sample. This is done by ‘digesting’ the sample in an acid, usually Nitric acid HNO_3 , but Hydrofluoric acid (HF) and Hydrogen Peroxide (H_2O_2) for silica and organic samples as required. Aqua Regia ($(HNO_3+)_3HCl$) is used for gold containing samples. In almost all cases samples are heated moderately ($< 100^\circ C$) and left to ‘digest’ for an hour or two. Digested samples are then injected into a chamber containing inductively coupled argon plasma. ICP is best suited for this process due to the lack of filaments or metallic hardware within the plasma, which is likely to sputter, interfering with the results. The sample is charged by the plasma and accelerated by differential pumping through a mass filter. Quadrupole mass filters are used here for their continuous throughput (in comparison to the cluster beam systems shown in figure 2.1) and sensitivity to low masses. The quadrupole mass filter is scanned over the expected mass range and peaks are observed at specific atomic masses by way of an ion current incident on the detector. The total integral of the support peak is compared to the total integral of the metal peak, and as such a metal percentage is determined[102].

There are multiple ways of ‘digesting’ a sample. The method covered here is dissolution and nebulising (spray injection). However, laser abla-

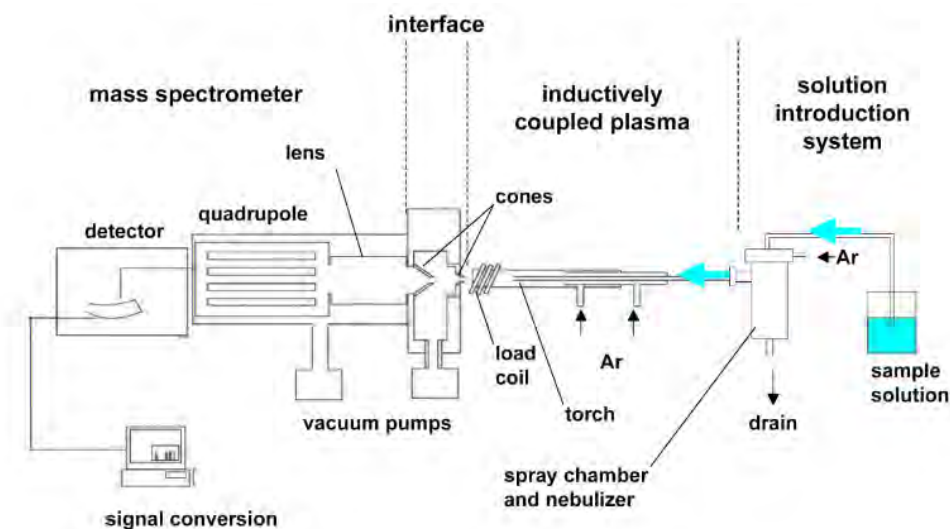


Figure 2.18: A schematic representation of an ICP-MS unit showing the digested sample undergoing argon pressurised nebulisation. The load coil generates an argon plasma within the tube, ionising the solution from the torch. The cones collimate the beam and extract it through differential pumping into the quadrupole mass filter. Zero Y/Z momentum is required for accurate measurement. The quadrupole separates particles by mass like an optical prism. The detector picks up those of a certain small mass range and amplifies this signal before it is analysed by a computer. Reproduced from [103]

tion can be used for solid samples, simple injection for gases, and thermal vaporisation for slurries[102]. ICP techniques can be used to detect incredibly small quantities of material, as low as one part per trillion (10^{12})[104], though applications for this resolution are limited. Due to the nature of the instrument higher accuracy can be achieved by scanning more slowly over the mass range, or scanning a narrower range if the operator knows what elements they are expecting. These limitations can of course be overcome by simply analysing more material. In many cases throughout this project, particularly in chapter 3, the time consuming nature of sample production

limits the quantity of material available for ICP-MS, and this is what limits the resolution of the data.

2.5.2 Temperature Programmed Desorption

Temperature Programmed Desorption (TPD) or Temperature Desorption Spectroscopy (TDS) is a technique for analysing the retention of adsorbed species to a surface. The surface is cleaned, usually with a reduction cycle: heating under a hydrogen containing atmosphere to remove surface species. The surface is then exposed to a flow of adsorbate, such as hydrogen, nitric oxide or carbon monoxide in order to completely cover the surface. The choice of adsorbate will depend on the reaction and material in question. Finally the sample is heated under the flow of an inert carrier gas such as argon. As the adsorbate desorbs it is measured downstream by a thermal conductivity detector or similar. This gives information about the quantity of adsorbate on the catalyst as well as an indication of its bonding characteristics. TPD can be performed in UHV conditions by heating the sample and monitoring the pressure of the chamber, or by use of a spectroscopic gas analyser[105]. Example data is shown in figure 2.19.

Figure 2.19 shows the desorption of hydrogen from a copper catalyst at $\sim 290\text{K}$ as a single peak comprised primarily of Cu(111) facets, broadened by the presence of (100) and (110) facets. Individual peaks can be identified as arising from different facets or materials owing to their differing interaction energies.

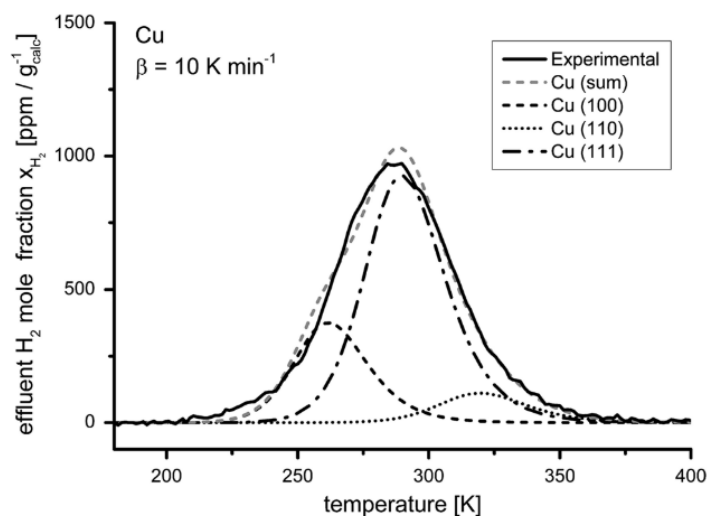


Figure 2.19: Example hydrogen temperature programmed desorption showing the experimentally observed peak as a compound of simulated facets at different percentages. Reproduced from [106]

2.5.3 Chemisorption Testing

Chemisorption techniques aim to measure the quantity of an adsorbate that can be strongly adsorbed or chemisorbed to the surface of a catalyst. This can be used to measure the active surface area of a catalyst excluding the support areas, particularly where the adsorbate used is a reactant of interest. Again, the sample surface is cleared with a reduction cycle, heating under a hydrogen containing atmosphere. The quantity of adsorbate can be measured by venting a known quantity into the chamber a number of times, and measuring either the pressure increase, or thermal conductivity change the pulse imparts on the system. Pulses that are adsorbed are not measured. Once pulses are measured the sample is assumed to be saturated and the unmeasured volume has been chemisorbed. Volumetric chemisorption carefully measures the leak rate or small pulse volume to determine the volume

of gas required to increase the pressure of the system. The system volume is also measured carefully by a similar process using noble gas. Using the ideal gas law $P = \frac{nRT}{V}$ the expected pressure increase is compared with the measured increase and used to determine the volume of adsorbate adsorbed. This process is repeated after exposure to vacuum which removes weakly bonded species. The second run does not measure the chemisorption sites as they remain occupied. By subtracting the volumes measured across each run, the chemisorbed volume is determined[107]. A summary of the chemisorption process and analysis is shown in figure 2.20

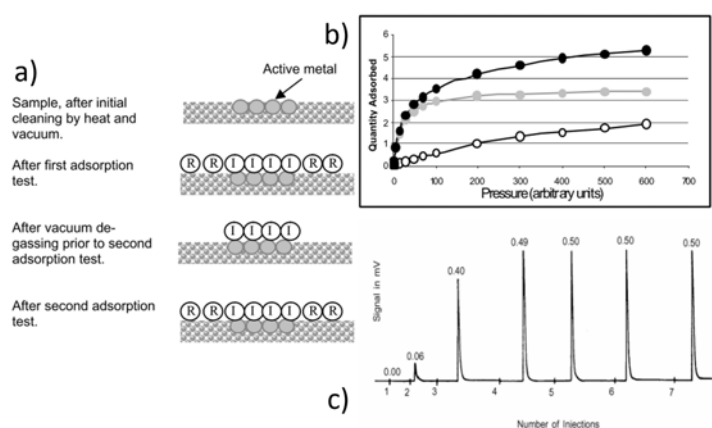


Figure 2.20: The chemisorption process and measurement techniques showing a) A schematic of the process of chemisorption showing reversibly (physisorbed) (R) and irreversibly (chemisorbed) (I) adsorbed species. b) shows example data from volumetric chemisorption with initial (black dots), repeat (grey dots) and difference (white dots) isotherms. c) shows example pulse chemisorption data showing chemisorption of 2.05 pulses. Reproduced from [107]

Chapter 3

Formation of catalysts using the Matrix Assembly Cluster Source

3.1 Introduction

In this chapter we cover the setup and working theory of the MACS and the procedure for catalyst creation. Created catalysts are characterised by Aberration Corrected Scanning Tunnelling Electron Microscopy (AC-STEM) to analyse their morphology and Inductively Coupled Plasma Mass Spectroscopy (ICP-MS) to determine the metal loading. The catalytic properties of MACS samples are compared to those of more standard samples created using Incipient Wetness impregnation (IWI). It has been shown previously in related work that magnetron cluster beam samples can demonstrate significant improvements in selectivity at high conversions over chemically syn-

thesised catalysts for selective hydrogenation[8], and this is investigated for MACS samples.

3.2 Experimental Setup

3.2.1 MACS Instrument

The MACS unit used for this work is a custom unit comprised of commercially available products making up the primary components. It consists of a cold finger on which the matrix is formed, a thermal evaporator to dose the matrix with metal, an ion source to sputter the formed matrix, and a deposition cup to collect the clusters on agitated powders. The MACS is run in reflection mode. The cold finger is a Sumitomo cryogenics HC-4E compressed helium chiller with a base temperature of $17.2K$ in the MACS configuration. The evaporator used is a Createc high temperature effusion cell, capable of $2000^{\circ}C$. This is a crucible based evaporator using pyrolytic boron nitride (PBN) or alumina crucibles for metals requiring evaporation temperatures $< 1700^{\circ}C$ and Pyrolytic Graphite crucibles for higher temperatures. Standard refractory metal crucibles (Tungsten, Molybdenum and so on) alloy well with PGMs, and as such cannot be used. The ion source is a radio-frequency, inductively coupled TecTra ion etch sputter gun, capable of 4mA beam current. This feeds into a set of 4 ion optics, biased with $\pm 3 kV$ Glassman high voltage power supplies. The deposition stage is a modified custom unit from Teer Coatings ltd, consisting of a cup and unbalanced motor to agitate the powder within. The matrix support is a custom build piece

designed and built at the University of Birmingham from oxygen free copper to maximise thermal conductivity.

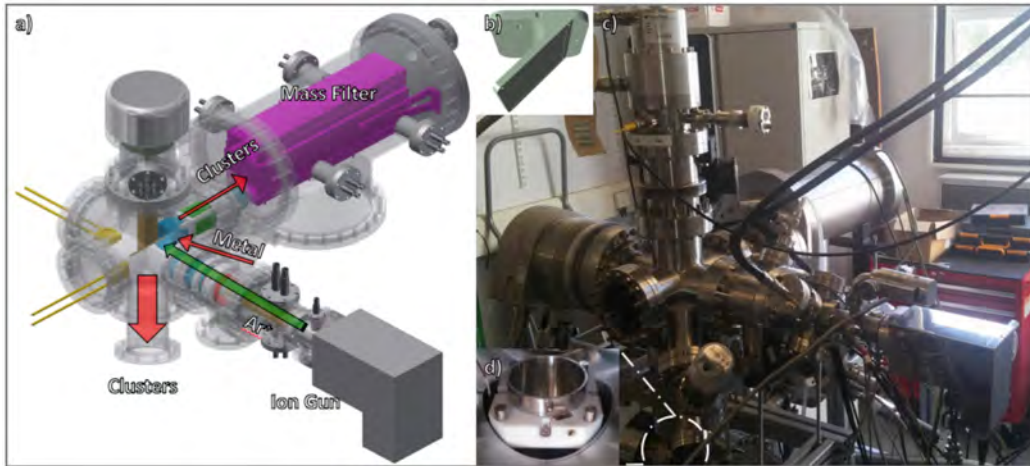


Figure 3.1: The MACS unit used for this project showing a) the system geometry [29] b) the schematic for the matrix support, c) the MACS instrument in the laboratory and d) the vibrating cup in the deposition chamber

The deposition cup is mounted on a magnetically coupled drive that moves the cup vertically towards the matrix support, reducing the throw distance from the centre of the support to the cup rim of 5cm during deposition. The cup can be retracted into the deposition chamber, which can be isolated and vented separately for sample loading and removal.

For this project, the MACS unit was modified by the author and Lu Cao to create the downwards deposition geometry using the matrix support shown in figure (3.1 b). The deposition chamber was added for ease of use and to enable multiple samples to be deposited without venting the main chamber or warming the cold finger. The deposition cup and magnetic drive were added to enable deposition onto powder with no increase in throw distance.

3.2.2 MACS Parameters

A few important variables dictate the deposition of clusters from the MACS unit. During dosing, the temperature of the evaporator is controlled as well as the chamber pressure. These factors control the rates of metal and gas deposition onto the matrix support, and thus control the matrix concentration. The matrix loading can be calculated using 2.3. It is necessary to calibrate the deposition rate of metal as a function of temperature as this will depend on deposition geometry, aperture size, choice of metal and the location at which the temperature is measured. Deposition rate is measured using a quartz crystal microbalance (QCM), placed in the same location as the matrix. QCMs monitor the decrease in resonant frequency of a piezo crystal as mass is deposited onto it and relate that to the mass added.

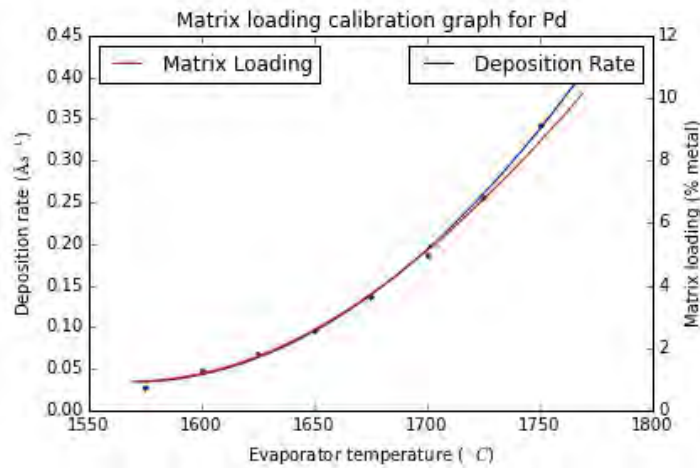


Figure 3.2: A calibration curve showing the rate of evaporated metal, and how it compares to matrix loading in a matrix formed of Pd and room temperature Ar at a pressure of 1.0×10^{-5} mBar. This can be used to calculate the matrix concentration

Calibration curves such as this are produced for each metal in each

configuration used, and were used to calculate the matrix loadings for all depositions.

3.3 MACS Flux

A key consideration for any catalyst is the metal loading. To measure this, the flux of the MACS unit must be measured. The MACS system was run at higher dosing pressures and temperatures, and sputtered with higher current, producing thicker matrices and sputtering them more rapidly.

3.3.1 Beam Shape

In order to measure the flux of the MACS unit, the beam shape must be measured to determine the total volume of material passing onto the support. This was measured using an offset set of TEM grids mounted from the beam centre to measure the fall off of the beam flux. Five TEM grids were placed at one centimetre intervals from the central point of the chamber to the edge. Due to spacial restrictions this was the only available location for beamshape testing and as such this is merely an informed estimate. Flux was calculated by cluster size and density.

Assuming a two dimensional Gaussian beamshape, a scaling factor for the total flux is produced: 0.887. Multiplying the central flux value by the scaling factor results in the average flux within the chamber limits. This is used to calculate the total flux of the system.

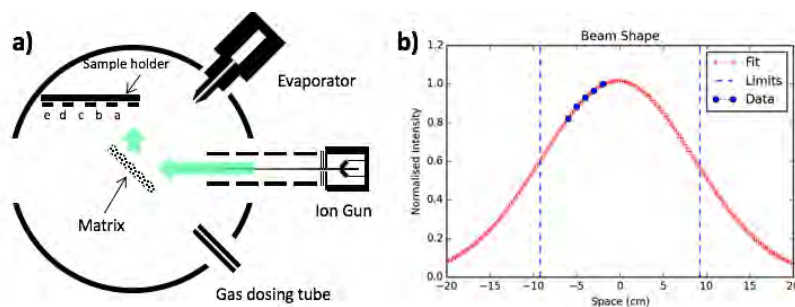


Figure 3.3: Figure demonstrating how the beamshape was measured showing a) The experimental set-up within the MACS chamber, and b) The resultant beam shape. Limits indicate the positions of the chamber walls

3.3.2 Flux Measurement

Flux was measured using a QCM, placed in the beam at the central point. The matrix was 3% silver in argon, dosed for one hour. Dosing conditions: evaporator temperature: $1250^{\circ}C$, Ar dosing pressure: $8.0 \times 10^{-6} mBar$. The matrix was biased at $-200V$ in order to improve the focus of the ion beam. Ion beam current was measured using the biasing power supply, ion beam current was $2.6mA$.

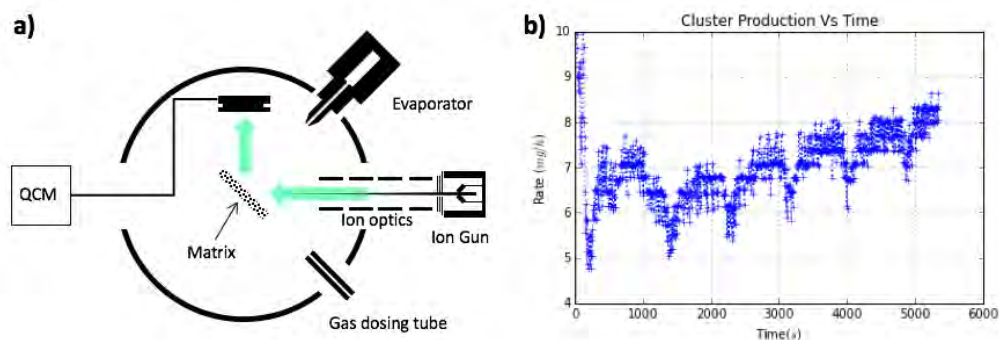


Figure 3.4: Figure demonstrating how the flux of the cluster beam was measured showing a) The experimental set-up within the MACS chamber and QCM b) The flux measured on the QCM scaled to the beam size. Periodic effects were found to be background.

The flux measured in this experiment equates to a cluster beam current of $10.2\mu A$ assuming singly charged clusters of 100 atoms.

3.4 Sample Production and STEM Analysis

Catalysts prepared using the MACS system in the configuration shown in figure 3.1 were prepared on Silica (SiO_2) and Alumina (Al_2O_3). Loading is calculated by analysing the flux of deposited clusters before and after deposition onto powder and averaging the values to get a beam dose into the cup. Assuming a sticking coefficient of 1 a wt% loading is calculated. Samples were produced at an estimated loading of $0.5\text{wt}\%$ and as such IWI samples were made to this loading.

3.4.1 Gold on Alumina

Gold alumina samples were produced using the MACS unit and IWI. MACS samples were deposited for five hours in five separate one hour depositions with a dosing pressure of $1.0 \times 10^{-5} mBar$, evaporator temperature of $1550^\circ C$ creating a 4.2% metal matrix over 45 minutes for each deposition. Impregnated samples were prepared using 1.27mMol chloroauric acid diluted with water to make a smooth slurry of fifty grams of alumina powder. The samples were dried at $80^\circ C$ overnight and reduced at $250^\circ C$ under an atmosphere of 1% H_2 in N_2 for four hours.

As shown by figure 3.5 it can be seen that the size distributions are broadly similar, with the IWI sample demonstrating a larger average cluster size and spread. Note the differing scales. The IWI sample's distribution has

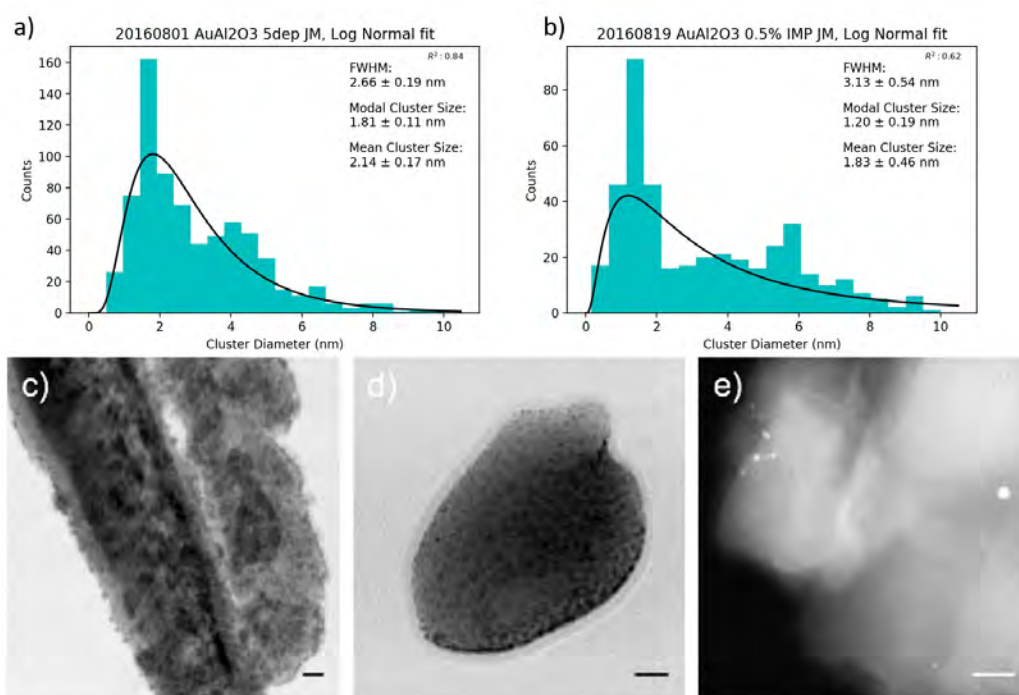


Figure 3.5: Characterisation of Au clusters on Al_2O_3 showing a) The size distribution of gold clusters produced by the MACS system (cluster beam), b) The size distribution of gold clusters produced by IWI, c) and d) show example BF-STEM images of $\text{Au}/\text{Al}_2\text{O}_3$ produced using the MACS, and e) shows an example HAADF-STEM image of $\text{Au}/\text{Al}_2\text{O}_3$ produced by IWI. Scale bars are 20nm

a relatively flat profile while the cluster beam sample demonstrates a fairly classic bimodal pattern, indicating agglomeration of similar sized clusters from the beam. More metal is observed in the MACS samples, whereas some large crystalline structures are observed in the IWI sample, and it is these that are thought to account for the difference in observed metal quantity. Some areas in the MACS sample appear to be over-deposited 3.5 c).

3.4.2 Gold on Silica

Gold clusters on silica were prepared in the same way as before on silica using identical parameters and method for both MACS and IWI methods.

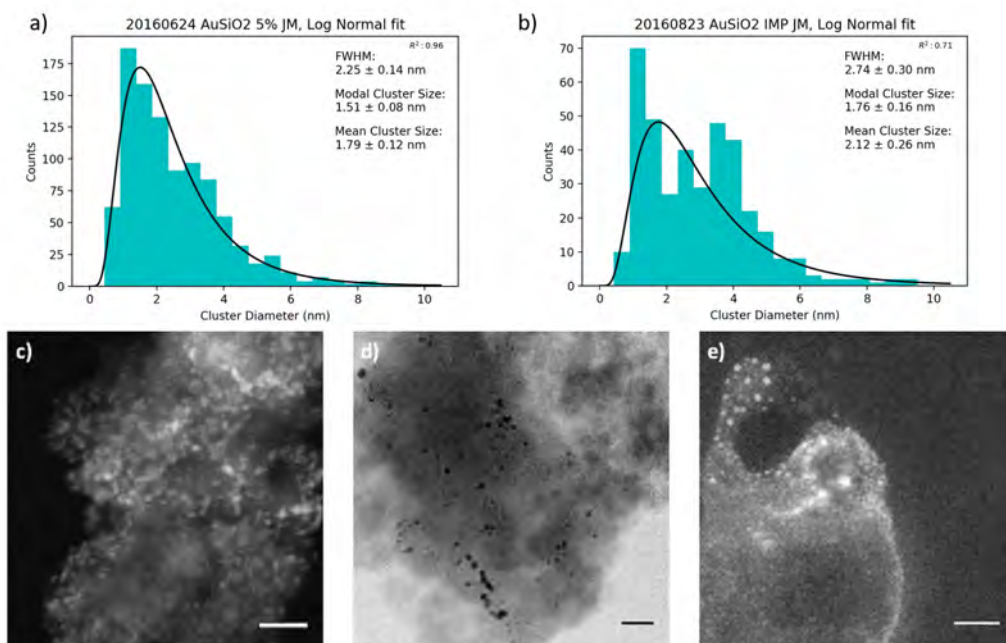


Figure 3.6: Characterisation of Au clusters on SiO_2 showing a) The size distribution of gold clusters produced by the MACS system, b) The size distribution of gold clusters produced by IWI, c) shows an example HAADF-STEM image of Au/ SiO_2 produced using the MACS, d) and e) show examples of HAADF and BF-STEM images of Au/ SiO_2 produced by IWI. Scale bars are 20nm

Similarly to figure 3.5, figure 3.6 shows similarly differing size distributions. No crystalline structures were observed in either sample and little overdeposition was observed in the MACS sample, the worst example of which is shown in figure 3.6 c). This is likely due to the increased surface area of the SiO_2 support over the Al_2O_3 .

3.4.3 Palladium on Alumina

Palladium was chosen for its activity in a number of hydrogenation and oxidation reactions. The method was adapted from previous gold samples, requiring higher evaporator temperatures of $1700^{\circ}C$ evaporator temperature and a chamber pressure of $1.0 \times 10^{-5} mBar$ producing a 4.8% metal matrix. Once again, samples were produced from five one hour depositions with a forty five minute dosing time. IWI samples were produced by dilution of 2.35mMol Palladium (II) nitrate, creating a slurry with fifty grams of support. Once again samples were reduced at $250^{\circ}C$ under an atmosphere of 1% H_2 in N_2 for four hours.

Pd/Al_2O_3 samples produced by the MACS unit demonstrate lower sizes than those produced by impregnation. This is thought to be due to the low defect nature of the Al_2O_3 support, demonstrated well by figure 3.7 e). The distribution appears to be bimodal due to the ion exchange style particle growth shown in 3.7 f), which produces the peak at $2nm$.

3.4.4 Palladium on Silica

Palladium samples on silica were prepared using the same methods as the palladium on alumina samples as before.

As can be seen by figure 3.8 IWI samples demonstrate a slight increase in average size as well as distribution width as those produced by the MACS. As observed with the previous gold samples it is thought that the slight porosity of the SiO_2 as well as its increased capacity for water retention during catalyst preparation has lead to a more evenly distributed metallic

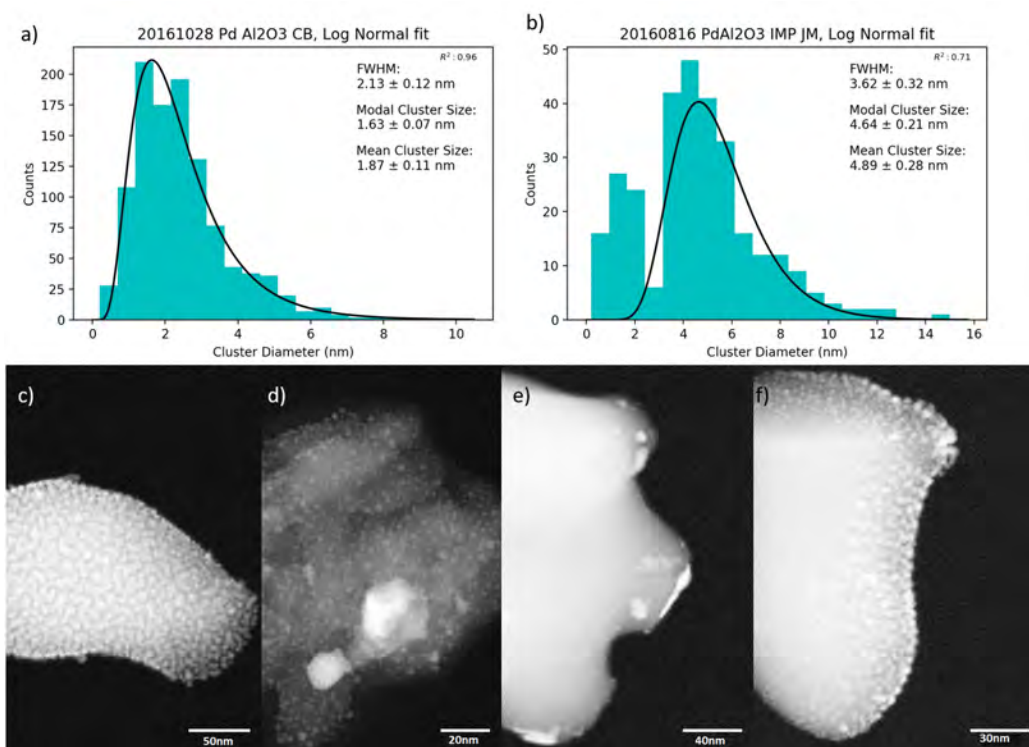


Figure 3.7: Characterisation of Pd clusters on Al_2O_3 showing a) The size distribution of palladium clusters produced by the MACS system, b) The size distribution of palladium clusters produced by IWI, c) and d) show example BF-STEM image of Pd/ Al_2O_3 produced using the MACS. e) and f) show example BF-STEM images of Pd/ Al_2O_3 produced by IWI. *Note the scale bars of c) and e)*

phase over the Al_2O_3 support.

3.4.5 Sample Summary

In general, samples produced by the MACS unit demonstrate an average cluster size of $\sim 1.6\text{nm}$ regardless of the support used, with somewhat more agglomeration observed on the lower defect Al_2O_3 support. Impregnated samples show less consistent sample distributions and less apparent material across all samples (note the number of clusters measured for each size distri-

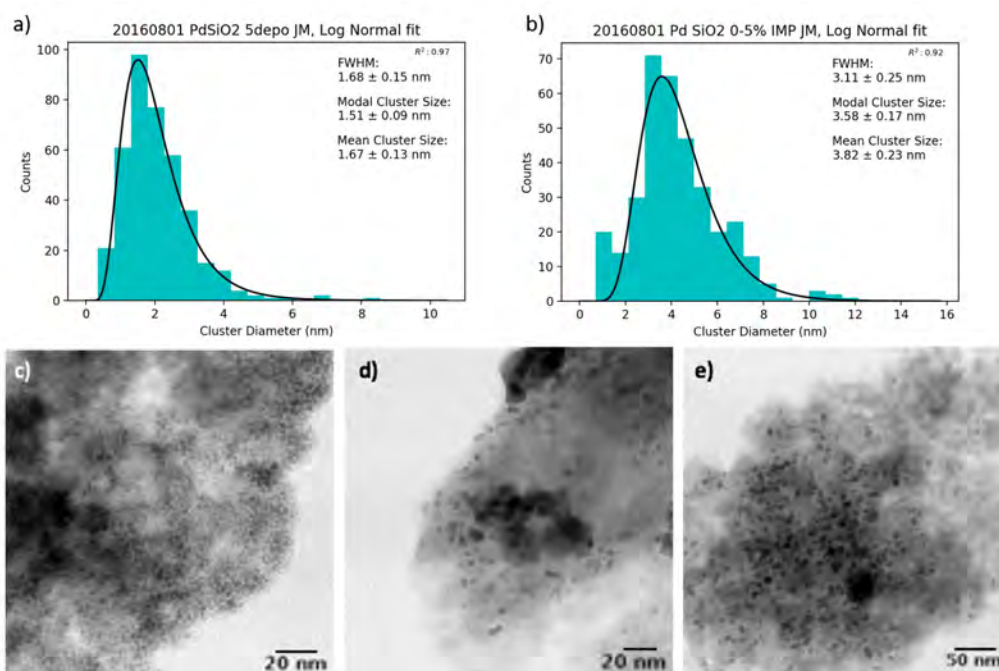


Figure 3.8: Characterisation of Pd clusters on SiO₂ showing a) The size distribution of palladium clusters produced by the MACS system, b) The size distribution of palladium clusters produced by IWI, c) shows an example BF-STEM image of Pd/SiO₂ produced using the MACS, d) and e) show examples of BF-STEM images of Pd/SiO₂ produced by IWI. *Note the scale bar of e)*

bution). Gold samples show slightly wider size distributions than palladium due to its inert nature and hence is likely to have a longer diffusion length. This results in some bimodality in the case of gold based MACS samples.

3.5 Loading

To gain an accurate appraisal of the catalytic activity of any sample, it is necessary to know the quantity of metal on its surface. This is a key consideration if one wishes to calculate the turn over frequency, or when considering the cost of catalyst production. In this case it is also a key consideration to

Sample	Loading(%)	Mean Diameter(nm)	FWHM(nm)
MACS Au/Al_2O_3	0.015 ± 0.005	2.14 ± 0.17	2.66 ± 0.19
IWI Au/Al_2O_3	0.900 ± 0.005	1.83 ± 0.46	3.13 ± 0.54
MACS Pd/Al_2O_3	0.050 ± 0.005	1.87 ± 0.11	2.13 ± 0.12
IWI Pd/Al_2O_3	0.715 ± 0.005	4.89 ± 0.28	3.62 ± 0.28
MACS Au/SiO_2	0.030 ± 0.005	1.79 ± 0.12	2.25 ± 0.14
IWI Au/SiO_2	0.0945 ± 0.005	2.12 ± 0.26	2.74 ± 0.30
MACS Pd/SiO_2	0.030 ± 0.005	1.67 ± 0.13	1.67 ± 0.13
IWI Pd/SiO_2	0.700 ± 0.005	3.82 ± 0.23	3.11 ± 0.25

Table 3.1: Sample characterisation summary showing loading as measured by ICP-MS, mean diameter and size distribution offset FWHM as measured by a log-Normal fit of the STEM cluster size analysis. Errors are calculated by fit accuracy and number of clusters analysed

measure the effectiveness of the MACS method. The most common method for this determination is ICP-MS. Samples were dissolved using nitric acid, nitric hydrofluoric acid and aqua regia for Pd/Al_2O_3 , Pd/SiO_2 and Au containing samples respectively.

MACS samples were produced at lower loadings but these fell outside the resolution of the mass spectroscopy and as such were abandoned.

As can be seen from table 3.1, MACS samples demonstrate less than 10% expected loading. This was attributed to the deposition stage. Factors to be investigated being the sticking coefficient and whether the agitation was having a negative effect on the deposition. Assuming all particles attach to the support appears reasonable from experience in cluster deposition, but there is a chance that the partially charged nature of the cluster beam depositing onto isolated oxide support particles deflects further deposition. Due to exceptionally low cluster mass, detachment due to vibration can be dis-

counted, but clusters that come into contact with the metal cup may be removed. The effective sticking coefficient is thus challenging to determine, and as such the effect of agitation was investigated.

3.5.1 Impregnated Material

Impregnated samples demonstrate a significantly increased loading over their ‘equivalent’ MACS samples, and yet demonstrate a significantly reduced quantity of clusters; see figures (3.5-3.8). As a result of this, EDX analysis was performed in an attempt to determine the location of this missing metal. Au/SiO₂ was analysed due to its suitability for imaging.

As can be seen in figure 3.9, despite no clusters being seen on the surface of the particle, there is a continuous distribution of Au across the surface that has not clustered. This is attributed to ion exchanged surface hydroxide [108, 109] also present on Al₂O₃ [110, 111, 112] forming *Si – O – Au* surface structures that appear to remain un-reduced, coating the surface of the support particles yet not producing significant contrast in STEM as a nanoparticle structure would.

3.5.2 Agitation Effects

When the powder agitation was observed, it was seen that the powder quickly moved to the edges of the cup, likely due to flexing within the base of the cup causing a central vibrational antinode. As such it is energetically favourable for powder to move to the edges of the cup where flux was lower. Agitation was set to be intermittent in future experiments to circumvent this issue.

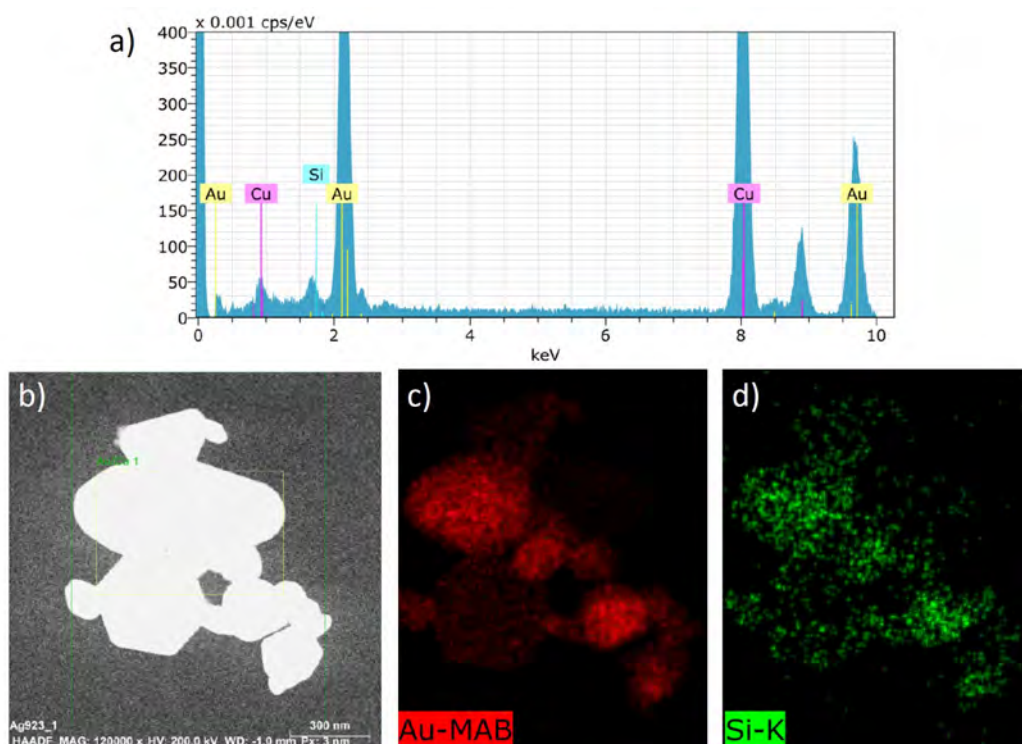


Figure 3.9: EDX characterisation of an apparently blank area of the IWI Au/SiO₂ sample showing a) the average spectroscopic result of the EDX mapping, b) the bright field image of the SiO₂ particles, c) The Au $M\alpha\beta$ peak EDX map and d) The Si K peak edx map

Large (10x) differences were observed in metal loading between agitated and still depositions and across separate samples. However, the samples produced by the MACS initially demonstrate regions of fairly significant metal agglomeration and as such, these were not reproduced at higher loading.

3.6 Catalysis Results

Samples were tested for their activity in the oxidation of carbon monoxide, the reduction of 4-nitrophenol and the selective hydrogenation of 1-pentyne to 1-pentene.

3.6.1 Carbon Monoxide Oxidation

The samples characterised in section 3.4 were tested for their activity in the oxidation of carbon monoxide. It was necessary to use a very low flow rate of 10mlmin^{-1} to observe activity in the MACS samples. The reaction was carried out in a tube furnace reactor with the catalyst sample resting on a quartz wool bung in a quartz tube. Reactant gas of 1% CO , 20% O_2 in He was flowed through the catalyst bed. The gas was analysed using an infra red absorption spectrometer, calibrated at room temperature with the reactant gas. The tube furnace temperature is ramped at 5°Cmin^{-1} and the CO concentration monitored to determine conversion.

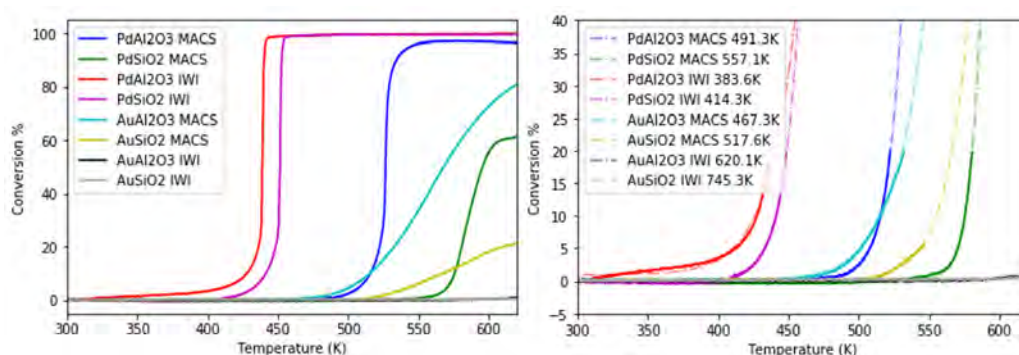


Figure 3.10: Results of the catalysed oxidation of carbon monoxide at 10mlmin^{-1} over 20mg of produced catalysts showing the overall reaction progress (left) and the fitting process used to determine the light off temperatures. Data is cut differently for MACS Au/SiO_2 as it does not demonstrate an exponential turn on at these scales.

As can be seen in figure 3.10, all samples demonstrated activity for the oxidation of carbon monoxide besides the impregnated gold samples. This is attributed to the presence of Cl^- present in the catalyst from the chloroauric acid preparation as seen by [113, 114]. Pd samples produced by

IWI demonstrate the lowest light off temperatures with alumina providing higher activity. This is attributed to the higher loading and the increased donation of oxygen from the Al_2O_3 support as shown in figure 2.8. This trend continues through all samples with alumina proving to be more active and at lower temperatures than silica as seen previously [65]. Palladium MACS samples prove more active than MACS gold, though $\text{Au}/\text{Al}_2\text{O}_3$ lights off somewhat before $\text{Pd}/\text{Al}_2\text{O}_3$. This slow catalytic behaviour is unexpected[44], though mimics the Cl^- effects observed by Bowker[113] and may be indicative of a similar contaminant affecting the rate of reaction. Both MACS gold samples demonstrate this slow turn of activity as a function of temperature however MACS produced palladium samples do not, instead showing the standard reaction progression. As there are no sources of residual reactive gases expected in the high vacuum environment of the MACS unit, this effect was attributed to contamination of copper from the matrix support as the resultant decrease in the adsorption energy will negatively affect gold more significantly than palladium. This issue is discussed further at the end of this chapter. All MACS samples demonstrate significantly higher light off temperatures than would be expected from the literature. This is attributed partly to their low loading, and partly to the lack of ion exchange present in the deposition of MACS samples[8]. This hypothesis is supported by the work done by Ivanova[115] who concluded that a high PdO/Pd^0 ratio was required for the activity of the catalyst. if we consider the initial reaction to be a reverse spillover of CO from the support to the cluster[116, 117], a PdO interface as a result of ion exchange opposed to a Pd-HO interface as a result of Pd^0 deposition would go some way to explaining the difference between

MACS and IWI samples.

3.6.2 4-Nitrophenol Reduction

The methods used for the reduction of 4-Nitrophenol was adapted from [28] as a reaction that all samples would demonstrate reactivity for. The reaction was performed at room temperature in a moderately stirred beaker. Fresh solutions of 4-Nitrophenol and sodium borohydride were prepared at 0.12 and 5.0 *mMol* respectively. 25 *cl* of each solution was mixed together and 10 *mg* of catalyst added. Samples were taken every 5 minutes with the first taken before addition of catalyst. These samples were analysed using an ultraviolet/Visible (UV/Vis) light spectrometer. The reaction is allowed to continue for 60 minutes while samples are taken. Peak absorption intensity as a function of time is used to measure the reaction rate: $k = -\frac{\delta A}{\delta t}$. This method assumes that the catalyst is well dispersed through the reaction vessel and that a proportional quantity of catalyst is removed with each sample for the UV/Vis spectrometer as ~50% of the vessel is emptied over the course of the reaction. Due to the sensitivity of this reaction to small concentrations of metal, all glassware required cleaning with aquaregia $HNO_3 + 3HCl$. Glassware was tested by leaving fresh 4 - *NP/NaBH₄* to sit for one hour before testing.

Figure 3.11 shows the results of the testing for the reduction of 4-Nitrophenol. For impregnated gold samples, the preferred support is SiO₂, for gold MACS samples, this trend is reversed indicating that this is caused by some surface manipulation during the impregnation process. For pal-

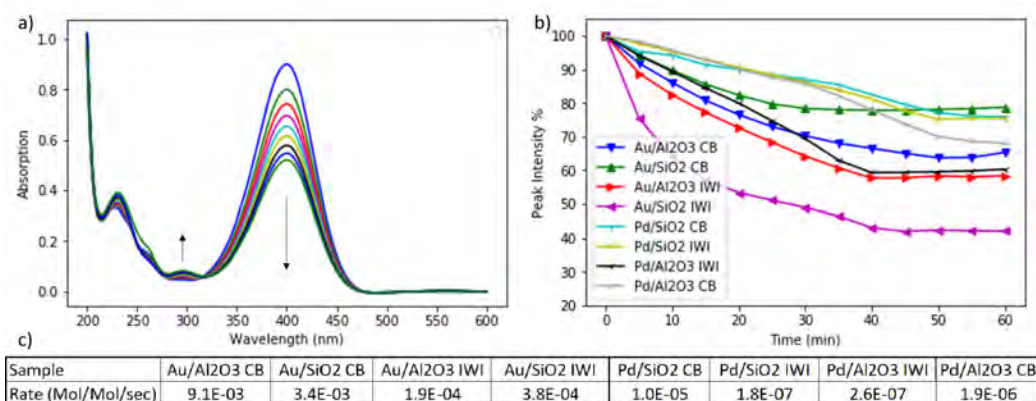


Figure 3.11: Results from the catalytic reduction of 4-Nitrophenol. a) Shows the decrease in absorption of 4-NP as a function of time catalysed by impregnated Au/SiO₂. Traces are taken every five minutes. b) Shows the reduction in peak absorption as a function of time. c) shows the initial activity of each sample in ($Mol_{Product} Mol_{ClusterMaterial} s^{-1}$)

ladium samples Al₂O₃ is the more reactive support, likely indicating that it has a favourably lower adsorption energy than SiO₂. Across all samples gold appears to be the more active metal, however appears to deactivate after ~40mins while palladium samples continue to be active for the duration. The reaction can be continued by addition of $NaBH_4$ to the vessel, indicating that the gold samples are catalysing the formation of H_2 from hydride ions, depleting the excess hydride concentration rapidly. Impregnated samples perform significantly better than MACS samples until this is normalised by their loading (see figure 3.11 c). The sensitivity of this reaction to very small quantities of metal (contaminant or otherwise) indicates that it is likely to be transport limited, and as such all reactions proceed at a similar rate despite differing loading. In this case, the results are likely to be indicative of exposed metallic surface area.

3.6.3 Selective hydrogenation of 1-Pentyne

Gold samples were found to be inactive for the hydrogenation of 1-pentyne and as such are omitted from this section.

Selective hydrogenation was performed as before in the case of carbon monoxide oxidation in a tube furnace reactor. The catalyst was placed on a quartz wool bung with reactant gas flowed through the bed. This gas was 40% H_2 in He at 250mlmin^{-1} mixed with 1M 1-Pentyne + 1M 2-MethylPentane (as an internal standard for the gas chromatograph) in an n-Hexane solvent at 0.06mlmin^{-1} . The gas chromatograph used was a CP-3800 with a CP-WAX-52CB $25\text{m} \times 0.32\text{mm} \times 1.2\mu\text{m}$ column, followed by a CP-SIL-5CB $50\text{m} \times 0.32\text{mm} \times 5.0\mu\text{m}$ column. The integrated area of each peak observed from the gas chromatograph (GC), normalised by the area of the internal standard peak was used as the total quantity of product. Integration limits for the gases were set as follows; (Min:sec); 1-Pentene: 6:42-7:05, Pentane: 7:05 - 7:23, t-2-Pentene: 7:23-7:39, c-2-Pentene: 7:39 - 7:52, 1-Pentyne: 7:52-8:10, 2-MethylPentane: 8:44 - 9:05, n-Hexane: 9:05 - 11:22.

Palladium samples were run at weights of 10, 20, 30, 40 and 50mg. Full conversion was achieved in the case of Pd/SiO₂ only at 50mg, as such this data is presented. Impregnated samples were run at a nominal 20mg weight and achieved full conversion.

The significant observed difference in figure 3.12 between MACS and IWI samples appears at room temperature. Here MACS samples are entirely inactive, while impregnated samples achieve full conversion, and mostly full hydrogenation to pentane. All samples achieve higher throughput of 1-

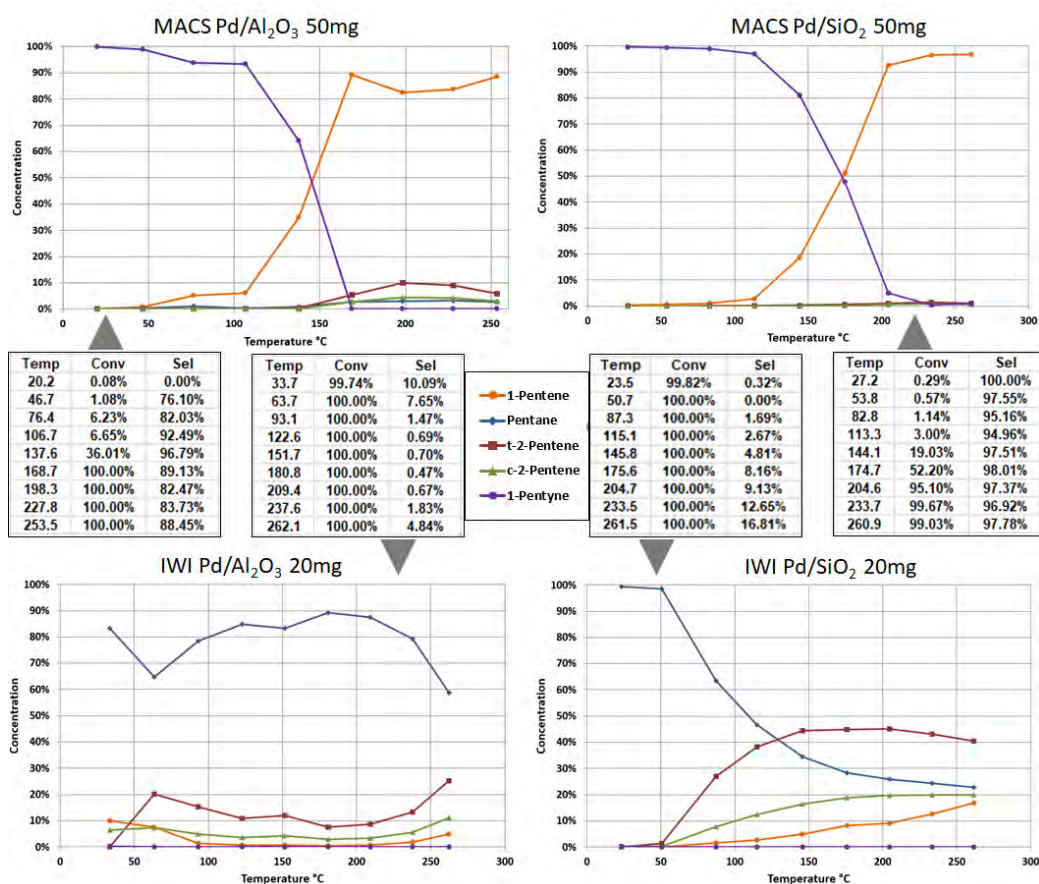


Figure 3.12: Results from the catalytic hydrogenation of 1-pentyne, showing the individual concentrations of each product as the temperature in the tube furnace reactor is ramped. Samples are listed, top left MACS Pd/Al₂O₃, top right MACS Pd/SiO₂, bottom left IWI Pd/Al₂O₃ and bottom right IWI Pd/SiO₂. Tables belong to graphs as indicated.

pentene as temperature is increased. Due to the variation in loading between MACS and IWI samples, conclusions on complete selectivity are difficult to draw. We know that the MACS samples here only just achieve full conversion, allowing little opportunity for 1-pentene to re-interact and hydrogenate further. This is best demonstrated by the MACS Pd/Al₂O₃ sample. Peak selectivity occurs at the minimum temperature at which full conversion is

achieved. As temperature increases from this point, the number of collisions with the catalyst increases as well as the average concentration of 1-pentene within the bed, allowing for an increased number of opportunities for further hydrogenation of 1-pentene. In summary, MACS samples demonstrate severely reduced activity for the low temperature hydrogenation of 1-pentene, but offer an apparent increase in selectivity at higher temperatures $> 200^\circ$. All samples demonstrate an increase in selectivity to the production of 1-pentene as a function of temperature and time.

3.7 Post Catalysis Analysis

All samples were imaged after all catalytic testing in order to determine the extent of catalyst damage. Significant sintering is not expected under thermal conditions as all experiments are conducted significantly below the Tammann temperature. Thus sintering is expected to be a product of the reaction process or reactive atmosphere. Cluster size distributions are acquired from the samples via STEM post catalysis and compared to those measured previously. The results of this analysis are summarised in table 3.2

Table 3.2 shows the results of post catalysis analysis of all samples, showing significant agglomeration only in the case of cluster beam samples under CO oxidation. It must be noted that while all samples were only raised to $350^\circ C$ catalyst temperatures are likely to be higher due to the exothermic nature of the reactions, in particular CO oxidation. This is to be expected as an oxygen containing atmosphere is far more damaging than a hydrogen containing one, and nitrophenol reduction was carried out at

	Δ Mean Size	\pm	Δ Modal Size	\pm	Δ FWHM	\pm
CO Oxidation:	+0.22	+0.09	+0.29	+0.03	-0.06	+0.11
4-Nitrophenol:	+0.01	+0.08	+0.13	+0.03	-0.35	+0.10
1-Pentyne:	+0.01	+0.06	+0.08	+0.02	-0.21	+0.07
CB:	+0.28	+0.14	+0.35	+0.09	-0.01	+0.16
IWI:	-0.11	+0.16	-0.01	+0.10	-0.39	+0.18
Pd:	+0.10	+0.13	+0.17	+0.08	-0.16	+0.15
Au:	+0.07	+0.15	+0.17	+0.09	-0.30	+0.17
Al ₂ O ₃ :	-0.06	+0.17	+0.04	+0.10	-0.35	+0.19
SiO ₂ :	+0.21	+0.14	+0.28	+0.08	-0.06	+0.15
Total Averages	+0.08	+0.15	+0.16	+0.09	-0.20	+0.17

Table 3.2: Table showing the results of the catalyst damage study grouped by reaction and sample type. Data shown is averaged across all samples or reactions of that type, errors are a weighted average of the fit and numerical errors combined for each sample in its category.

room temperature. This trend is dominated by Pd/SiO₂ and to a lesser extent Au/SiO₂ MACS samples. Agglomeration on the multifaceted support seems less likely than settling of clusters into corner sites, and in the case of Pd/SiO₂, oxide formation, swelling the clusters somewhat.

Throughout all samples a general decrease in FWHM is observed, though all of this is under a 3σ significance. Two of nine samples fall outside the 3σ significance window as opposed to the 1 sample expected. This may be significant, but as it is not accompanied by accompanying increases in cluster size it is not considered significant. Further to this point, such changes would require removal or obscuring of small and large clusters concurrently, and while this seems feasible for small clusters, it would appear non-physical for those on the large end of the distribution.

3.8 Matrix-less deposition

During the course of palladium sample production, the matrix was measured at a higher temperature, in the region of 40 K; too high for Argon condensation to occur. This was initially attributed to a temperature sensor error, as delicate electronics contained within sputtering/evaporation systems are wont to develop minor and/or high resistance short circuits. It was assumed that the Wheatstone bridge circuit used to measure the resistance of the Rhodium-Iron temperature sensor had developed a short at the matrix. After three separate depositions the problem persisted and it was discovered that the temperature issue was being caused by an enlarged hole in the Tantalum heat shield of the evaporator. Tantalum, as with other refractory metals alloys with deposited Palladium, forming a low melting point alloy, which melts and widens the aperture, decreasing thermal radiation shielding. A new heat shield was formed, reinforced with sputter coated Al_2O_3 and sample production continued. As such the produced sample was produced without a matrix, with direct atomic deposition. The sample produced with a warm matrix was characterised and tested along with the MACS Pd/ Al_2O_3 sample already covered in this chapter. Both Pd/ Al_2O_3 samples were tested for their Palladium and Copper loadings by ICP-MS inspired partially by the results of carbon monoxide oxidation in figure 3.10, and partially by the matrix-less deposition. The direct deposition sample was found to have 0.04wt% Pd, and 0.03wt% Cu. The standard MACS sample was found to contain 0.02wt% Cu and 0.06wt% Pd. Considering the deposition times, the ratio of palladium between the two is reasonable, however the matrix-less

sample is 40wt% Cu, and even with the matrix, the sample is 25wt% Cu. As such, some copper from the support is being sputtered into the final sample despite the matrix.

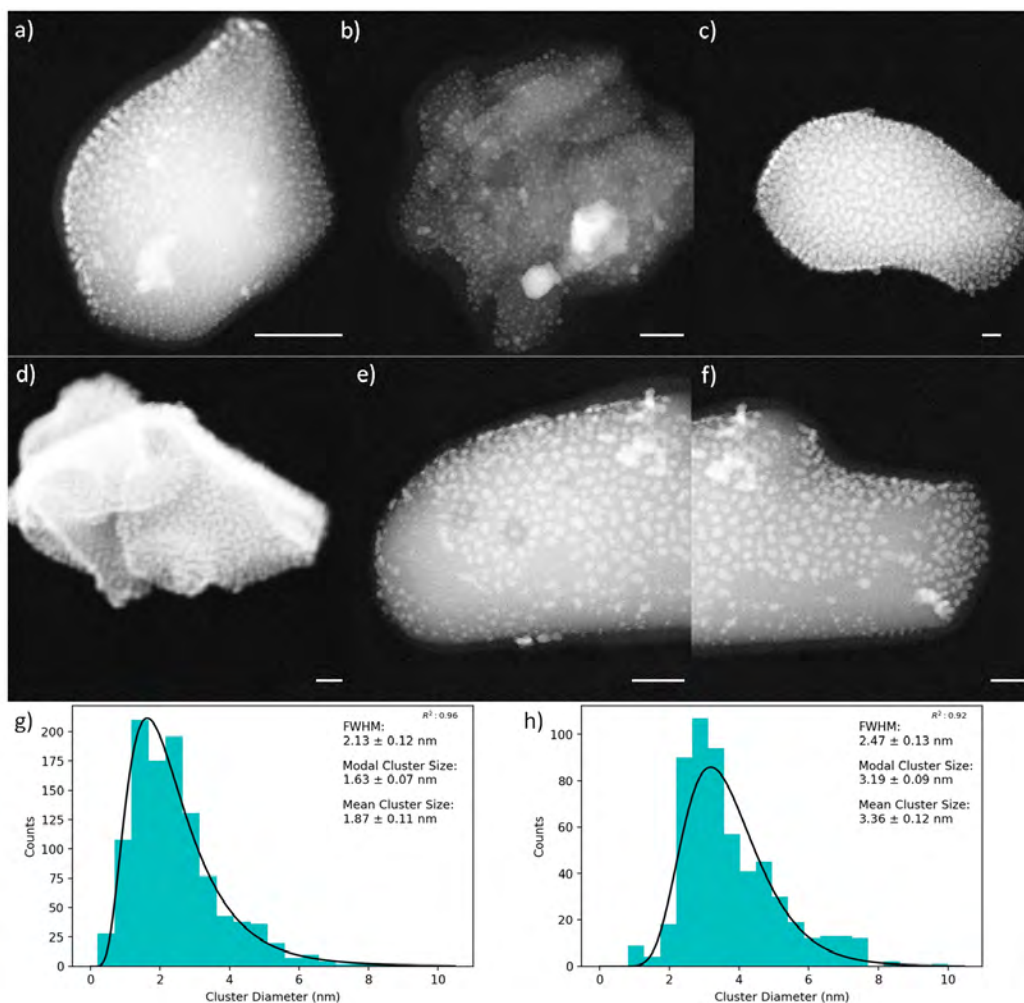


Figure 3.13: STEM characterisation comparison of a)-c) MACS produced Pd/Al₂O₃ and d)-f) matrix-less Pd/Al₂O₃. g) the size distribution of MACS produced Pd/Al₂O₃, h) the size distribution of matrix-less Pd/Al₂O₃. Scale bars are 20nm

Both samples were imaged using STEM, shown in figure 3.13. Qualitatively, it is possible to see for MACS samples that clusters tend to be

circular and isolated. In the case of the matrix-less sample, clusters appear to be a series of islands with defined width channels separating them. The matrix-less sample also demonstrates areas where cluster size is proportional to material density as would be expected from simple sputtering. If we turn a critical eye on MACS samples similar areas can be observed there, see figure 3.13 c) though they are significantly less common, indicating that the MACS too undergoes some atomic deposition. While this is to be expected as sputtering a matrix will produce some lone atoms, this may also indicate areas sputtered off the back plate. It must also be noted that the clusters observed in the matrix-less sample are significantly larger than their MACS counterparts, though appear to be of uniform height when observed at the edge of the particles. As such the assumption of spherical clusters is likely exacerbating the analysis.

Both matrix-less and MACS samples underwent the same catalytic testing as those throughout the rest of this chapter. Both samples demonstrate remarkably similar results, with the matrix-less sample achieving full conversion for both carbon monoxide and 1-pentyne slightly later than the MACS sample, which may be explained by the increased palladium loading. Interestingly, for CO oxidation the matrix-less sample lights off slightly earlier than the MACS sample. This is attributed to the differing support interaction between atomic and cluster deposition. In the reduction of 4-Nitrophenol, the matrix-less sample once again demonstrates a faster initial reaction, but tails off sooner. This is likely due to the increased copper content in the sample. Copper, as with many metals is somewhat active for the reduction of 4-nitrophenol particularly in alloy form[28, 118], and is likely to be respon-

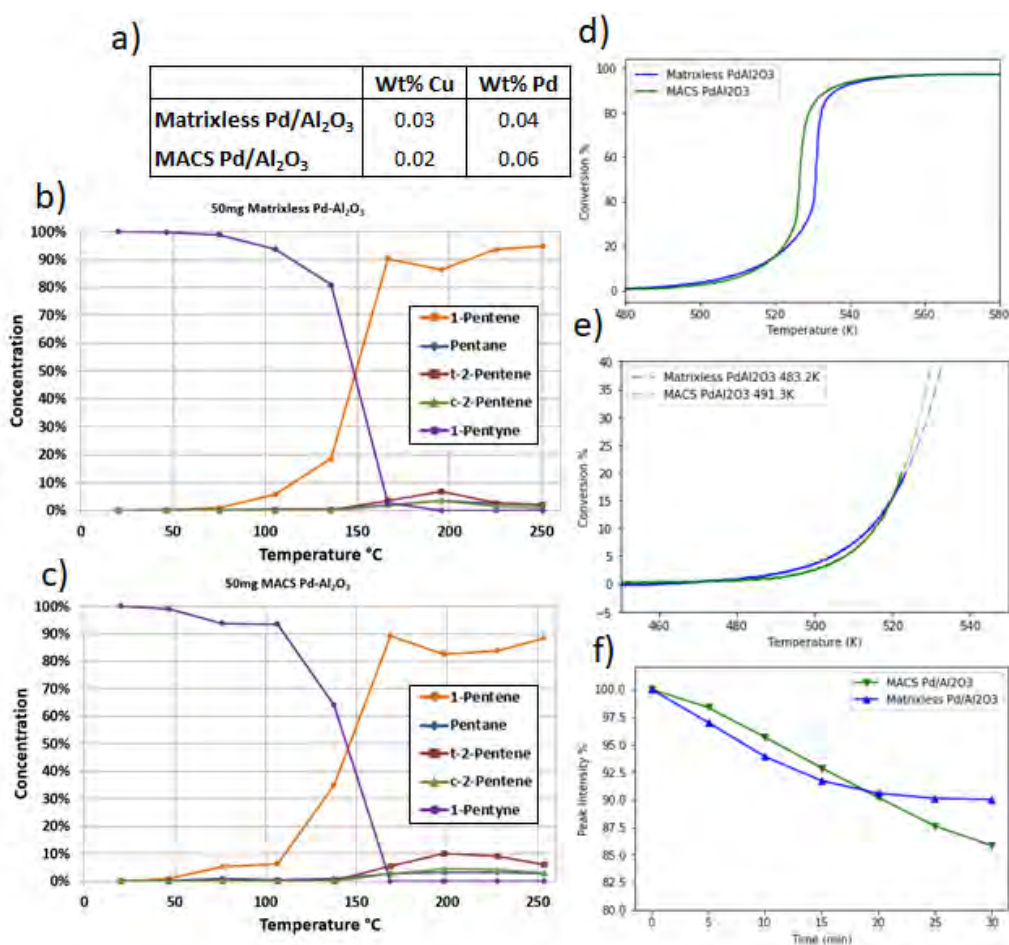


Figure 3.14: Catalytic reaction comparison between matrix-less and MACS Pd/Al₂O₃ samples showing a) the results of ICP-MS for samples metallic content, b) and c) the behaviour of matrix-less and MACS Pd/Al₂O₃ for the selective hydrogenation of 1-pentyne respectively. d) and e) show the reaction progress and light off temperature of both samples respectively. f) compares the samples responses in the reduction of 4-Nitrophenol

sible for the differences in activity. Besides these relatively small differences, primarily explained by composition, rather than production method, the two catalysts demonstrate remarkably similar behaviour across all testing fields. It seems that the in-vacuum/metal to metal/solvent free nature of these samples is the key factor in determining their catalytic behaviour, rather than

the distinctions of cluster production or cluster size.

3.9 Summary and Conclusion

This chapter has focused on the scale up and adaptation of the MACS unit for deposition onto powdered substrates. The MACS system was developed in reflection mode, scaled up and characterised in order to produce samples that could be compared with those produced by standard chemical means. For the purpose of this project, incipient wetness impregnation was chosen for its simplicity and flexibility. MACS catalysts were produced alongside IWI prepared samples. Palladium and gold were deposited onto alumina and silica powders, characterised using aberration corrected STEM to determine the nanoscale structure of the materials and acquire a size distribution of deposited clusters. These samples were tested for their activity in the oxidation of carbon monoxide, the reduction of 4-nitrophenol and the selective hydrogenation of 1-pentyne.

MACS samples demonstrate average cluster sizes of 1.7-2nm with distribution widths of 1.7-2.7nm. Impregnated samples demonstrate both larger sizes (2-5nm) and distribution widths (~3nm). Impregnated palladium samples demonstrate the highest activity and lowest light off temperatures for the oxidation of carbon monoxide, with MACS palladium samples also demonstrating activity. MACS gold samples demonstrate some activity for this reaction while impregnated gold samples demonstrate no activity, likely due to the remaining effect of Cl^- ions from the solvent. The differences between MACS and IWI samples for this reaction are thought to be due to the forma-

tion of the support/cluster interface, as well as the differing loadings whose effect is amplified by the exothermic nature of the reaction. Alumina samples demonstrate higher activity than silica as expected, likely due to their ability to donate oxygen to the clusters, though this could also be due to a lower surface area, allowing the exothermic positive feedback loop to occur more rapidly. All samples demonstrate activity for the reduction of 4-nitrophenol, with gold samples demonstrating increased activity over palladium. MACS Au/Al₂O₃ shows the highest rate when normalised by metal content likely due to its increased dispersion. MACS Pd/SiO₂ shows the highest normalised rate of palladium samples likely for similar reasons. It is difficult to pull any overall trends from this reaction, its sensitivity to very small quantities or very low loaded catalysts is desirable in many situations, however its progress appears to be dictated in the main by reactant concentrations, rather than particular catalyst properties and as such does not lend itself particularly well to such analysis where other alternatives are available. In the selective hydrogenation of 1-pentyne significant behavioural differences between MACS and IWI samples are observed. Gold based catalysts were found to be inactive for this reaction as expected and as such are excluded. MACS samples demonstrate particular inactivity to the conversion of 1-pentyne at low temperatures, while at room temperature IWI samples demonstrate full conversion, in the main to the undesired pentane. At higher temperatures all catalysts produce pentene at an increased rate, however MACS samples, likely due to their exceptionally low cluster size and distribution[119] are inactive for the conversion to pentane, producing pentene with ~90% selectivity. MACS Pd/SiO₂ samples demonstrate the highest selectivity, likely

due to the increased surface area allowing for the smallest and narrowest size distribution of the produced samples. Finally a Pd/Al₂O₃ sample was produced without an argon matrix. This sample was therefore a simple sputter deposition, with atomic mobility leading to cluster formation on the surface. This sample was tested for its catalytic activity in the same way as the others, and was found to demonstrate almost identical activity for all reactions as the MACS Pd/Al₂O₃ sample and as such the difference between the catalytic activity of MACS and IWI samples was attributed in the main to the effect of the solvent in the impregnation process. Both this sample and the MACS Pd/Al₂O₃ sample demonstrate significant ~30% copper content, this value being somewhat reduced by the protective properties of the matrix. While other samples were not tested for copper content, we see some evidence of it in gold samples when run for carbon monoxide oxidation, and it is reasonable to assume as matrix and deposition parameters were consistent across all samples. For the purposes of ‘real world’ catalyst production, perhaps cluster deposition, along with its complexity and associated consequences, is not an ideal method.

A note from the author: During the previous work, Richard Palmer left the university, taking the access to the MACS unit used in chapter 3 with him. While it would be preferable to continue with this method, addressing its flaws, these conclusions and the requirement for new equipment resulted in the MACS method being abandoned for the remainder of the project.

Chapter 4

The Clean Catalyst Source

4.1 Introduction

In response to the discoveries made in chapter 3, it was decided that catalyst formation could be performed by simple sputtering and achieve similar results to the MACS system while eliminating much of the complexity and time consuming nature of the process. However, leaving behind cluster deposition and relying on atomic diffusion and cluster nucleation introduces some new considerations. In such a system, the final produced structure is far more dependent on the surface/metal interaction, as shown in figure 2.12. Even remaining in the Volmer Weber growth mode, variation in surface/metal interaction energies will cause changes in surface diffusion length and thus change the final cluster size and number density. We must also consider the intrinsic link between coverage and cluster size, requiring a tighter control on the material deposited per unit area. It is worth noting that cluster deposition systems will also suffer from this effect at higher coverage,

producing dimer and trimer peaks in the size distribution. As catalyst production consistently relies on high metal coverage to achieve desired activity, it may be that surface agglomeration is more suited to catalyst production despite its relative simplicity. This will naturally not be the case where lower activity is acceptable for high selectivity catalysts, such as in the pharmaceutical industry. Eliminating the cooling and dosing steps of the MACS, the rate of catalyst production could also be vastly accelerated, and the relative simplicity of the system makes scale up a simpler prospect.

4.2 Initial tests

While surface agglomeration forming clusters is a well documented phenomenon, it is important that initial samples are made in a similar manner to ensure that there is sufficient surface interaction to prevent deposited material gathering on step edges or other macroscopic defects. It is also important to see how different materials may interact during formation of binaries.

4.2.1 Equipment

For these initial tests, the costs and setup were kept to a minimum. The MACS 2 unit was repurposed using the target clamp shown in figure 4.1

The target shown in figure 4.1 is a standard worn 99.99 + % gold 2” magnetron sputter target used in a simple sputtering (non-magnetron) configuration. A 99.99 + % silver target is mounted on the reverse side for binary formation. The target is grounded through a standard multimeter, measuring the sputter current. The target is sputtered by a Kaufmann and



Figure 4.1: The design of a magnetron target clamp, showing from left to right; the basic 3D design; the completed clamp mounted on a magnetic transfer arm; the completed clamp with worn magnetron sputter target held in place.

Robinson KDC10 ion gun. The target is designed to minimise the sputtering of the aluminium clamp, which may contaminate the sample. Sputtering of the threaded rod mounts is considered negligible for these applications.

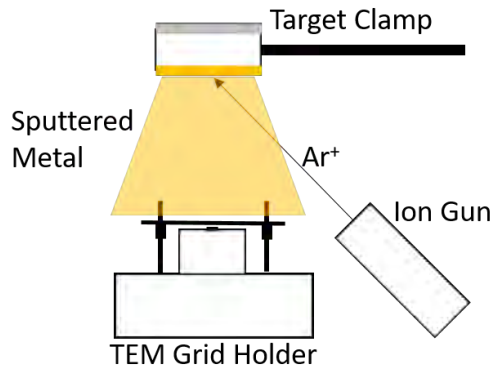


Figure 4.2: The deposition geometry of the test setup. The distance between the ion gun aperture and the target is 12cm . The distance between the target and the TEM grid is 6.5cm . The TEM grid holder is a six grid revolver style holder.

The following samples in this section were deposited using the deposition geometry shown in figure 4.2

4.2.2 Test Samples

Test samples were deposited in a horizontal fashion onto amorphous carbon TEM grids. These grids were previously swept through the Al_2O_3 support, attaching small particles to the surface with Van der Waals forces. This allows analysis of the formation of particles on the carbon film as well as the support and allows comparison of the two regions. Due to availability, test samples were made using Au and Ag. These were treated as analogues to the catalytically more interesting Pd species used later in the project. These samples were used to investigate the formation of monometallic and binary clusters on Al_2O_3 and SiO_2 as well as their thermal stabilities.

Monometallic Formation

Initial samples were deposited for a variety of different times to determine optimal deposition conditions. Due to the ease of imaging and thus analysis, Au was used as the test material.

Figure 4.3 shows the initial samples made using a direct sputtering method. The times were chosen based on a QCM reading of $0.2\text{\AA}s^{-1}$. As such the three initial depositions represent approximately 0.5, 1 and 3 monolayers coverage. It is possible to see from the above data that the formation mechanics between the carbon and Al_2O_3 surfaces are broadly similar, with the Al_2O_3 demonstrating marginally wider size distributions. This is likely due to macroscopic surface features: step edges causing larger scale agglomeration and angled surfaces receiving less material per unit area.

Mean sizes of these samples were plotted against deposition time with

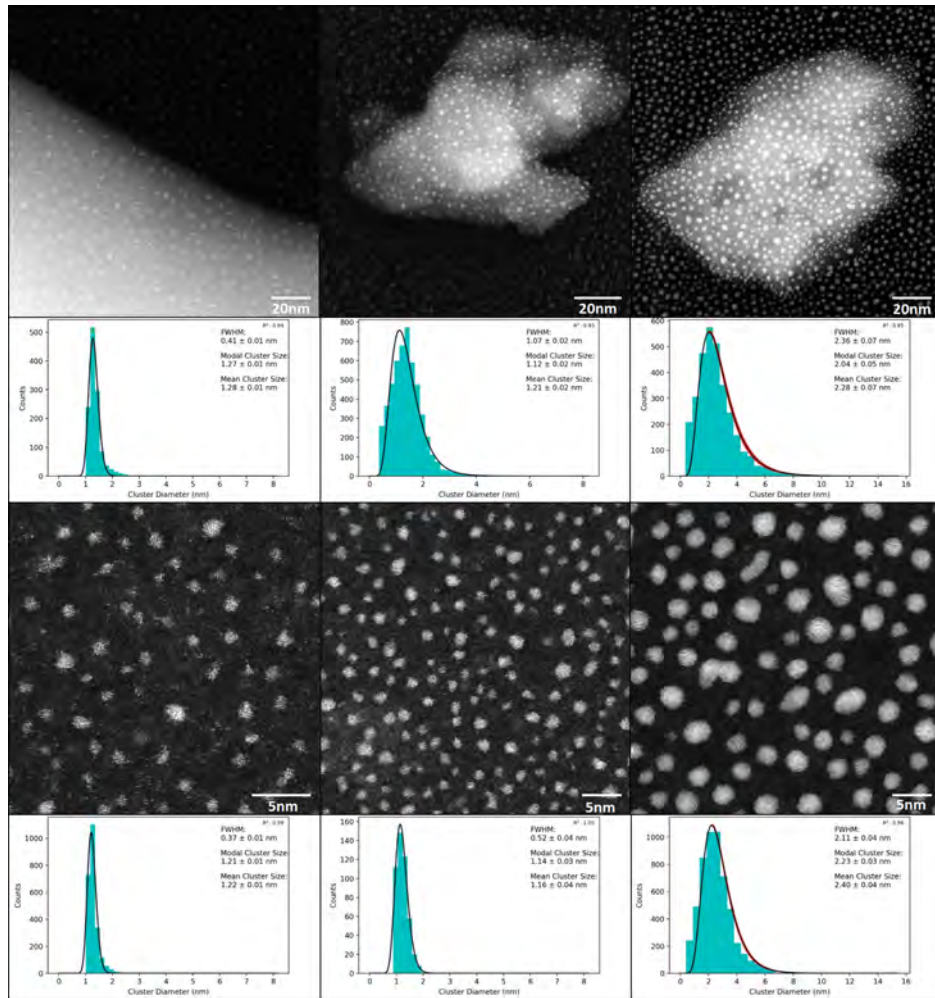


Figure 4.3: Initial depositions of Au on Al_2O_3 studded carbon TEM grids. From left to right 5, 10 and 30s depositions using a sputter current of 0.68mA. The top row shows the deposition on Al_2O_3 , the lower row, on the carbon TEM grid film. The size distributions relate to the images above them. Images are representative of the samples, size distributions are cumulative across all images taken. Note the scale of the 30s deposition size distributions

extra samples deposited for 15, 45 and 63s as shown in figure 4.4. The mean size follows a power law of $y = 0.56x^{0.33}$ with an R^2 value of 0.96. This implies the formation of three dimensional clusters with little preference for vertical or horizontal growth. Clusters formed on carbon show a somewhat

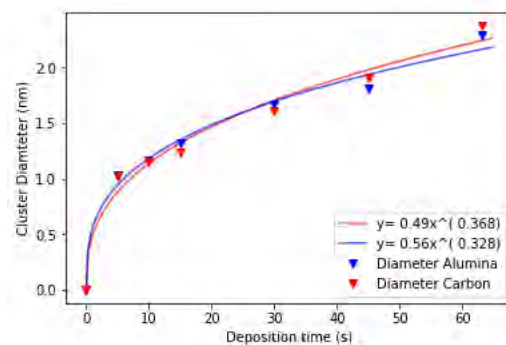


Figure 4.4: Cluster size as a function of time for initial depositions of Au on Al_2O_3 studded carbon TEM grids. Showing average cluster diameter on Al_2O_3 (blue triangles) and on the carbon film (red triangles). The fits show the power law followed by each size distribution with parameters listed in the legend (blue: Al_2O_3 , red: Carbon).

higher power law dependence, though this is simply attributed to counting error.

Cluster size was shown to be invariant with respect to deposition energy when normalised by the effect this has on sputter yield. Cluster size was also shown to be invariant as a function of deposition rate and sample temperature (during deposition) up to 473K as would be expected in heterogeneous agglomeration.

Bimetallic Formation

The differing aspects of control in physical over chemical methods inevitably leads to interest in binary clusters and what may be possible in this regard. Thus it is important to look briefly at a known system. Initial samples of AuAg alloys were deposited sequentially. These metals were chosen due to their differing masses, allowing for z contrast imaging in HAADF STEM.

This should allow any segregated binary structures to be clearly visible [120, 121, 122].

In such a system of surface agglomeration, it is reasonable to assume that monometallic clusters will form unless the surface is ‘saturated’ with nucleated clusters before the second deposition occurs. I.e. that there are no empty, defect rich areas larger than twice the mean free path of deposited atoms on the substrate. By analysing the nearest neighbour distance (NND) as a function of deposition time, it was determined that for Au deposition, saturation was reached after ~10s deposition at a sputter current of 0.69mA. See figure 4.5.

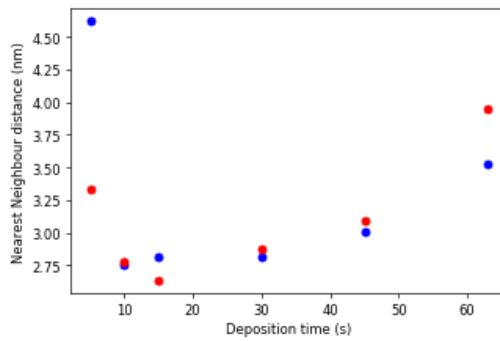


Figure 4.5: Mean first nearest neighbour distances, measured centre to centre of gold clusters formed over multiple depositions on a single TEM grid. Depositions were performed at a sputter current of 0.69mA. Red dots represent NND on the carbon film, blue dots represent NND on Al₂O₃. Surface saturation is said to be the point where NND is minimised. NND increases at larger deposition times as larger clusters merge into one another and are registered as a single cluster with a larger ‘watershed’. The larger NND demonstrated at 5s appears to be due to a lack of contrast between the smaller Au clusters and the background Al₂O₃.

Using the setup illustrated by figure 4.1, samples were produced by two 10s depositions of Au and Ag sequentially onto Al₂O₃ studded TEM grids

using a sputter current of 0.69mA . Samples were analysed using STEM. Segregation was observed by simple analysis of the z-contrast from HAADF STEM imaging, presence of alloys was confirmed using STEM-EDX.

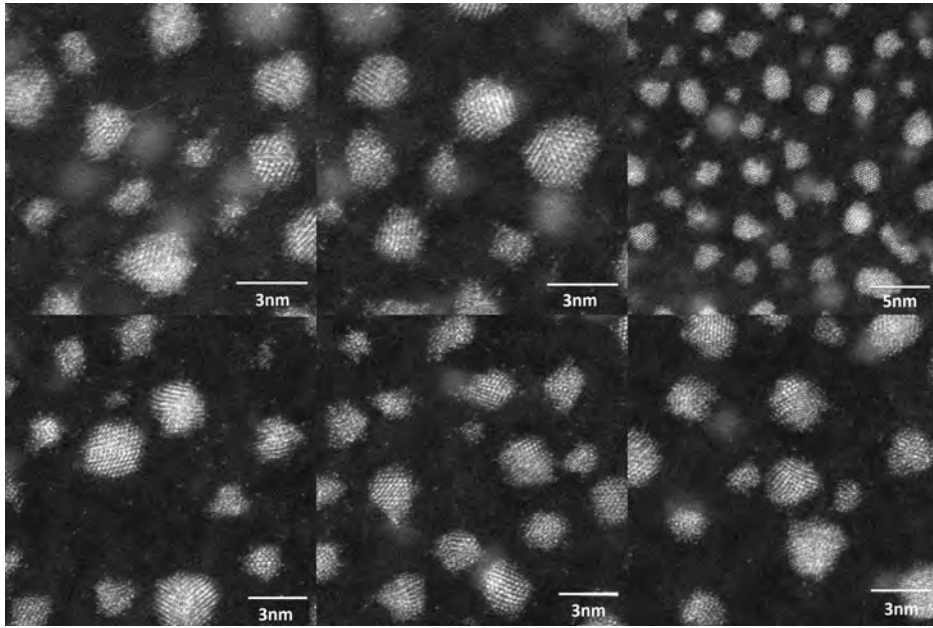


Figure 4.6: Initial images of AuAg binary clusters produced by sequential deposition of Au and Ag for 10s each at 0.69mA sputter current onto amorphous carbon. The top row shows Au first, followed by Ag, the bottom row shows images of samples formed with this deposition order reversed.

In figure 4.6, mottled effects can be seen in the intensity of the atomic columns within the clusters, particularly near the edges where the columns are only a few atoms thick, and thus there is a larger relative variance in the Z contrast. No particular segregation is observed as has been shown in the literature and no significant difference is observed between the samples when the deposition order is reversed. This information supports an alloying hypothesis, as would be expected from small clusters, and is confirmed using STEM-EDX.

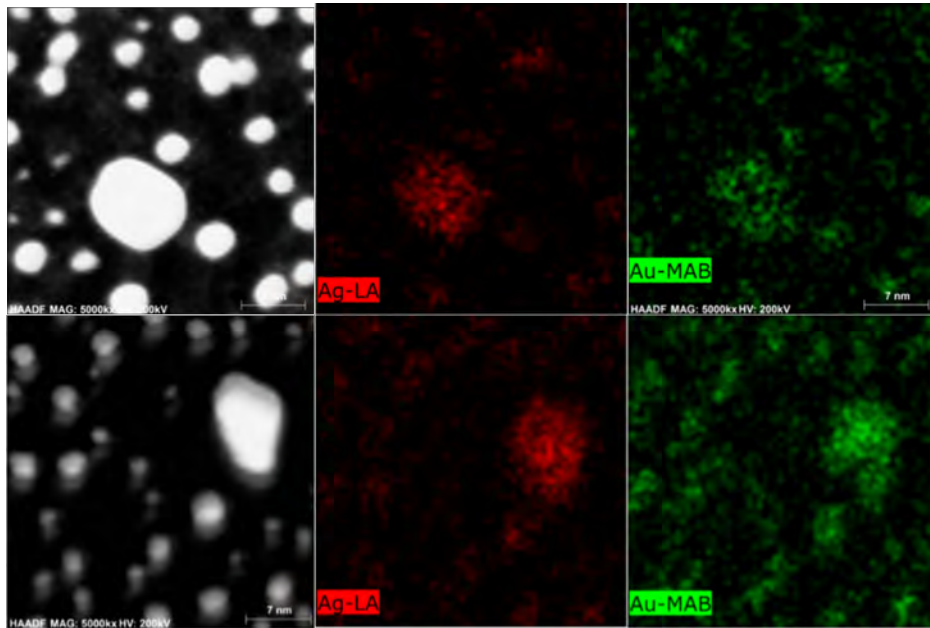


Figure 4.7: EDX mapping of clusters in figure 4.6. The top row shows the result of an Au-Ag deposition order, the bottom shows samples with this order reversed.

Figure 4.7 shows that the clusters observed are indeed AuAg alloys, and once again, no significant difference is observed between deposition orders. Larger clusters are favoured for EDX analysis due to the count rate of the EDX detector used. From this initial work it has been shown that it is possible to produce binary clusters and that these are likely to be alloyed at the size ranges found here. Samples were found to be stable at temperatures up to 573 K in air, with sintering behaviour restricted to the carbon support of thin films.

4.3 The Clean Catalyst Source Design

The fundamental requirement for such a system is a vertical deposition geometry onto an agitated powdered substrate. This could be done with a magnetron sputtering source, however the complications of having a higher pressure plasma, contained or otherwise close to a tray of insulating powder is likely to cause charging issues, expelling the powder. There is also the relative complexity and cost of changing metal in a magnetron system to consider. In terms of metal flux, magnetron sputtering is the best option, and as such is used in industrial systems such as those used by Exothermics inc[†] however greater flexibility is desired for small scale production and testing. As such, an ion gun and target setup was decided upon.

4.3.1 Target

Once an ion gun and target setup was decided upon, it was necessary to design a target. It is desirable to have a clamped film for target sputtering due to the cost of precious metal catalyst materials and the wide sputtering area desirable for large surface area depositions. There are a few considerations when designing a target for ion gun sputtering. It must be large enough to cover the ion beam, reducing contamination by stray ions sputtering other surfaces in the chamber. It must have a clear surface of sputter material, ideally a screw-less mounting system, again to prevent sputtering of these mounting points and contamination of the sample. A system with multiple

[†]Exothermics (<http://exothermicsinc.com>) appear to be the only company using physical deposition methods to form catalysts on an industrial scale, in the main for automobile catalytic applications. Information on their methodology is not widely available, however this does demonstrate industrial relevance.

mounting points for different target materials should be made, as this is fairly simple with the ion gun/target setup. Finally the sputter material should be electrically isolated from the chamber, enabling measurement of the sputter current directly, as well as charging of the target in order to focus the ion beam.

The target clamp was developed to be rotatable, and fill the chamber as much as reasonably possible, thus a triangular prism shaped target was developed with a screwless clamp design.

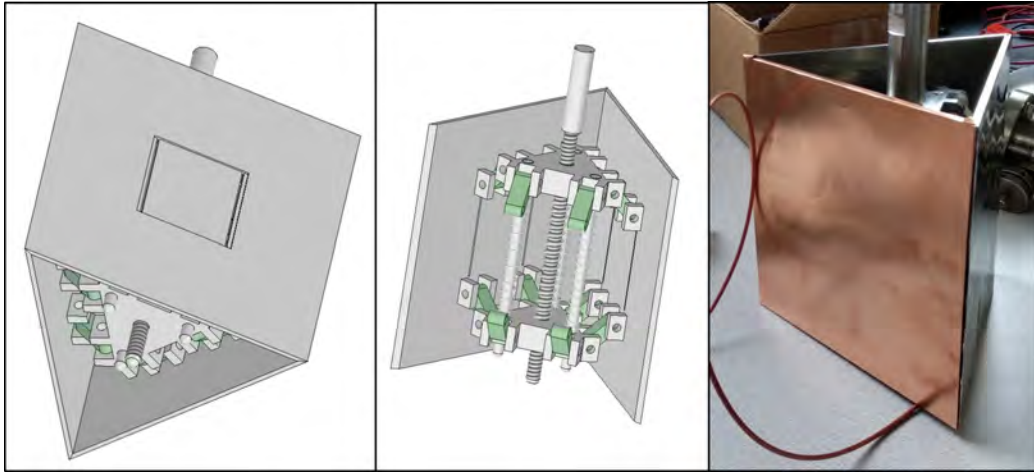


Figure 4.8: The design of the target clamp, showing left to right: The overall design with a central cut out for thick film placement, the internal compression mechanism for expansion and contraction of the clamp and the finished target with Pd and Cu films mounted. The cable is attached to a high voltage feedthrough used to measure sputter current and the green mounting arms are milled from PEEK for isolation, physical strength, lubrication and vacuum compatibility.

Figure 4.8 shows the design and final build of the target clamp. The clamp is mounted on a threaded rod, attached to a rotating magnetic drive. An M8 nut is used to compress the clamp axially, opening up the inter-

faces between the rectangular mounting plates. The rectangular plates are 148x150mm to allow clamping of a standard 150x150mm film bought from Goodfellow Ltd. The central cutout is 50x50mm with 1mm wide cuts through the plate 48mm apart to allow mounting of a 50x50mm secondary target underneath the primary film. As the ion current density follows a 2D Gaussian, with a maximum at the centre of the target, the primary film will sputter through, exposing the secondary film to the ion beam, allowing more efficient use of sputter material. NB: Bought films are consistently larger than quoted, and thus the cutout could be expanded to 55mm to take advantage of these slightly larger films. PEEK (Poly-Ether-Ether-Ketone) is a standard plastic for UHV applications, has a low coefficient of surface friction similar to the better known PTFE, high mechanical strength (hence preference over PTFE) and low vapour pressure. Thus PEEK is used for mounting arms isolate the mounting surfaces from the grounded central rod and expansion springs. A wire is taken from the mounting hardware of the outer plates, through a Super high voltage (SHV) feedthrough. The current is measured to ground from this feedthrough to ground using a standard multimeter, as the system uses sputter currents in the mA range.

4.3.2 Powder Tray

The primary concern for such a system is that each powder particle is exposed to the metal beam for an equal amount of time. This ensures an even distribution of active metal, and thus, a narrower size distribution. As such, accurate powder control is of primary importance. While powder rheology

is an important consideration in any such system, its effect can be somewhat minimised by piezo-agitation, minimising contact of the powder with the surface, and breaking up agglomerates. Piezo agitation systems are consistently used to control the flow of powder for nanofabrication applications [123, 124] and as such are of interest here. Taking these requirements into consideration, a piezo agitated, tilting, hopper to hopper deposition tray was designed. Keeping particles sheltered from the metal beam at either end, and exposed while they travel the distance in between. This tray must also be easily removable for cleaning and loading of powder.

During initial prototyping of the powder tray, it was quickly realised that a removable glass base would be necessary in order to achieve effective powder agitation over a smooth surface, as well as having the ability to clean sputtered metal off the surface. The ridges often found in metal sheet were found to disrupt the flow of powder significantly, and this effect was only partially eliminated by polishing the surface to a mirror finish, which would be required after every cleaning cycle. 1mm sheet glass however is cheap and readily available, can be acid cleaned effectively and provides a smooth surface. NB: many commercial glass techniques leave residual Zn contamination on glass surfaces. This can be acid cleaned before use if it is of concern. It is also technically difficult to accurately cut glass using standard score and snap methods. It was found that a Flow[©] waterjet cutter was best suited for this.

The skimming doors prevent powder ‘avalanches’ from the hoppers, and help spread the powder into a monolayer, with little powder shadowing. The powder is passed in between the hoppers multiple times during a deposition.

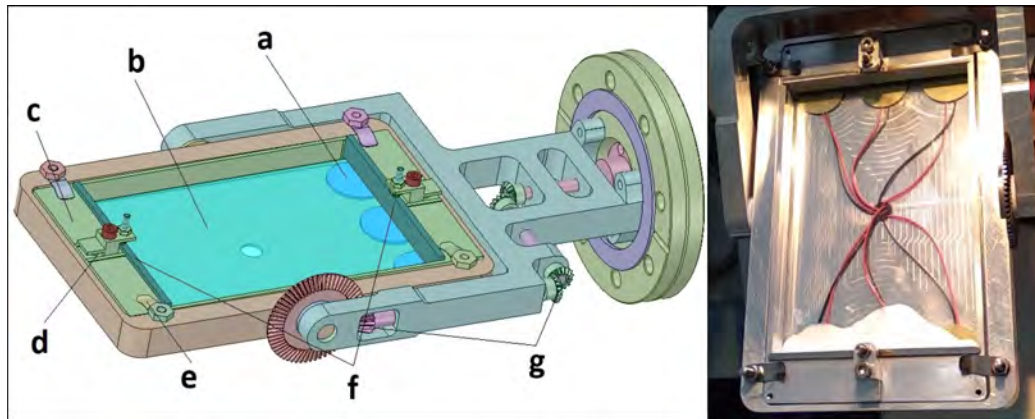


Figure 4.9: The design and final build of the piezo agitated deposition tray, showing a) Piezo Buzzers (RS electronics, product code: 724-3162), b) glass base, c) removable internal tray, d) vent/pouring hole granting access to the hoppers, e) microscope style sprung mounts, f) skimming doors separating the covered hoppers from the main tray area. g) The rotating mechanism, mounted to an external rotational magnetic drive. The image on the right shows the final built tray and mounting arms with piezo buzzers' wire and powder visible. NB: the image is taken under atmospheric conditions with the lower hopper over filled for the purposes of presentation.

Both the piezo agitation and charging effects assist in ensuring a smooth flow of monolayer powder.

The powder tray has two electronic components to it, the piezo buzzers' driving circuit and an Arduino controlled accelerometer to feedback the angle of the tray. The system was originally designed with a single Arduino Mega based control circuit, controlling the frequency and amplitude of the piezo buzzers as well as reading the tray angle. The system required two power supplies, 5V for the Arduino and 30V for the piezo buzzers. Due to issues with floating ground signals causing the Arduino to fail in operation, as well as the vibrational noise from the piezos rendering the signal from the accelerometer unreadable, this system was eventually split into two separate

circuits for the sake of reliability.

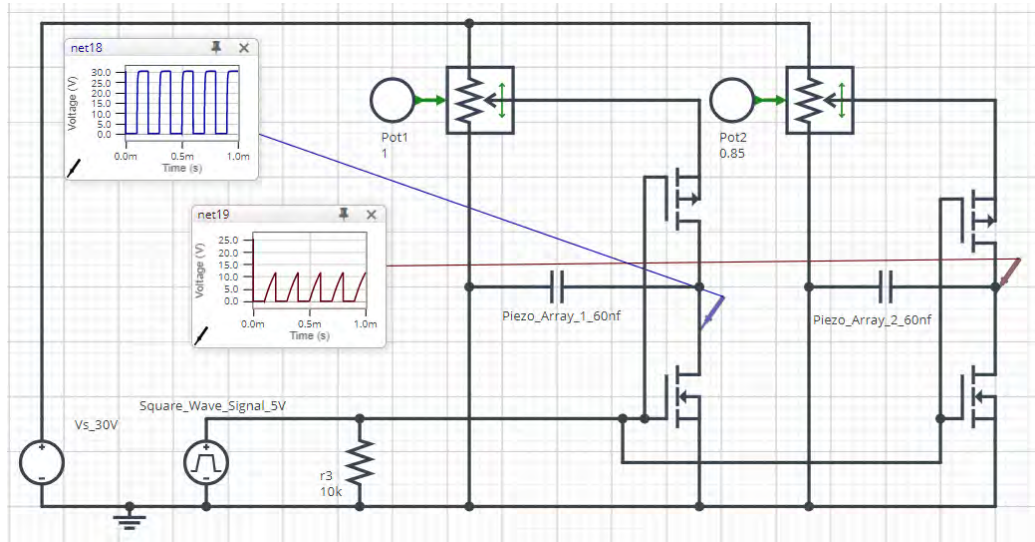


Figure 4.10: The final circuit design and simulation used to control the piezo agitation system of the CCS. Note that the potentiometers Pot1 and Pot2 have different setpoints. The main circuit supply is 30V and the square wave signal is 5V, 5kHz. The graphs represent simulated voltage to ground over a time interval of 1ms. The circuit design and simulation was done using SystemVision Cloud.

Figure 4.10 shows the circuit used to control the piezo buzzers. There are two separate banks of three piezo buzzers, each side, with a central buzzer, in interlocking ‘L’ shapes (see figure 4.9 for piezo layout). This was in order to control the motion of powder across the usual direction of travel, as powder will move towards areas of lower amplitude agitation. In practical use this was found to be unnecessary, and the potentiometer values remained equal throughout. Note that the amplitude reached does not scale linearly with the position of the potentiometer, as the capacitive piezo bank must charge through the upper resistance of the pot, with a characteristic RC value. This also means that the amplitude depends on the frequency of vibration, but

as this is fixed during use, it wasn't considered a significant issue. As can be seen from figure 4.10, 'net18' the wiper resistance (60Ω) is small enough that the RC effect is not significant for these voltages/frequencies.

In the initial setup the potentiometers were Analog Devices, SPI (Serial Protocol Interface) controlled digital potentiometers with 10bit (1024) setpoint serial number:AD5293BRUZ-20. These were controlled by the Arduino. The 5V square wave signal was produced by a digital output of the Arduino. The LCD display (Sain Smart IIC LCD2004) and accelerometer (Adafruit MMA8451) are I²C controlled. This combined approach was abandoned due to a floating ground signal interrupting the I²C communication with the arduino, and eventually causing the module to crash. The approach was abandoned for a more robust separated system using a repurposed PWM controller running at 50% duty cycle, 5.15kHz. This replaced the square wave signal in figure 4.9, and the digipots replaced with standard potentiometers. The Arduino remains as a read out for the accelerometer.

4.3.3 Full System Set up

The setup is completed by a Kaufmann and Robinson KDC10 ion gun, mounted in an angled flange fabricated by Kurt J Lesker Ltd.

Figure 4.11 illustrates the location and geometry of the components discussed in this chapter so far. These are contained in a 250mm internal diameter barrel chamber with a 160mm ID cross tube where the powder tray can be loaded and removed by hand (see figure 4.12).

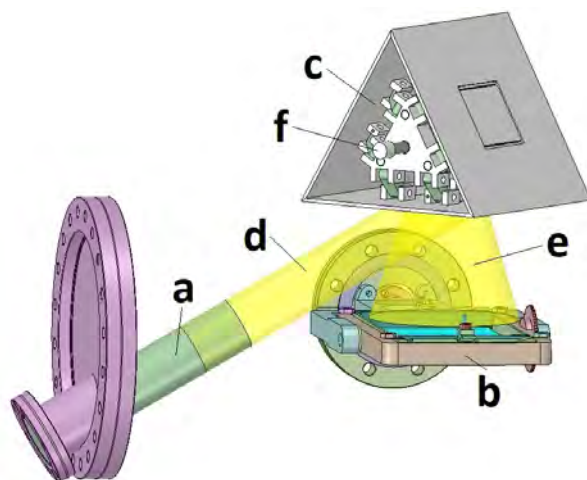


Figure 4.11: The final design of the functional components of the CCS in their correct locations. The chamber has been omitted for clarity. a) The KDC-10 ion gun, b) the powder tray, c) the target clamp, d) the ion beam, e) the metal beam and f) the point of attachment for the target clamp to demonstrate the axis of rotation

4.4 Standard Operating Procedure

The standard operating procedure is recorded here for a greater understanding of the process behind using the CCS to produce catalysts as well as being instructive for anyone who wishes to use the equipment in the future. Much of this section relates to figure 4.12 on page 96 for valve names and locations. Valves will be listed with letters from that figure.

4.4.1 Inserting Powdered Support

Once the main chamber is at atmospheric pressure, open the door and pour a measured quantity of powder into the centre of the tray. The hoppers have a capacity of approximately three cubic centimetres in use, this relates to approximately three grams of the Al_2O_3 powder used consistently in this

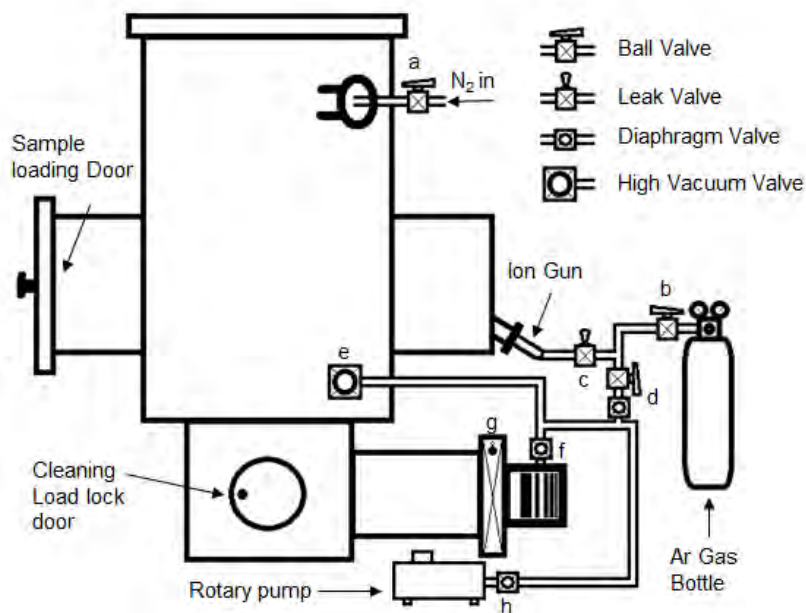


Figure 4.12: A simplified external chamber and vacuum diagram of the CCS illustrating the location of the valves for users. a) Vent valve b) Argon line valve c) Leak valve for ion gun d) SpeediValve™ for reliability and ball valve for line flushing. e) High vacuum valve allowing the chamber to be rough pumped while bypassing the turbo pump. f) SpeediValve™ for isolation of the turbo pump. g) Gate valve for isolating the turbo pump from the chamber. h) SpeediValve™ for emergency use.

work. The powder is poured into the centre of the tray to prevent it sticking in the hopper areas. Due, it seems, to the reduced level of adsorbed water under operating conditions, the support appears to stick less once the chamber has been evacuated. Any powder left on the centre of the tray should be swept off by the motion of the powder.

4.4.2 Pumping Down

The CCS has an isolatable turbo pump allowing it to remain in operation while the chamber is at atmospheric pressure or being rough pumped. Ensure the roughing pump is running and isolate the turbo pump by closing the turbo pump exhaust valve (f). The gate valve will also be closed if the turbo pump is running. Open the high vacuum valve (e) connecting the roughing pump to the main chamber. If there are any leaks in these valves the pressure will begin to increase behind the turbo pump, increasing the indicated load on the pump. If this happens, the high vacuum valve (e) should be closed, and then the turbo pump exhaust valve (f) opened to remove this pressure build up. Once the chamber has reached $< 5 \times 10^{-2} mBar$, close the high vacuum valve (e) and open the turbo pump exhaust valve (f). Finally open the gate valve (g) slowly, allowing the turbo pump to evacuate the chamber. Full evacuation to base pressure of $6 \times 10^{-7} mBar$ should take approximately four hours. If components have been removed for cleaning or porous/high surface area supports are being used, this may take longer due to the porosity or solvents used.

4.4.3 Deposition

Flush the lines: close the turbo pump exhaust valve (f). Ensure the line valve (b) from the Argon gas bottle is closed. Open the line vent valves (d) and pump down the lines to the Argon gas bottle. Close the ball valve (d) and refill the lines by opening the line valve (b). Pump and refill the lines three times or more to remove and reduce gaseous contaminants. Close the

line vent valves (d) and open the turbo pump exhaust valve (b). Set the pressure in the chamber to $1 \times 10^{-4} mBar$ using the leak valve (c). Turn on the piezo agitation ($5150Hz$, $30V$) and tip the powder into one of the hoppers by tilting the tray. Set the ion gun to the desired current ($5mA$ standard), enable ion discharge, and once values have settled, enable the ion beam. Note that the ion beam current setpoint is usually 25% higher than the measured sputter current. Tip the powder back and forth under the beam focusing on achieving a smooth monolayer flow of powder and ensuring that the entirety of the powder moves between the hoppers each pass. Time this process from the first pass under the beam. Once the powder has been coated for the required time ($\sim 5min$), turn off the ion gun power supply (manufacturer recommended). Close the leak valve (c) and the Argon gas bottle valve (b).

4.4.4 Venting

Close the gate valve (g), isolating the turbo pump from the chamber. If the turbo pump is to be turned off, do so now. Open the nitrogen valve at the wall. Open the vent valve (a) on the chamber partially, until a leak is heard, and allow the chamber to vent slowly. This helps prevent blowing powder out of the tray. Unfasten the chamber loading door, once the chamber has reached atmospheric pressure this will open.

4.4.5 Retrieving Sample

Wearing gloves, open the loading door and release the nuts securing the sprung clamps (figure 4.9c). Rotate the springs out of the way and remove the tray insert. Tip the tray's contents into a container through the vent hole (figure 4.9e), use of a glass funnel is recommended. Remove the glass base of the tray and clean it and inside the hoppers using a vacuum cleaner/nitrogen gun/solvent as required. The glass base can be acid cleaned or cleaned with an abrasive such as scotchbrite™ pads. No measurable contamination from metal deposited on the glass has been observed. Dry the tray components in an oven if required, reassemble and replace in the tray base, securing the sprung clamps by hand.

4.5 System Characterisation

Once the system has been built, it is necessary to characterise its behaviour and the types of sample that it may be possible to produce. Initially, the metal beamshape was measured by sweeping a quartz crystal microbalance (QCM) across the chamber along three paths to produce a 2 dimensional beam shape. Initially the QCM was placed centrally in the chamber, and the target tilted around the axis shown in figure 4.11 (f) to maximise the central flux[†]. The data was collected over three separate depositions at $5.0mA$ sputter current, and the metal flux measured as a function of position. The

[†]This is clearly not the optimal angle through which to rotate the target but is done this way due to chamber limitations. The case of an axis of rotation normal to the horizontal direction of the ion beam would be optimal, and in this case the variation in loading across the width of the tray would be more closely related to the metal/ion beam width.

data were normalised by the flux at the central point.

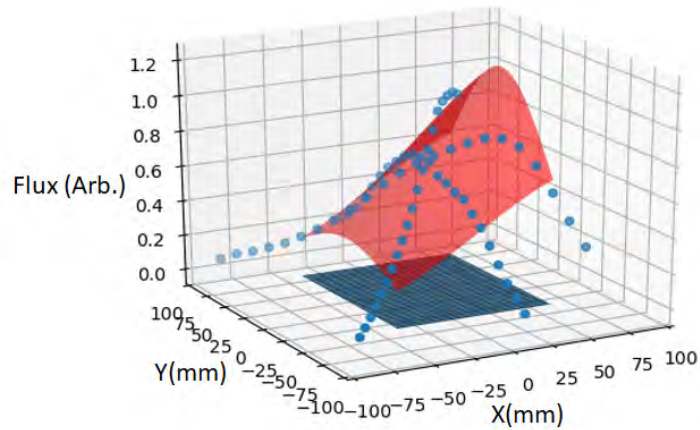


Figure 4.13: The metal beam shape as measured by QCM swept across the chamber along three separate angles. The data is fitted with a 2D Gaussian. The ion gun is located at (-250,0). The blue dots represent the normalised data, the blue area represents the exposed area of the tray, and the red area represents the metal flux over the tray area. The flux intensity peaks at (78, 1) with a sigma of 79mm or a FWHM of 186mm.

From this beamshape it is possible to see that the angle of the beam produces a Gaussian extended in the x dimension. The Gaussian peaks beyond the boundary of the tray, effectively wasting much material. As the tray tilts in the Y direction, it is reasonable to assume each particle follows a reasonably straight trajectory along Y. By integrating along the two Y-parallel edges of the deposition tray, we can obtain a maximum difference in exposure to the metal beam. This is done and we find that the particles travelling along one edge of the tray are exposed to 3.36x more metal than those on the other side. This is somewhat offset by multiple transits under the beam and powder moving along the x direction once inside the hoppers, so this should be treated as a theoretical worst case scenario in terms of

metal loading. Thus this will have a larger effect at lower deposition times and lower loadings, where the concern of producing a thin metal film is also decreased.

4.6 Initial Samples

4.6.1 Method Refinement

Initial samples were produced using Copper due to cost and availability. Samples were deposited for 3, 10 and 20 minutes using a sputter current of $5mA$. Piezo fluidisation was achieved using a $5.15kHz$, $10V$ square wave.

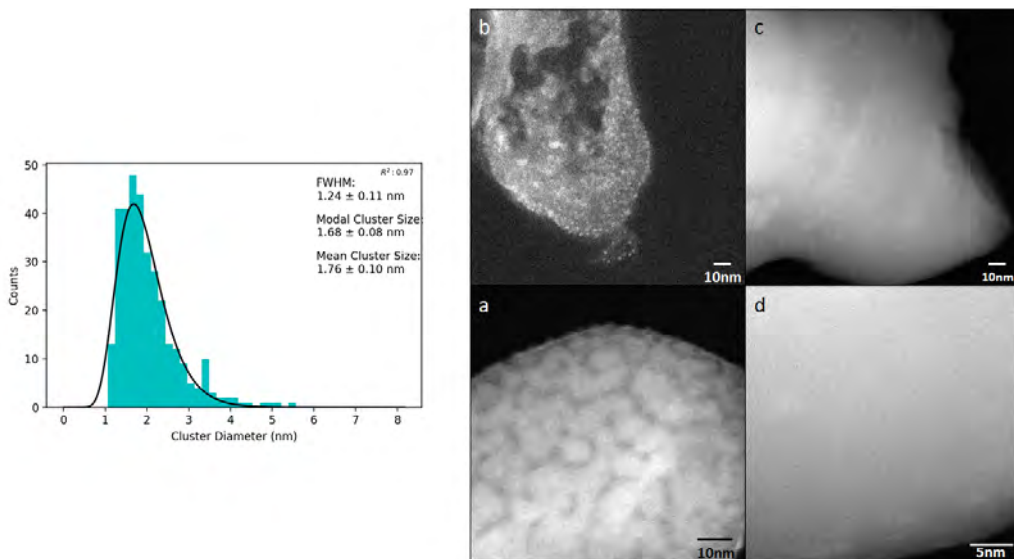


Figure 4.14: The first Cu/Al_2O_3 sample produced using the CCS. 3min, $5.0mA$; $10V$, $5.15kHz$ piezo agitation, 11° maximum tray tilt. Showing the overall size distribution and the range of deposited quantities observed a) to d) from high to low coverage.

Figure 4.14 shows the STEM analysis of the first powdered sample cre-

ated using the CCS: Cu/Al₂O₃. This sample shows a wide range of deposited material. The sample was created in four passes under the beam with a tray angle of $\sim 11^\circ$ creating slow moving agitated Al₂O₃, each pass taking approximately 45s. By maximising the time spent with the powder in the open rather than in the hoppers, the material deposited on the powder was maximised. Over a series of Cu/Al₂O₃ samples the piezo agitation was increased to 30V, the doors lowered such that a $\sim .25$ mm gap was left between the skimming doors and the glass base, and the deposition time increased to 5min. The tray angle was increased to $\sim 16^\circ$ increasing the number of passes under the beam to 21 ± 2 .

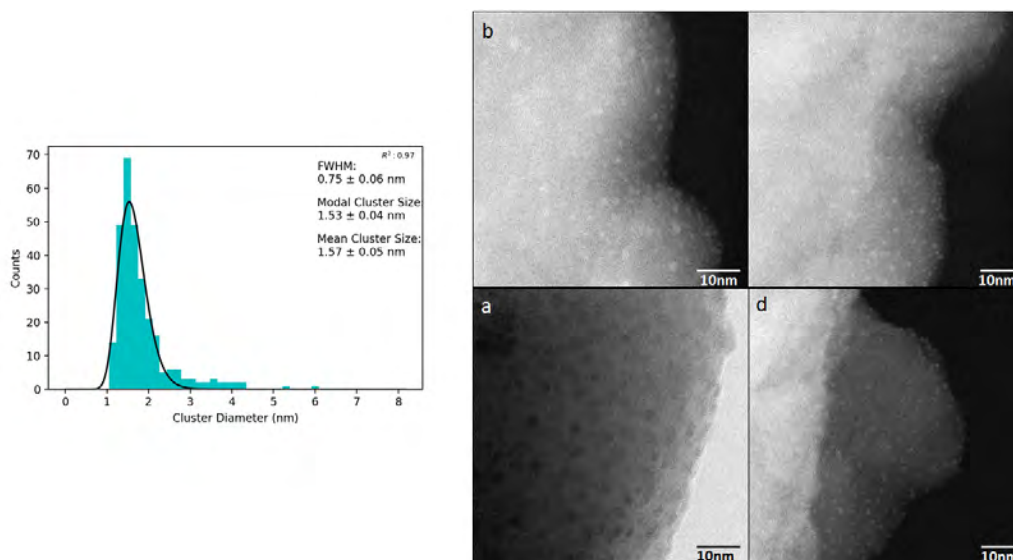


Figure 4.15: The final Cu/Al₂O₃ sample with the deposition method adapted. Deposited for 5min, 5.0mA sputter current, 30V, 5.15kHz piezo agitation, 16° maximum tray tilt. The figure shows the total size distribution and the range of deposited material from high to low coverage, a) to d).

The sample analysed in figure 4.15 demonstrates the final results of the improvement of the method resulting in a significant decrease in the distri-

bution width from $1.24 \pm 0.11nm$ to $0.75 \pm 0.06nm$ with mean and modal sizes within 2σ of each other. These size distributions do not include areas such as those shown in figure 4.14 a, as the image processing algorithm fails to identify a networked island structure as a cluster. Even if it was possible to identify these structures, it would be inaccurate to assume they are spherical, and much of the surface would be identified as a single cluster, not affecting the size distribution significantly. As such, these size distributions must be accompanied by a qualitative assessment of the images observed to ensure that the sample is homogeneous, at least across the observed particles.

4.6.2 Monometallic Homogeneity

It is necessary to consider how the beamshape and method affects the final size distributions of clusters produced using this system. This can be generally related to the FWHM of the size distributions of full sample testing. A narrower distribution should enable the final produced catalyst to have a far more specific and, in some cases selective response. This also enables the sample to be tuned to suit the reaction by shifting this size distribution. While there is a natural distribution width caused by the numerical process of cluster nucleation and agglomeration, increases to this are most likely due to differences in material deposition quantity. However as $ClusterSize \propto DepositionQuantity^{1/3}$ this effect, as seen in the size distributions, is somewhat muted, and enables a relatively narrow distribution to be achieved, close to the ‘natural’ distribution widths seen in figure 4.3. This analysis is done on a Pd/Al₂O₃ sample due to the increased contrast in

STEM, using the higher mass element. This enables a larger portion of the clusters to be identified, and thus the data suffers less from numerical errors.

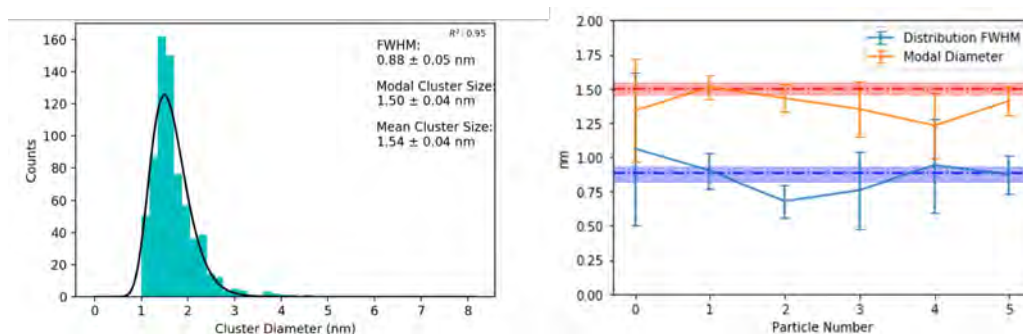


Figure 4.16: An initial Pd/Al₂O₃ sample showing the measured size distribution from the entire sample. The plot shows the modal cluster size and FWHM of a log normal fit of size distributions of clusters found on individual Al₂O₃ particles in the image set. Errors are calculated by combination of error on the fit and binomial error from the number of clusters measured

As can be seen in figure 4.16, cluster size and distribution width remains consistent across the sample within numerical error with the exception of the width of support particle two's distribution, which falls within two sigma. This is reinforced visually across the sample images. It must be noted that particles with too few clusters identified to plot an accurate distribution have been eliminated from the data. No powder particles have been observed in STEM without metal deposition. Mean cluster size across the sample varies by 10%, relating to a variation in deposited material of 30%.

4.6.3 Binary Homogeneity

As previously mentioned, investigations into sample homogeneity are a key factor in relating the nanoscale structure of a catalyst to its real world capa-

bilities, however confidence in sample homogeneity is also essential in such a system if it is to be used for creation of multiple-metal materials by sequential deposition. In such systems, the local metallic ratio plays an important role in the catalytic response, particularly in the selectivity of the material. Once a single metal has been deposited the surface area must ideally be ‘saturated’ with monometallic clusters in order to prevent monometallics of the second metal forming in the undeposited areas. Likewise, the second metal must be evenly distributed in order to make contact with the entirety of the sample, producing truly binary clusters rather than a mix of monometallics.

Initial samples were produced using palladium and copper due to their catalytic interest[125, 126], contrast in HAADF-STEM, and in order to achieve comparable results to chapter 3. samples were produced using a variety of targets in order to quantify their effectiveness at producing desirable binary clusters. Sequential deposition was compared to a strip target, with the copper strip aligned normal to the direction of powder flow. A central geometry with a palladium central disc in a copper target was also investigated. Produced samples were analysed using quantitative EDX of entire support particles to maximise the signal and minimise contamination over a ten minute exposure time. The purpose of this test is to attempt to optimise the formation of homogeneous binary particles, and decide whether a differing target geometry is required.

As can be seen from figure 4.17 no significant difference in metallic ratio standard deviation is observed between sequential deposition and a centrally mounted secondary metal target. Use of a strip target should decrease this variation of deposited material where the standard deviation is considered.

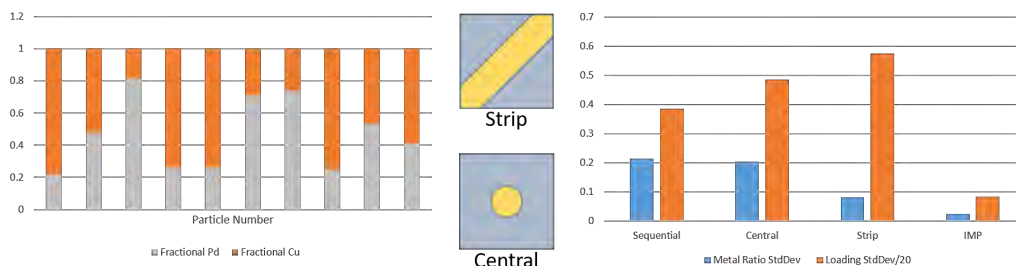


Figure 4.17: Quantitative EDX analysis comparing sequential deposition (left) to a centrally mounted circular Pd target, a Cu strip placed horizontally across the target, normal to the direction of powder flow, and an impregnated $Pd_{10}Cu$ sample. (Left) example of the raw data of a sequentially deposited PdCu sample demonstrating the differing metallic ratios across the sample, (centre) target geometries used for the strip and central deposition and (right) the standard deviations of the metallic ratios and loading per particle

The standard deviation should now be due primarily to the difference in the ‘flatness’ of the beam at each end of the tray (see figure 4.13). The higher intensity of the beam profile between the central copper portion of the target as opposed to the palladium at the edges gives rise to a set of copper rich particles being produced at one edge of the tray while the other edge sees a far flatter material profile, with the produced particles being more even binaries. Impregnated samples see a particularly low standard deviation of material, though as mentioned in chapter 3, impregnated samples display little apparent material and data is based on single clusters on otherwise naked particles. It is of course understandable that impregnated samples have a particularly low metallic ratio standard deviation due to the atomic process of mixing in the salt precursor.

It was decided that the benefits of compound targets were limited, as a new target is required for a different metallic ratio. If this was to become

a limiting factor in future work, gridded overlays of the second material would be used to control the relative fluxes of the two metals, with different transparency grids used for loading control.

4.7 Catalytic Testing

Once the CCS has been shown to produce materials that appear similar to model catalysts under an electron microscope, it is necessary to demonstrate this activity in real world. For the sake of comparison the reactions are kept consistent from chapter 3, with the exclusion of 4-nitrophenol reduction. This decision was made due to the lack of insight gained from the reaction. As it can be triggered by the presence of many transition metals, and is usually done at a very low concentration, the reaction does not offer much information on the catalytic performance of these materials, merely confirms activity in the case of very low assay catalysts. Thus, testing in this section consists purely of 1-pentyne hydrogenation and carbon monoxide oxidation of initial Pd/Al₂O₃ and PdCu/Al₂O₃. The PdCu/Al₂O₃ samples are formed at ~20% Cu in order to mimic the MACS samples from chapter 3 and analyse whether the back-plate contamination has a significant effect on the catalytic response of the samples. PdCu/Al₂O₃ samples are formed using sequential deposition.

4.18 shows the STEM analysis of the initial Pd/Al₂O₃ and PdCu/Al₂O₃ samples at different loadings, as determined by ICP-MS. Sample a) is a Pd/Al₂O₃ sample at 0.006wt% Pd, sample b) doubles this loading for a 20% increase in average cluster size (26% or 2^{1/3} expected). Sample c) is

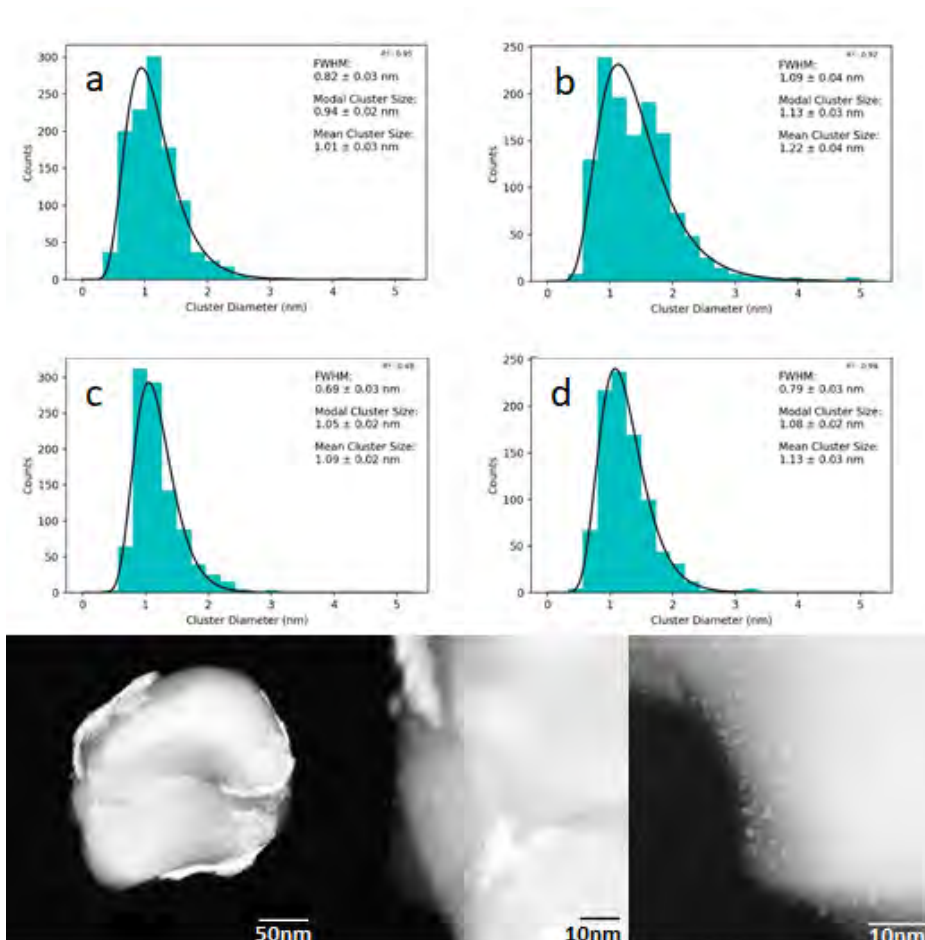


Figure 4.18: STEM analysis of initial monometallic and binary particles showing size distributions for a) 0.006% Pd/Al₂O₃, b) 0.012% Pd/Al₂O₃, c) 0.004% Pd, 0.001% Cu/Al₂O₃, d) 0.008% Pd, 0.001% Cu/Al₂O₃. Images are of sample d, demonstrating how it disobeys the trend. As before in figure 4.7, binary particles are found to be alloyed

a 0.004% Pd, 0.001% Cu/Al₂O₃ and sample d) doubles the Pd loading retaining the Cu loading. A negligible increase in cluster size is observed with a slight increase in distribution width. This is somewhat explained by the large structures observed in the images shown in figure 4.18 which are not registered as clusters in the size distribution.

Impregnated analogues were also formed at an equivalent loading of 0.005wt% Pd and PdCu. These samples were characterised using STEM and ICP-MS.

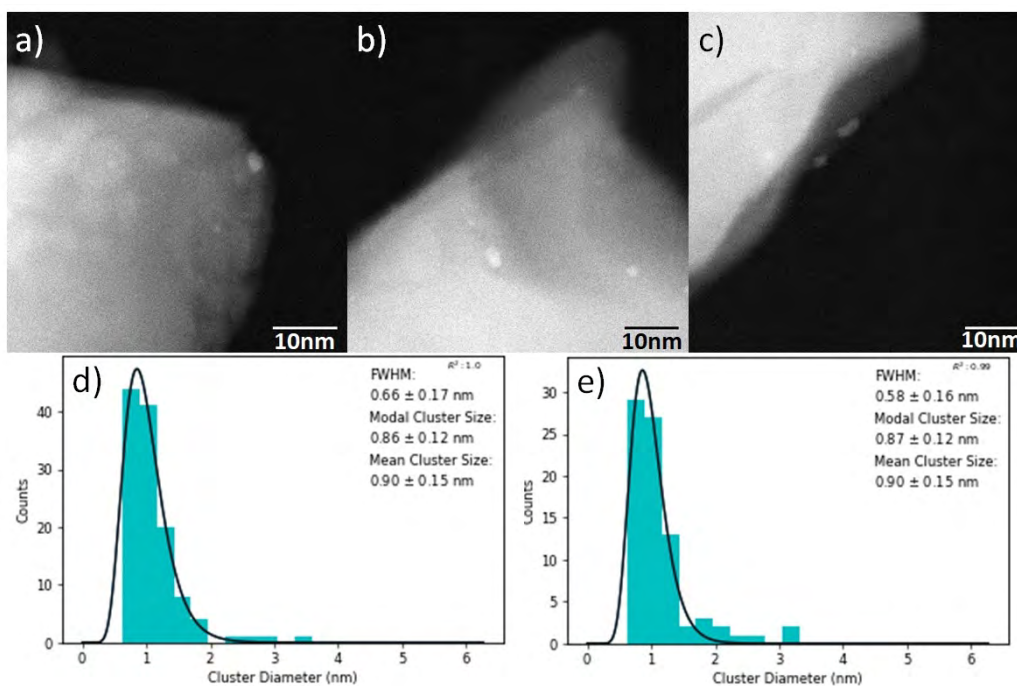


Figure 4.19: STEM analysis of impregnated Pd and PdCu particles on Al₂O₃, showing a), b) example STEM images of Pd/Al₂O₃ and c) PdCu/Al₂O₃. Both samples are qualitatively indistinguishable in STEM. d) and e) show the size distributions of Pd/Al₂O₃ and PdCu/Al₂O₃ respectively.

As shown in figure 4.19, very few metal particles are observed on the samples, though a very narrow size distribution remains with average cluster diameters <1nm. The lack of observed metal is attributed to the ion exchange phenomenon mentioned in section 3.4, however in these samples it is amplified, as cluster formation will occur once the surface is saturated with Pd.

Sample Summary

Quantitative analysis of all samples produced is summarised here for reference and comparison.

Sample	Loading(ppm)	Mean \varnothing (nm)	FWHM(nm)
CCS H <i>Pd/Al₂O₃</i>	120Pd	1.22 \pm 0.04	1.09 \pm 0.04
CCS H <i>PdCu/Al₂O₃</i>	10Cu 80Pd	1.13 \pm 0.03	0.79 \pm 0.03
CCS <i>Pd/Al₂O₃</i>	60Pd	1.18 \pm 0.04	0.69 \pm 0.05
CCS <i>PdCu/Al₂O₃</i>	11Cu 40Pd	1.02 \pm 0.04	0.71 \pm 0.05
IWI <i>Pd/Al₂O₃</i>	55Pd	0.90 \pm 0.15	0.66 \pm 0.17
IWI <i>PdCu/Al₂O₃</i>	7.4Cu 54Pd	0.90 \pm 0.08	0.58 \pm 0.16

Table 4.1: Sample characterisation showing loading in ppm as measured by ICP-MS, mean diameter and size distribution FWHM as measured by a log-Normal fit of the STEM cluster size analysis. Errors are calculated by fit accuracy and number of clusters analysed. H indicates higher loading

4.7.1 Carbon Monoxide Oxidation

Initial sample activity is determined by carbon monoxide oxidation. Samples are tested after ICP-MS analysis and the quantity of palladium in the reactor is normalised. Loadings and quantities are listed in figure 4.20. The reaction is carried out in a tube furnace reactor with the catalyst sample resting on a quartz wool bung in a quartz tube. Reactant gas of 1% *CO*, 20% *O₂* in *He* is flowed through the catalyst bed. The gas is then analysed using an infra red absorption spectrometer, calibrated at room temperature with reactant gas. The tube furnace temperature is ramped at 5°Cmin⁻¹ and the *CO* concentration monitored to determine conversion. In order to keep the data consistent with previous experiments, the flow rate of 10ml/min remains to allow for comparison between these samples and those in chapter 3

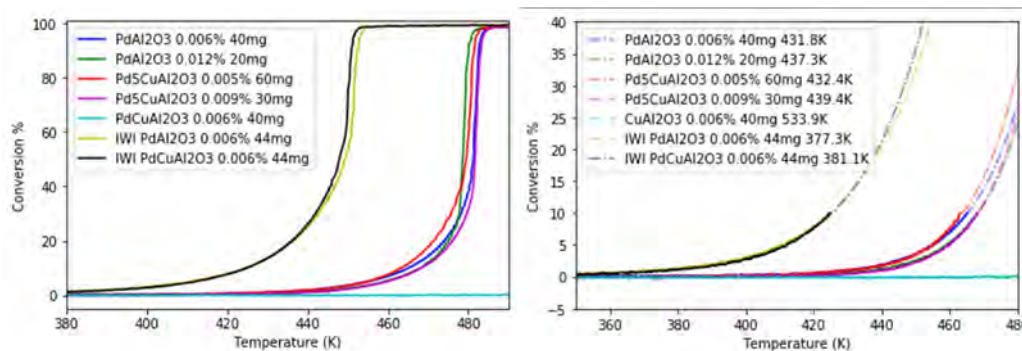


Figure 4.20: Initial samples' activity in the oxidation of carbon monoxide showing (left) the overall reaction progress and (right) the fitting process to determine the light off temperature. The offset for each fit is listed in the legend. Cu/Al₂O₃ are found to be inactive over this range.

Figure 4.20 shows the initial samples' activity with mass normalised to 2.4 μgPd in the reactor. The light off temperatures are determined by exponential fitting to the initial 20% conversion. As the flow rate for these samples is so low, there is a fairly high percentage error $\sim 10\%$ in the flow rate. However, as shown in figure 2.9, the effect on the light off temperature is likely to be minimal. As before, the impregnated samples light off first, with little difference observed between them until $\sim 30\%$ conversion where PdCu/Al₂O₃ demonstrates somewhat higher activity. However, such effects are better investigated at higher flowrates, and as such this section will focus on the light off temperatures and comparison to previous samples. IWI samples at equivalent Pd loadings with equivalent Pd content in the reactor demonstrate similar behaviour but light off at lower temperatures at 377.3 and 381.1 K for Pd/Al₂O₃ and PdCu/Al₂O₃ respectively. The previous IWI Pd/Al₂O₃ sample demonstrated a light off temperature of 383.6 K, see figure 3.10 on page 63. Note that the PdCu sample lights off first in the case of

the IWI samples. Due to a lack of clusters observed in STEM, these samples would require a different analysis method. Of the CCS samples, the lower loaded samples light off first, with Pd/Al₂O₃ lighting off slightly earlier than PdCu/Al₂O₃. While these results appear to be consistent across samples, no significant differences are observed at these flow rates, implying that the reaction initialises on a palladium surface, affected little by the addition of copper. All CCS samples light off before previous MACS samples with MACS Pd/Al₂O₃ (PdCu/Al₂O₃) lighting off at 490 K.

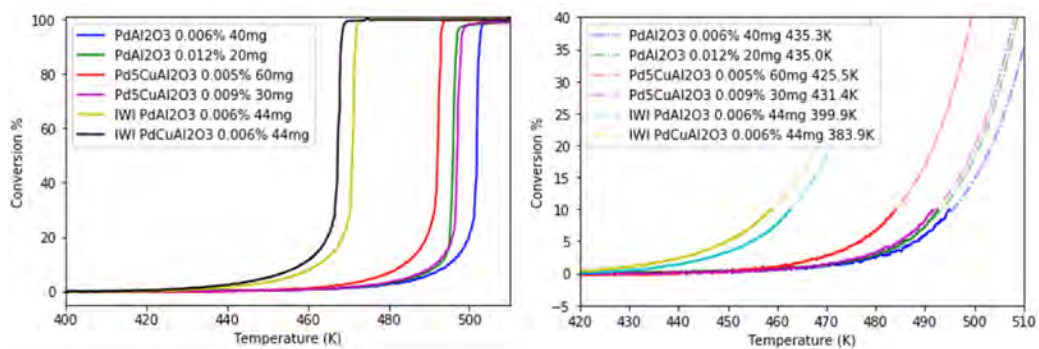


Figure 4.21: Initial samples' activity in the oxidation of carbon monoxide at 200ml/min reactive gas, showing (left) the overall reaction progress and (right) the fitting process to determine the light off temperature. The offset for each fit is listed in the legend.

At the higher flowrate of 200mlmin^{-1} more separation is observed between the samples, and with now negligible errors in flow rate, sample comparison can be more accurate. As before, the earliest samples to light off are the impregnated samples with the PdCu/Al₂O₃ sample active ~ 10 K before its Pd/Al₂O₃ equivalent, continuing through full conversion. From the CCS samples' results we see that regardless of loading, Pd/Al₂O₃ samples light off at 435 K with the higher loading sample demonstrating a faster turn on,

achieving full conversion 4.6 K earlier. The lower loaded CCS PdCu/Al₂O₃ initialises at 425.5 K and achieves full conversion 4.9 K before the higher loaded PdCu/Al₂O₃. This is likely due to the Cu reducing the interaction energy between the Pd and CO[127] allowing the reaction to progress at lower temperatures. The effect is amplified in the case of the lower loaded PdCu/Al₂O₃ sample due to its higher copper ratio. Finally it is worth noting that the higher loading (and thus lower surface area in the reactor) samples appear to be mass transport limited at high conversion, likely due to their lower active surface area in the reactor. This effect could also be due to a reactive gas not interacting with the shallower beds at high temperatures.

From these tests it can be concluded that samples of similar loading to the MACS samples have been formed and demonstrate activity for CO oxidation. These samples demonstrate far higher activity and lower light off temperatures than MACS samples formed previously, as they achieve 100% conversion at 200mlmin^{-1} (2mlmin^{-1}) CO. PdCu samples demonstrate a reduced light off temperature, and this appears to be primarily due to the copper content of these samples. The higher loaded Pd/Al₂O₃ demonstrates a similar activity to the higher loaded PdCu/Al₂O₃ at high conversions. This indicates that the addition of copper is being offset by the effect of larger clusters in the Pd/Al₂O₃ sample at high conversions. These initial tests provide an insight into work that could be done with the CCS, but were out of the scope of this project.

4.7.2 1-Pentyne Hydrogenation

As before, samples were tested for the selective hydrogenation of 1-pentyne to 1-pentene to gain some understanding of the selectivity of the catalysts produced by the CCS. The samples in this section will be the same as those tested for carbon monoxide oxidation in the previous section, see figure 4.18 for STEM analysis. The hydrogenation was performed as before in a tube furnace reactor, with the catalyst placed on a quartz wool bung with reactant gas flowed through the bed. This gas was 40% H_2 in He at 250mlmin^{-1} mixed with 1M 1-Pentyne + 1M 2-MethylPentane (as an internal standard for the gas chromatograph) in an n-Hexane solvent at 0.06mlmin^{-1} . The gas chromatograph used was a CP-3800 with a CP-WAX-52CB $25\text{m} \times 0.32\text{mm} \times 1.2\mu\text{m}$ column, followed by a CP-SIL-5CB $50\text{m} \times 0.32\text{mm} \times 5.0\mu\text{m}$ column. The integrated area of each peak observed from the gas chromatograph (GC), normalised by the area of the internal standard peak was used as the total quantity of product. Integration limits for the gases were set as follows; (Min:sec); 1-Pentene: 6:42-7:05, Pentane: 7:05 - 7:23, t-2-Pentene: 7:23-7:39, c-2-Pentene: 7:39 - 7:52, 1-Pentyne: 7:52-8:10, 2-MethylPentane: 8:44 - 9:05, n-Hexane: 9:05 - 11:22.

Samples were run at varying weights to achieve isoconversion at $\sim 125^\circ\text{C}$. The accuracy of this point is somewhat limited by the time taken to process an injection into the GC. As such measurements can only be taken every 12min, and we extrapolate linearly between them.

It is important to note that the reactions shown in figure 4.22 all have a significant dependence of selectivity on conversion as the reactions are

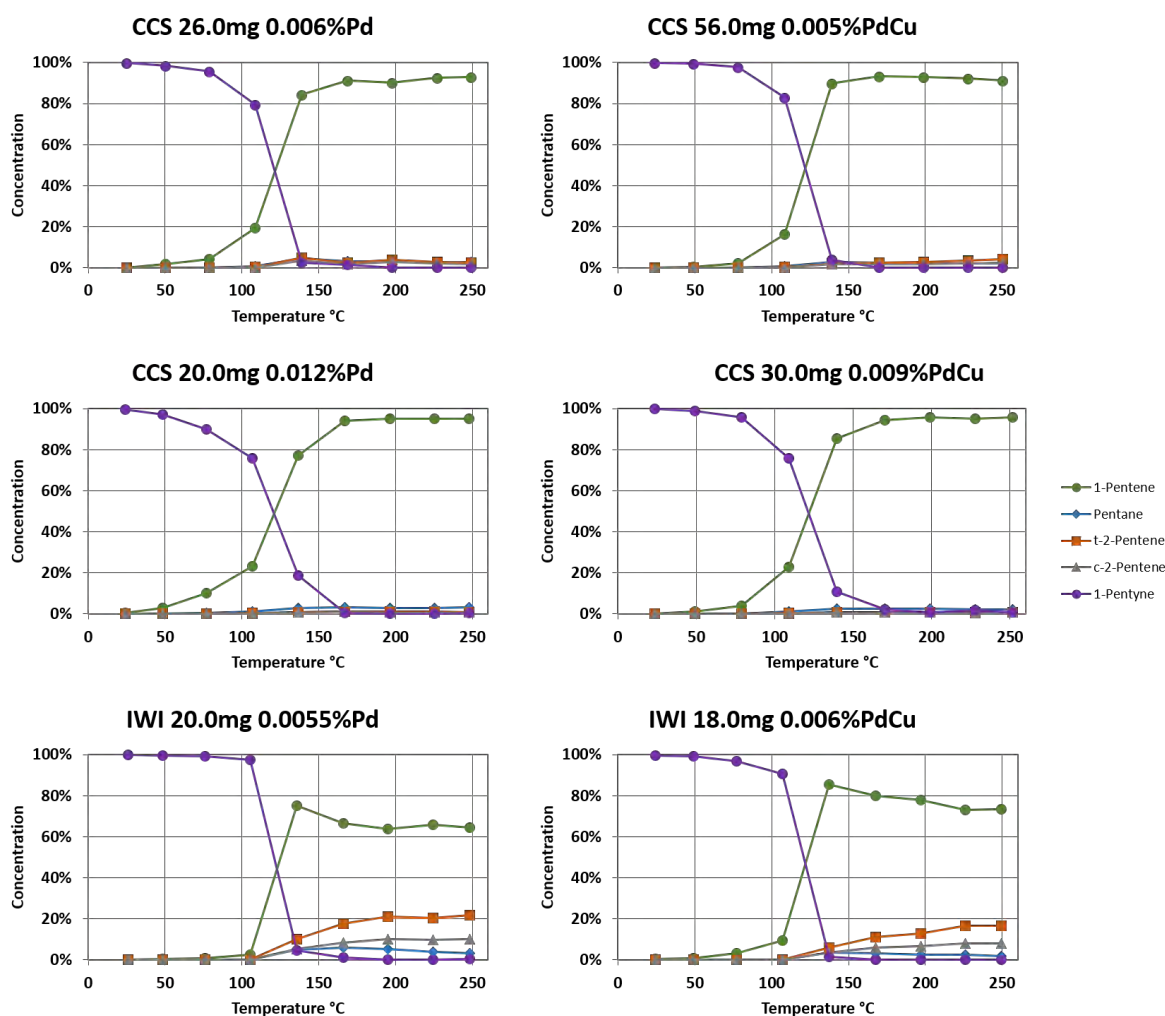


Figure 4.22: Initial samples' isoconversion for the partial hydrogenation of 1-pentyne to 1-pentene, with products of further hydrogenation being the migration of the double bond, producing cis and trans isomers of 2-pentene, and finally full hydrogenation to pentane.

linearly dependent; 1-pentene must be produced before other products. The isoconversion series shown aims to normalise the number of active sites in the reactor, however this is only truly valid in the case of a single type of active site with a single associated binding energy.

As can be seen from figure 4.22 for the CCS samples, the addition of Cu results in a decrease in active area proportional to the Cu atomic ratio. This implies once again that the sample is alloyed, and that the copper is an inactive spectator. This trend however is not observed in the case of Pd vs PdCu impregnated catalysts which demonstrate almost identical activity when normalised by metal loading. Impregnated samples demonstrate somewhat higher activity than CCS samples when normalised by metallic content. Similar differences have been observed previously [47] and attributed to residual Cl^- from chlorine containing precursors. Here a nitric acid precursor is used, which should not leave significant contamination, however may remain from the formation of the nitrate. This activity could also be attributed to a size effect as described by Boiteaux [128] who attributed larger clusters to higher activity in the hydrogenation of non-terminal alkynes. The addition of Cu leads to marginally increased selectivity to the production of the alkene, 78% to 86%. A marginal decrease in selectivity is observed upon addition of Cu to Pd/Al₂O₃ catalysts, from ~96% to ~93%. Selectivities quoted are maximums above 50% conversion. Impregnated samples demonstrate decreasing selectivity as a function of temperature, while CCS samples remain consistent at all observed temperatures where high conversion is observed. It is important to note that these effects mean that the selectivity observed here is less dependent on the quantity of catalyst as well, with CCS samples demonstrating consistent ~ 90% selectivity under all conditions tested. Due to the number of variables involved in these reactions, further investigation would require in depth chemical analysis of the catalysts' surface, though these results are similar to those reported in the literature for encapsulated

Ni/Al₂O₃ catalysts [129], PdAgAl₂O₃ catalysts[127], and other PdCu/Al₂O₃ catalysts [130]. While these results appear to be among the most selective and active, there is a certain bias as to what is published. In terms of selectivity for the alkene among selective hydrogenation reactions, all vacuum synthesised catalysts demonstrate exemplary behaviour. This is highlighted by [8]; the cluster beam, and now, more generically the ‘vacuum synthesis’ route appear to produce selective catalysts with relatively little refinement.

4.8 Conclusion

This chapter has focused on the design, development and build of a system that is designed to produce catalytic material on the few gram scale. Initial tests were carried out using available materials to gain an understanding of the necessary parameters for the build. It was determined that the surface temperature, deposition rate and sputter energy had no effect on cluster size when the quantity of metal deposited is normalised. Cluster size was also found to be broadly similar on amorphous carbon and α -alumina. This is thought to be due to the defect modulated growth mechanism, though other supports would have required further testing if they were to be used. As a result of these investigations, the only significant factor for cluster size control was shown to be deposition quantity per unit area. This dictates a highly consistent deposition method, coating each particle fairly evenly. However cluster size was shown to scale with the cube root of deposition quantity, implying three dimensional cluster formation and a somewhat dulled dependence on cluster size. Test binary clusters were produced demonstrating the

alloy formation of gold/silver nanoparticles at small sizes, independent of deposition order. As such, a piezo fluidised, hopper to hopper deposition tray was designed in order to tip powder from one covered area to another under the metal beam, exposing all particles for a similar length of time. A triangular prism shaped sputter target clamp was developed in tandem with the tray to allow sputtering of large area films and multiple metals consecutively. Films are clamped to this target and sputtered with a 600V ion source, capable of up to 10mA sputter current. Three metal films can be clamped, and each sputtered sequentially without breaking vacuum. The system was built and initial samples created using copper to tune the sputtering parameters measured before to the powder fluidisation in the completed system. Binary samples were also produced and their homogeneity analysed using STEM EDX. Co-sputtering targets of different geometries was compared to sequential sputtering and samples produced by incipient wetness impregnation. While metallic ratios are more homogeneous in certain co-sputtering target geometries, the flexibility of sequential deposition was considered to outweigh this for the applications here. Initial samples were then produced using palladium and copper. In the main this was done to verify the results in chapter 3 to see whether the copper contamination had had a significant effect. These samples were imaged with STEM and size distributions acquired producing mean cluster sizes of 1nm with similar \sim 1nm distribution widths. Samples were produced at two separate loadings of \sim 0.005 and \sim 0.010% Pd and PdCu on Al₂O₃, for a total of four CCS samples. These were compared to impregnated Pd/Al₂O₃ and PdCu/Al₂O₃ samples produced at 0.006% loading. All samples were tested for their activity in the oxidation of carbon

monoxide and the selective hydrogenation of 1-pentyne to 1-pentene with normalised Pd quantity in the reactor. In the oxidation of carbon monoxide, at low (10mlmin^{-1}) flow rates, samples demonstrate 50 K lower light off temperatures when compared to previous MACS samples. This is likely due to the differing interfaces between support and cluster demonstrated by atomic vs cluster deposition. IWI samples demonstrate significantly lower light off temperatures than both MACS and CCS samples, but remain very similar to those analogous samples produced for chapter 3 with a light off temperature of ~ 380 K. At higher flow rates, separation between samples becomes more apparent, however light off temperatures appear to be more dependent on composition than loading. Addition of copper decreases the light off temperature across all samples by ~ 10 K, with the lower loaded PdCu/ Al_2O_3 lighting off 5 K before other CCS samples. In summary, CCS samples are somewhat improved over cluster beam samples, and some minor tuning can be performed with the addition of copper. It can also be said that the previous samples did not have their activity for CO oxidation seriously affected by copper contamination. Impregnated samples remain significantly more active than physically deposited samples, possibly due to the cluster/support interface as discussed previously, or remaining contamination from the solvent. Considering that we would expect contamination from the solvent to decrease the activity of the catalyst and that the addition of Cu has no significant effect on the largely support independent, it seems reasonable that the more electronegative Cu may be closing the support cluster interface somewhat, thus lowering the light off temperature. In the selective hydrogenation of 1-pentene, an isoconversion series was performed

in an effort to normalise the active area in the reactor. Significantly, when this is done impregnated samples show the largest change over previous reactions. They are no longer active at low temperatures, producing a maximum selectivity of 75% at 130°C decreasing to 64% at 250°C achieving a final 99.5% conversion. Addition of copper improves selectivity and ensures complete conversion. IWI PdCu/Al₂O₃ achieves a maximum selectivity of 87% decreasing to 73% on complete conversion. CCS samples demonstrate a far higher selectivity and with very little temperature dependence. Conversion begins at 130°C and selectivity remains high as the temperature is ramped. Little difference is observed between CCS Pd/Al₂O₃ and PdCu/Al₂O₃ samples, besides a proportionate decrease in the active area, requiring a far larger quantity of catalyst for isoconversion. Higher loading samples demonstrate higher selectivities of 96% and 95%, with lower specific reaction rates.

In brief, the Clean Catalyst Source produces samples catalytically similar to those produced previously with the MACS system. They demonstrate reduced sizes and distribution widths with similar and improved catalytic behaviour. It must also be noted that due to its lack of complexity, the CCS is far easier to use, more reliable and requires ~ 1% of the time required to produce analogous samples to those in chapter 3. It also appears that for these reactions at least, there is a negligible difference between MACS samples and atomic agglomeration. As a result, we propose that if lab scale, solvent free catalyst production is desired, this is the superior method.

Chapter 5

Molybdenum Palladium Alloys

There are many possible ways to influence the surface of a catalyst support pre-deposition. The natural solution to modifying the formation of clusters on a support is to sputter the support, increasing the defect density. However the standard alumina supports used in this work appear to be defect rich, with very few areas where clusters are unable to nucleate. There is also the consideration of sputtering a powdered, insulating support. This would require a neutralised ion beam to prevent powder charging issues, and thus would require a similar set up to the powder tray in the CCS. As such, this method was not considered further. However, a coating of another material is likely to affect cluster formation in similar yet opposite ways. Due to the setup of the Clean Catalyst Source, metals are the natural choice here. An inactive metal was desired ideally with a high affinity for oxygen, resulting in a layer by layer growth mode. As such, molybdenum was chosen as a target metal in order to isolate interface effects. By taking advantage of the film growth properties of this metal, we aim to highlight the strengths of a direct

deposition sputter system for catalyst production, as well as demonstrating the use of materials that are challenging to use chemically.

Molybdenum's high affinity for oxygen leads to a Stranski-Krastanov (layer+island) growth mode on oxide supports [131, 132] as opposed to the Volmer Weber growth more commonly observed in catalytically active metals [89]. This gives access to an efficient way to control the surface properties of the support without significantly affecting its rheology. There are four areas of interest within the standard, cluster based catalytic systems observed here. The metal/support interface (contact surface), the metal/support boundary (cluster perimeter), the metal surface and finally the support surface. In an effort to investigate these effects, this chapter focuses on four *Pd* based samples: *Pd* clusters, *Mo* nucleated *Pd* clusters, *Mo* surrounded *Pd* clusters and *Pd* clusters formed on a *Mo* monolayer. All samples are formed using Al_2O_3 as a support. A cartoon of these structures is shown in figure 5.1.

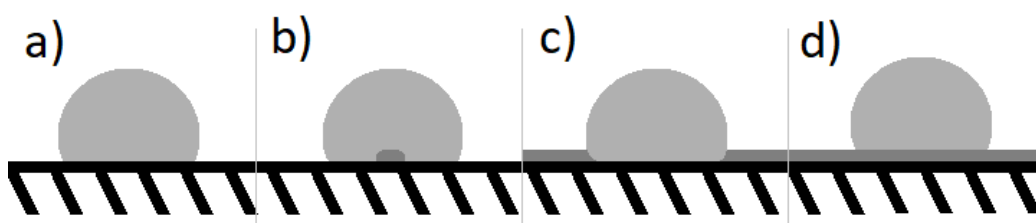


Figure 5.1: A cartoon showing the types of samples produced in this chapter showing a) $\text{Pd}/\text{Al}_2\text{O}_3$ control, b) *Mo* nucleated *Pd* clusters, c) *Mo* surrounded *Pd* clusters and d) *Mo* supported *Pd* clusters. All samples are produced on Al_2O_3 support particles. Key: light grey: *Pd*, dark grey: *Mo*.

5.1 Sample Production

All samples were produced using the CCS and due to the nature of this testing, impregnated analogues are not appropriate. In order to extract more fundamental formation information; the behaviour of Mo on our Al_2O_3 support, as well as its interaction with Pd, sample analogues were produced on TEM grids. This allows comparison of the formation mechanics on the highly defected carbon film, as well as Al_2O_3 particles without concern for the natural variation in material deposited across the particles' surfaces. This also removes confusion from clusters formed on the opposite side of the Al_2O_3 particles. Observations on the carbon film enable background-free structural analysis. All samples had molybdenum deposited first and were imaged to confirm their structure prior to palladium deposition.

5.1.1 TEM Grid Depositions

Al_2O_3 decorated TEM grid samples were deposited on for 1 minute at 0.4, 1.0 and 4.0mA sputter current producing ~ 0.3 , 0.8 and >1 mono-layers of Pd respectively. All TEM grid samples were then deposited with Pd for one minute at 1.4mA sputter current. Mo coverage was measured from STEM images.

From figure 5.2 we see that at 0.3ML coverage, sub nanometer ~ 10 atom islands are observed with some isolated atoms. At 0.8ML coverage, island density is increased with some apparent bi-layer structure formation. At <1 ML coverage, the structure of the layer belies its formation: from cluster like seeds. The thickness of the film at the edge of the Al_2O_3 particle may be

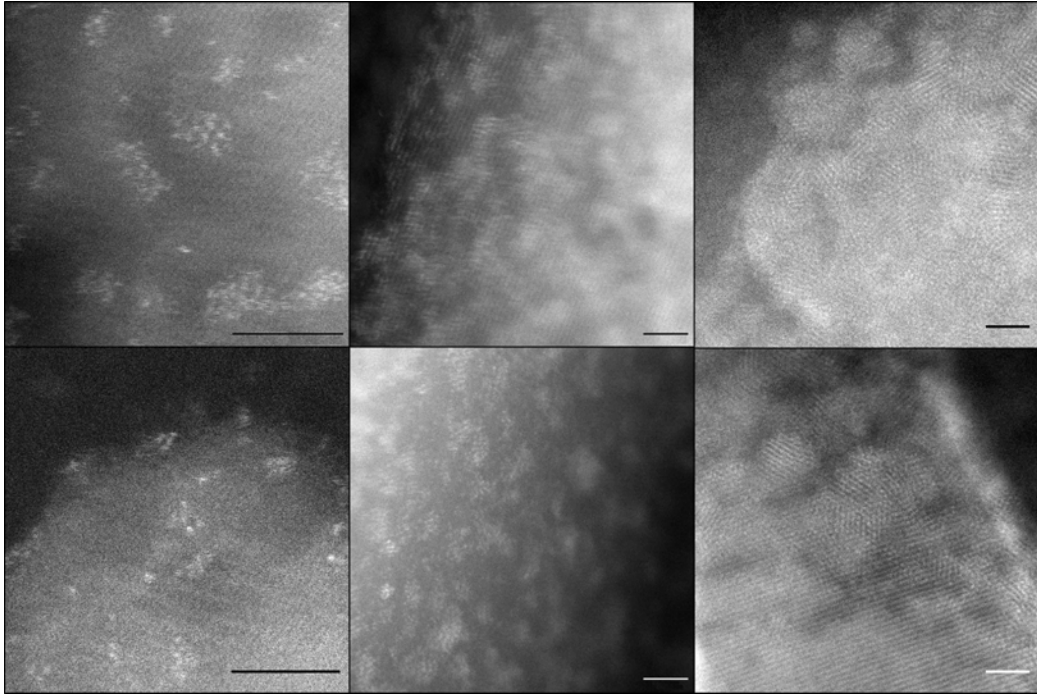


Figure 5.2: Images of Mo Deposited on Al₂O₃ particles mounted on TEM grids at different coverages; showing left to right; 0.3, 0.8 and <1ML. Scale bars are 2nm throughout

measured, but is not representative due to the deposition geometry. From these images it is possible to see the development of molybdenum structures as a function of deposited material, with isolated Mo islands becoming a semi-connected network and finally a full Mo film, with individual domains observed.

From the observations in figure 5.3, we see that at 0.3ML coverage, Pd clusters appear to form over the pre-deposited Mo islands, indicated by a lack of material observed between clusters. At 0.8ML coverage, an unbroken Mo layer is observed separating the formed Pd clusters, indicating that they form in between the network of islands on the bare surface. At <1ML Mo,

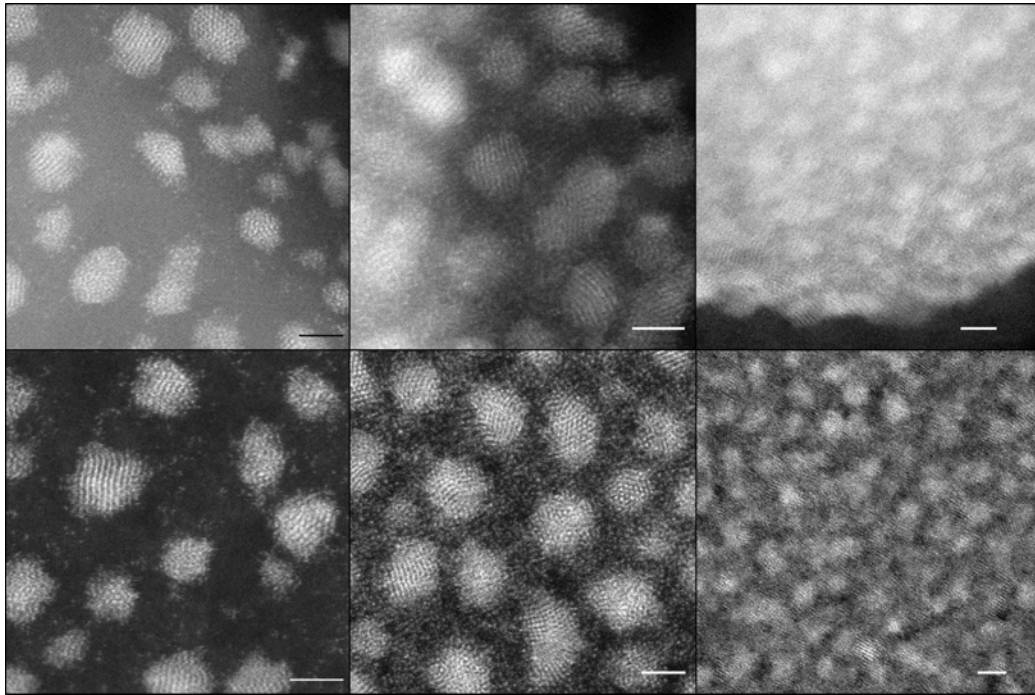


Figure 5.3: Images of the same samples as seen in figure 5.2 after a one minute, 1.4mA Pd deposition. Left to right; 0.3, 0.8 and <1ML Pd. Top images are of the structures on Al_2O_3 , while the lower images are taken on the carbon film for clarity. Scale bars are 2nm throughout

Pd forms cluster like structures on top of the likely oxidised Mo layer, though the thick underlayer makes these harder to distinguish

It is possible to conclude that we have produced three distinct MoPd structures on Al_2O_3 ; Mo supported Pd clusters, Mo surrounded Pd clusters with contact to the Al_2O_3 support, and Pd clusters formed on a Mo shell. At this point, we should take some time to consider the effects of oxidation. As the samples were exposed to air in between metal depositions, the Mo surface will be oxidised. Based on a base chamber pressure of $2 \times 10^{-7} \text{ mBar}$, we would expect a complete surface encounter every ~ 10 seconds, primarily composed of H_2O . It is therefore reasonable to expect that surface (hydr)oxide forms

during deposition, as well as partial oxidation due to the Al_2O_3 support. As such no particular effort was made to investigate the effects of deposition without exposing the sample to air. A colour change was observed upon deposition of higher loadings of Mo on powdered Al_2O_3 which faded over ~ 24 hours, indicating the presence of metallic Mo being oxidised in the samples. As the surface of this Mo is likely to also be similarly oxidised, this is not considered to affect the formation of Pd particles.

Once these structures have been shown to form on well controlled, broadly planar surfaces, these compositional samples were repeated on powdered Al_2O_3 to gauge their catalytic or macroscopic response.

5.1.2 Glass Ground Supports

Initial samples for this work were produced as in chapter 4, on the standard saint-gobain alumina powder used consistently through this work. While initial tests were consistent, surface dependent techniques, such as carbon monoxide chemisorption and hydrogen based temperature programmed desorption were desired. In order to produce the required surface area for such samples support was ground between two glass panes to a BET surface area of $9.0\text{m}^2\text{g}^{-1}$ from an original value of $1.5\text{m}^2\text{g}^{-1}$. This allows for deposition of an increased quantity of material without affecting the surface structure, and thus signal from such samples may be acquired.

5.1.3 Catalyst Formation

Samples were coated with Mo for 0, 3.6, 15 and 21 minutes at a sputter current of $8mA$. These samples were then imaged and coated with Pd for 6:15min with a sputter current of $8mA$. These deposition parameters are derived from the standard formation of Pd on Al_2O_3 used in section 4.6, and scaled by the increase in BET surface area caused by the glass grinding of Al_2O_3 . This is an attempt to reproduce the structures seen in figures 5.2 and 5.3 on a large scale, producing a lab scale catalyst. Test samples revealed the simple scaling of deposition quantity to be effective in reproducing the previous surface structures.

Palladium on Alumina Control Sample

When deposited for 6:15 min this control sample came out with significantly lower loading $\sim 270ppm$ as opposed to $\sim 570ppm$ from the other samples. This discrepancy is attributed to poor agitation. Due to time constraints with ICP-MS testing, this sample, referred to as PdMo0 was replaced with a previous Pd/ Al_2O_3 sample deposited for 10:00min. It is that sample that is illustrated in this section.

Figure 5.4 demonstrates similar structure to of the control sample as desired, with some overdeposition due to the higher loading. These structures are very similar to those seen in chapter 4 as desired.

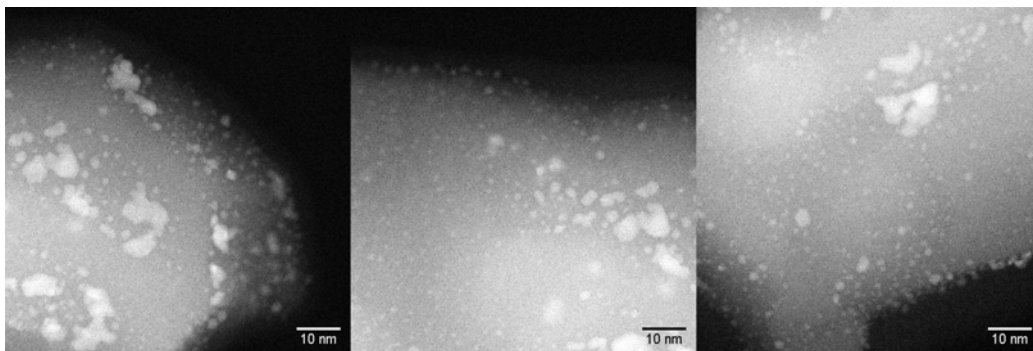


Figure 5.4: Example images of the control Pd/Al₂O₃ sample demonstrating structures as seen throughout this work, with some areas somewhat overdeposited

Molybdenum Nucleated Palladium

This sample, referred to as PdMo1 for convenience was formed by a 3:36 min deposition of Mo at a sputter current of $8mA$, followed by a 6:15 min deposition of Pd, also at a sputter current of $8mA$.

From figure 5.5, initial monolayer Mo Islands are formed at the alumina's nucleation points and are subsequently coated by Pd. Very little evidence is seen of residual Mo after the palladium deposition, leading us to believe, as in the case of the TEM grid samples, that the Pd clusters have formed at the same nucleation sites as found by the Mo. As no jagged Mo edges appear to be exposed, it is concluded that some alloying has occurred upon deposition of Pd. This could be due to the Pd clusters picking up the surface Mo or causing it to diffuse on the surface forming more circular islands in a form of 2D Brownian motion stimulated by mobile Pd atoms. The final result is a sample almost indistinguishable from those Pd/Al₂O₃ samples produced previously. This sample aims to isolate electronic and structural

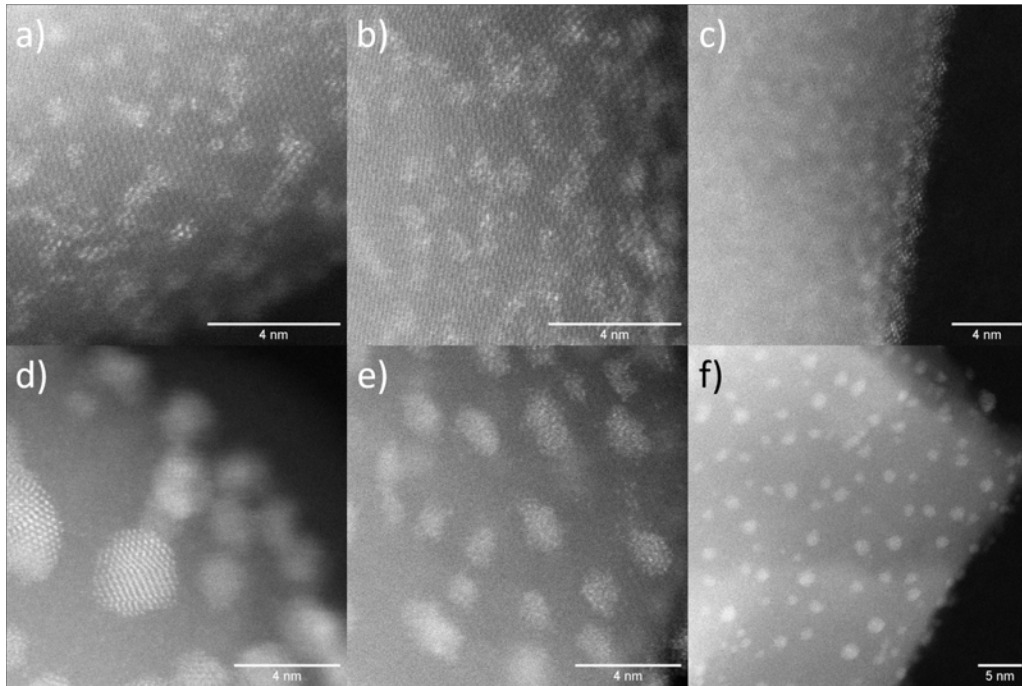


Figure 5.5: Produced structures of Mo and Pd/Mo on glass ground alumina powder. a) - c) show molybdenum structures before palladium deposition, d) - f) show the final sample complete with palladium clusters

strain effects. All imaged areas demonstrate qualitative homogeneity.

Molybdenum Surrounded Palladium

This sample, referred to as PdMo₂ was formed by a 15min deposition of Mo followed by a 6:15 min Pd deposition, both at 8mA sputter current.

Figure 5.6 shows the formation of a holey Mo monolayer followed by the formation of a Pd cluster structure after Pd deposition. As on the TEM grids, the Pd cluster structure appears to be present on top of a heightened background, and clusters appear to be misshapen when compared with previous, broadly spherical particles. This is taken as evidence that the clusters

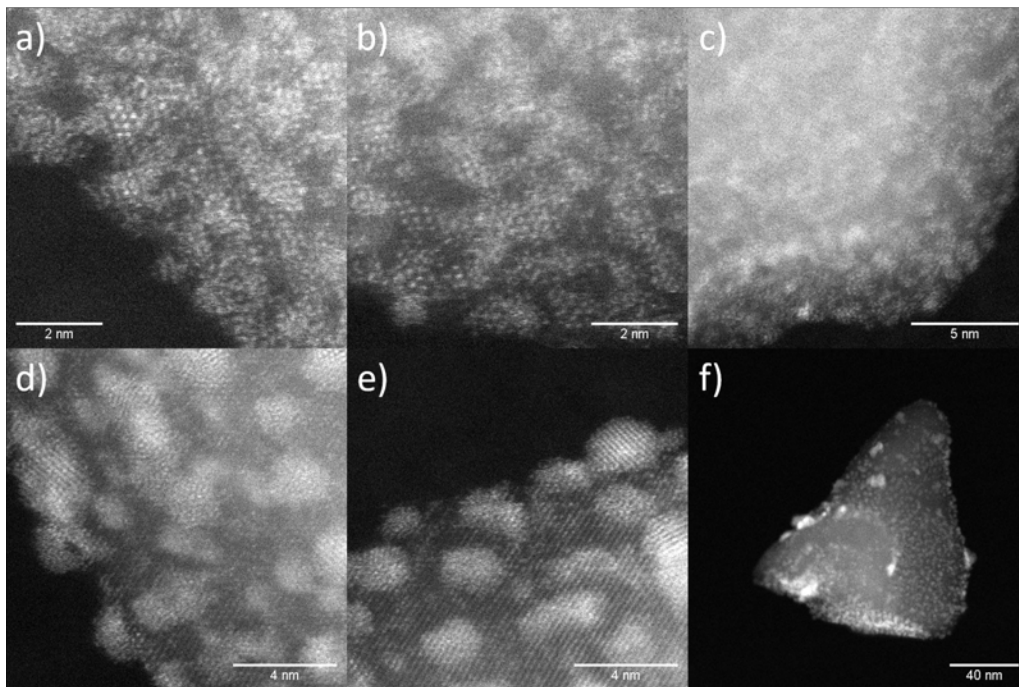


Figure 5.6: Produced structures of Mo and Pd/Mo on glass ground alumina powder. a) - c) show holey monolayer molybdenum structures before palladium deposition, d) - f) show the final sample complete with palladium clusters

are forming on the Al_2O_3 support, in the holes of the Mo monolayer. A few large structures are observed as shown in figure 5.6 f), though the vast majority of the surface area is as shown in d) and e). This sample should isolate cluster/support interface effects, allowing the formation mechanism of the Pd clusters to remain largely unaffected.

Palladium on Molybdenum

This sample: PdMo3 was produced by a 20min deposition of Mo followed by a 6:15min deposition of Pd at 8mA in an attempt to produce a Mo monolayer decorated with Pd clusters.

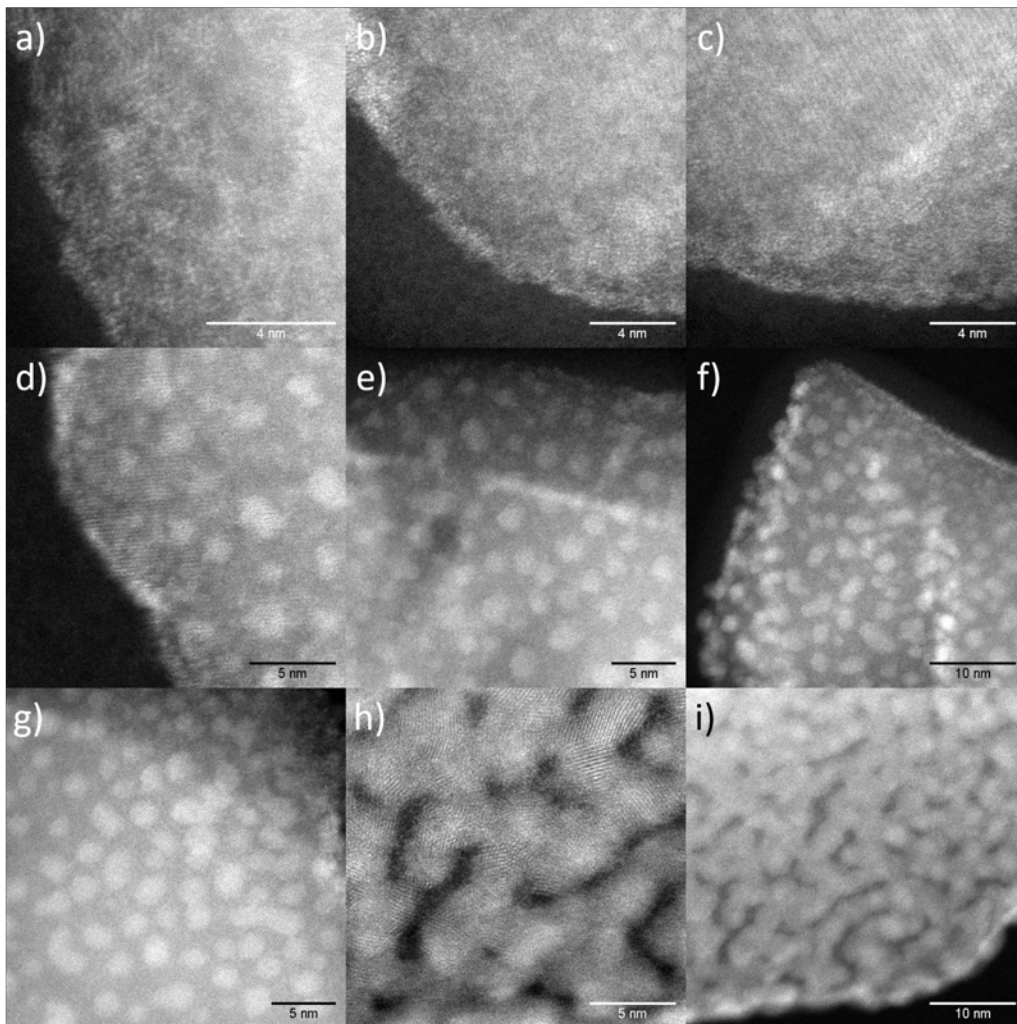


Figure 5.7: Produced structures of Mo and Pd/Mo on glass ground alumina powder. a) - c) show ~monolayer molybdenum structures before palladium deposition, d) - i) show the final sample complete with palladium deposition, demonstrating the range of structures observed

Figure 5.7 on page 131 shows the Mo monolayer structure and a range of Pd cluster structures observed across the sample. Clusters in this sample appear to be larger than in previous samples in this section, as well as being far more varied in size. Certain areas show clusters as seen previously,

though a far wider variation in apparant material deposited is observed in this sample than any others. This may simply be due to poor agitation, but looking at the edges of the powder particles particularly obvious in figure 5.7 f) and i) reveals a flattened mono/bilayer nature of the clusters that may not have been seen previously. Growing flattened structures highlights the variation in deposited material observed previously in section 4.6, as the size of these flattened structures will scale with the square root of the quantity of deposited material, rather than the cube. This eventually leads to the interconnected sample structure seen in figure 5.7 h) and i). In short, the molybdenum monolayer has affected the formation mechanism of the palladium sample.

5.1.4 Sample Summary

While the above sections illustrate the produced structures, this section summarises the quantitative details of the produced samples.

Sample	Loading(ppm)	Mean \varnothing (nm)	FWHM(nm)
PdMo0	830Pd <1Mo	1.65 ± 0.03	0.79 ± 0.04
PdMo1	480Pd 60Mo	1.38 ± 0.04	0.95 ± 0.05
PdMo2	570Pd 420Mo	1.58 ± 0.08	1.05 ± 0.09
PdMo3	570Pd 580Mo	1.83 ± 0.09	0.93 ± 0.10

Table 5.1: Summary of the quantitative analysis from STEM analysis and ICP-MS for quantitative data showing loadings of each metal in PPM, average diameters and distribution widths. Errors are calculated as before by error on the fit and numerical error

As discussed in the section before, the addition of Mo appears to increase the diameter of all clusters slightly, with average cluster diameters of

$PdMo1 < PdMo2 < PdMo3$. The larger size of PdMo0 is attributed to the higher loading. Samples demonstrate similar loadings for the purposes of catalytic testing.

5.2 Surface Area Testing

Throughout this work, homogeneity is measured solely using the STEM. While the samples imaged are highly consistent across the measured area, confirmation of this at the lab scale is important, it is possible that the method of attaching particles to the grid is selective for coated particles. This is done due to an apparent disconnect between the observed surface area in STEM and the sample's catalytic behaviour when compared with impregnated samples, discounting the ion exchanged surfaces as shown in figure 3.9. Testing in this manner is interesting for samples when viewed from a surface science angle, as these techniques can be used in UHV environments on very small surface areas with very accurate pressure measurement[133, 134, 135]. As such these tests could be compared to see the changes of moving to the macroscale, but this is out of the range and equipment available for this project. In this section, the results of Hydrogen Temperature Programmed Desorption (H_2 TPD) and Carbon Monoxide Chemisorption of the PdMo samples covered in this chapter are presented.

5.2.1 Temperature Programmed Desorption of Hydrogen

The temperature programmed desorption of hydrogen was performed using a MicroMetrics AutoChem II. Samples were heated under argon at 250°C for 10 minutes, dosed with hydrogen at room temperature for one hour before TPD up to 800°C at $10^{\circ}\text{Cmin}^{-1}$. Samples are compared to 1% and 0.1% Pd/Al₂O₃ impregnated samples for scale. Initial results demonstrate small peaks of desorption for all samples around 680°C . Most literature [2, 136] shows the desorption peak of hydrogen on palladium occurring at $\sim 100^{\circ}\text{C}$, with some desorption below room temperature. On supported catalysts, the desorption peak appears at $\sim 500^{\circ}\text{C}$ [137], which appears to be due to subsurface H₂ ad(ab)sorption [138, 139] with peaks attributed at 500°C and $> 600^{\circ}\text{C}$.

From figure 5.8 we see that all samples demonstrate a response around 680°C . The higher loaded impregnated samples demonstrate the largest desorption peaks due to this loading. The 1% IWI Pd/Al₂O₃ peak is shifted somewhat to lower temperatures, likely due to its more crystalline nature. Some variation is observed in the peaks produced across the MoPd sample set, however they are confounded by apparent detector drift. All samples demonstrate this negative drift at higher temperatures which is attributed to instrumental error. Thermal effects are compensated by a secondary gas cooling loop, and back pressure effects should not be present in an empty tube blank. As these effects are consistent and variable a background reduction is performed using a blank run, the y locations of the peaks normalised and

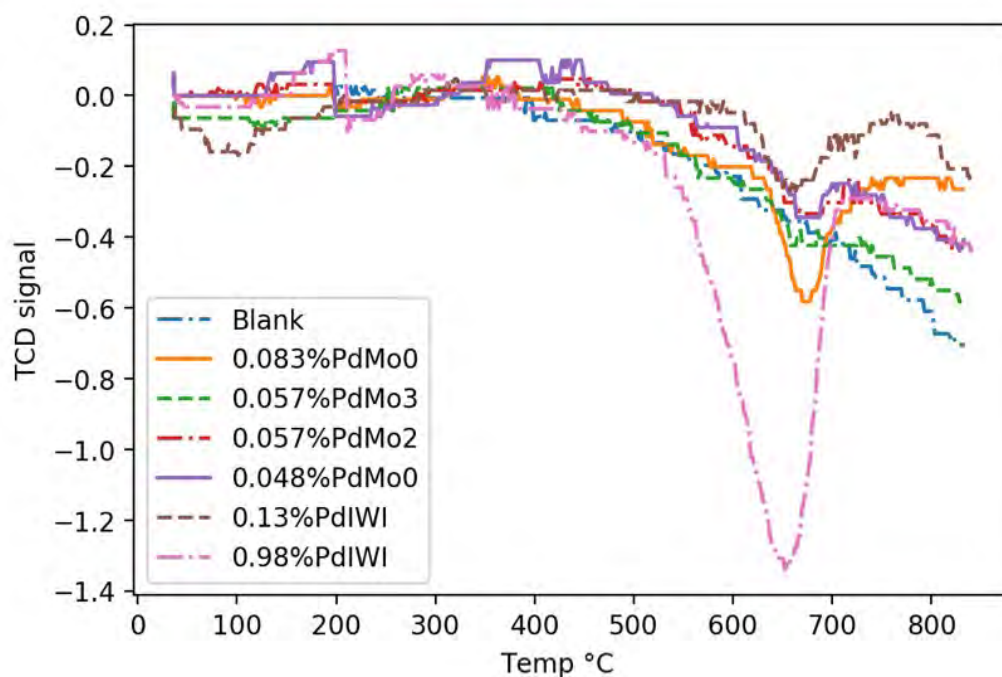


Figure 5.8: Temperature programmed Desorption data from all samples along with an empty tube blank run, and impregnated Pd/Al₂O₃ samples.

the peak value inversely scaled by metal loading.

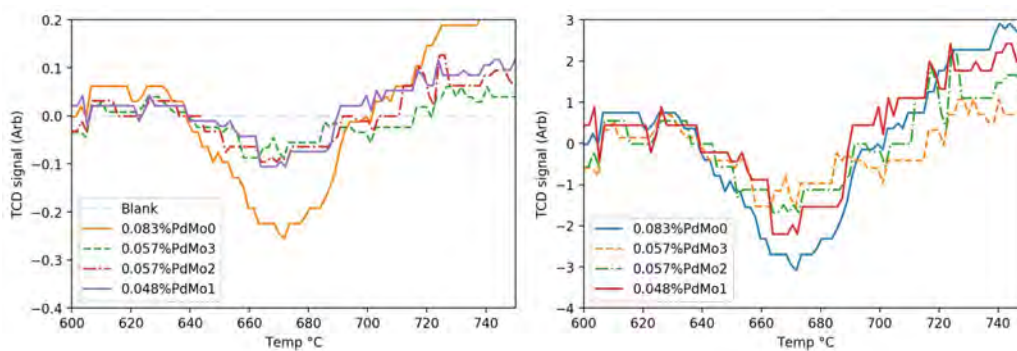


Figure 5.9: Temperature programmed Desorption data from all MoPd samples corrected for tilt, height and loading. Showing tilt correction and height normalisation (left) and loading normalisation (right). Impregnated samples are omitted for clarity

As can be seen from figure 5.9 (left) it is possible to see that there is a trend of peak amplitude with molybdenum content, with an increase in Mo resulting in a decrease in the quantity of H_2 adsorbed. Pd/Al₂O₃ (PdMo0) adsorbs the most H_2 when normalised by loading. This could be due to size differences in the samples though these have been shown to be minor (figures 5.4 and 5.5). As such it is suggested that the subsurface Mo reduces the H_2 adsorption capacity. It is possible that the alloy PdMo interface of The PdMo1 sample has decreased the quantity of subsurface hydrogen absorbed. The Mo surrounded Pd sample may show a further decrease due to the lesser surface area of unoxidised Pd available, with the Pd on Mo sample demonstrating the smallest desorption peak by combination of these factors and the apparent lack of multi-layer structures observed (figure 5.7.

5.2.2 Chemisorption of Carbon Monoxide

Carbon monoxide Chemisorption offers a more direct measurement of the active surface area of a catalyst sample due to the relative ease of calibration. The use of carbon monoxide as an adsorbate naturally may highlight different active areas to hydrogen. Samples were heated to 200°C under 10% hydrogen in a nitrogen environment to reduce the catalysts. Chemisorption is performed at 35°C with metered introduction of carbon monoxide from 10 to 600 mBar.

As can be seen from figure 5.10, all samples display similar behaviour, with the PdMo0 (Pd/Al₂O₃) sample demonstrating the lowest active surface area. All samples demonstrate similar first adsorptions indicating similar

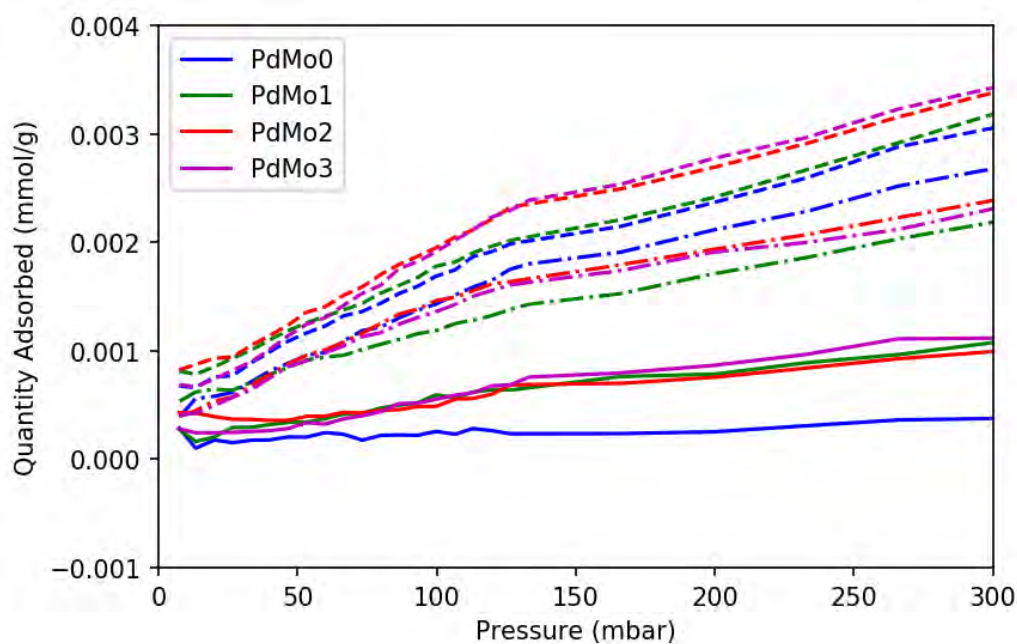


Figure 5.10: Carbon monoxide chemisorption isotherms of PdMo/Al₂O₃ samples. Dashed line show the initial adsorption, dot-dashed lines show the repeat measurement, and solid lines show the difference between adsorption repeats. See figure 2.20 on page 47 for the repeat isotherm method

un-reactive surface areas as is to be expected, with the exposed Mo samples adsorbing slightly more CO, also as expected. This separation is not seen in the repeat (reversible only) adsorption, indicating chemisorption on the Mo surface. All PdMo/Al₂O₃ samples demonstrate very similar active areas, as such, these are calculated by taking the monolayer adsorption quantity (at ~ 130 mBar), and approximating a 1:1 CO:Mo adsorption ratio. These values are shown in table 5.2.

These samples are produced on Al₂O₃ powder with a specific surface area of $\sim 10\text{m}^2\text{g}^{-1}$. From the coverage shown in STEM images (figures 5.4 to 5.7), a value of $\sim 5\text{m}^2\text{g}^{-1}$ would be expected, however the values measured

Sample	Area (m^2g^{-1}) sample		Pd loading	Area (m^2g^{-1}) Pd	Crystallite Size (nm)	Area (m^2g^{-1}) PdMo	PdMo Crystallite Size (nm)
PdMo0	0.022	\pm 0.001	0.083%	26.51	9.51	26.51	9.51
PdMo1	0.069	\pm 0.003	0.048%	143.75	1.75	127.78	2.00
PdMo2	0.064	\pm 0.003	0.057%	112.28	2.25	64.65	4.14
PdMo3	0.069	\pm 0.003	0.057%	121.05	2.08	60.00	4.51

Table 5.2: Table showing each sample's area per gram of sample, per gram of palladium and per gram of deposited metal as measured by CO chemisorption. Taking metal loading into consideration, average hemispherical cluster size, considering Pd as well as both Pd and Mo as chemisorption sites (i.e: contributing to the cluster).

by chemisorption are ~ 100 x lower. This issue is unresolved, but due to the consistency of STEM images and the dramatic change upon introduction of molybdenum, it is suggested that chemisorption is not occurring as expected on these samples, and perhaps larger agglomerated structures are responsible for this behaviour. Cluster sizes as calculated are unlikely to be representative of the real sample due to the Mo structures present, but are included as this is a standard method of obtaining crystallite size which highlights differences between the methods.

5.3 Catalyst Damage

In an effort to determine whether the results shown in table 5.2 are reasonable as well as to characterise their sintering, the samples were imaged after chemisorption analysis. The damage observed in this section is likely to be primarily due to the reduction step performed before the chemisorption analysis. This also has the advantage of being more controlled than an an

exo/endermic reaction, as the sample temperature will remain consistent and independent of reaction rate.

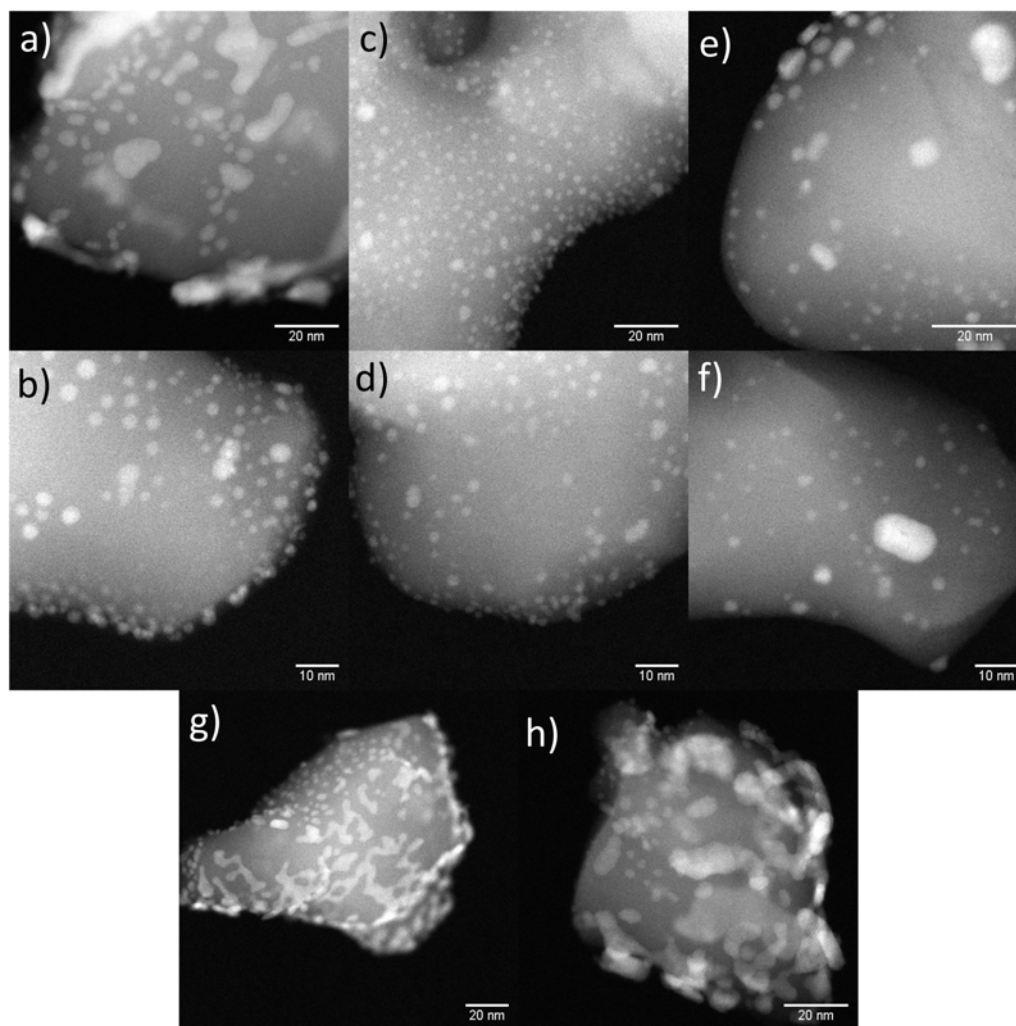


Figure 5.11: Representative STEM images of palladium molybdenum samples after CO Chemisorption testing showing a) and b) PdMo0, c) and d) PdMo1, e) and f) PdMo2, g) and h) PdMo3

From figure 5.11, it is possible to see different modes of agglomeration across each sample, despite very small changes in molybdenum content, indicating that this results from the structures as discussed in section 5.1.3.

PdMo0 shows sintering as expected, with large, presumably lower defect regions being cleared of metal. This metal gathers up at edge sites, this may be due to Ostwald (cluster-atom) or Smoluchowski (cluster-cluster) ripening. PdMo1 appears to demonstrate similar levels of agglomeration of small clusters, though with reduced clearing and large structure formation. PdMo2 also demonstrates reduced clearing and distinct Ostwald ripening characteristics, particularly in 5.11 f). Many small clusters remain, with large clusters growing with a large apparent collection area. PdMo3 demonstrates large island like formations which appear to be of uniform thickness. Some small areas remain cluster like, though the majority appear to be agglomerated. Some cleared areas are observed though these are comparatively small, likely due to the island like metallic structures occupying a larger space than their cluster based counterparts. From these samples it appears that the molybdenum deposition has had a significant effect on the ripening modes of the catalysts. As such it is necessary to demonstrate the structure of molybdenum in the sample after damage has occurred. Figure 5.12 shows higher resolution STEM images of the Mo underlayer.

Figure 5.12 demonstrates that a small amount of molybdenum remains on the surface in the form of small clusters around larger palladium or PdMo agglomerates. When compared to figures 5.6 and 5.7 on pages 130 and 131, a significant amount of molybdenum appears to have been removed from the surface likely by the formation of volatile oxides [140]. Despite this, the entirety of the surface appears to remain doped with low levels of molybdenum. This effect is somewhat more noticeable in PdMo3 with the molybdenum layer appearing more like an interconnected network in places, though this

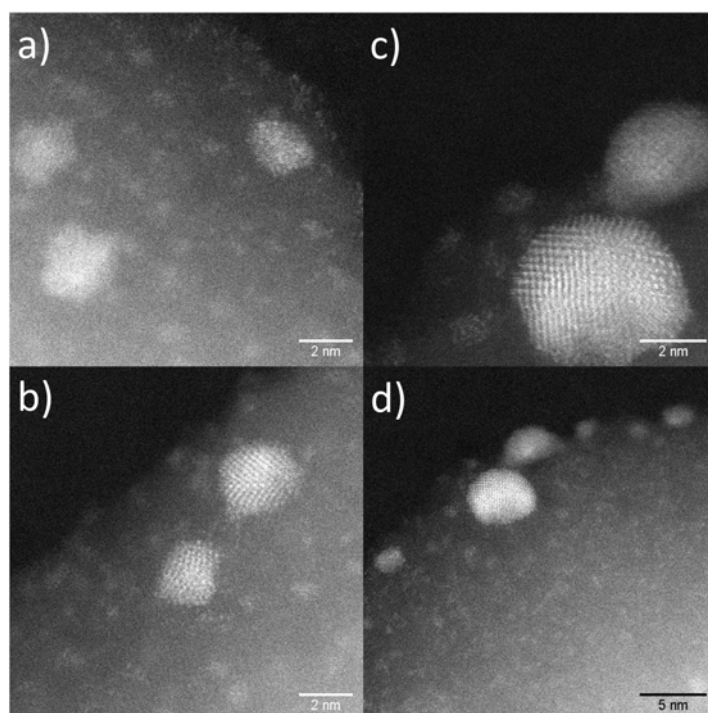


Figure 5.12: STEM images showing examples of residual molybdenum structures after carbon monoxide chemisorption, showing a) and b) PdMo₂, c) and d) PdMo₃. No evidence of Mo structures was observed in PdMo₁ after chemisorption testing

is not a significant difference. No remaining molybdenum was observed on PdMo₁, presumably remaining covered by palladium. In order to quantify catalyst damage, size distributions were plotted for each sample after damage has occurred and are shown in figure 5.13.

From figure 5.13 it is possible to see that all samples have increased in average cluster size and distribution width as is to be expected. All samples demonstrate a small peak at very small sizes, and generally show a smooth distribution profile; indicators of Ostwald ripening. However PdMo₀ and PdMo₃ demonstrate a rougher profile and some features at 4-7 nm that

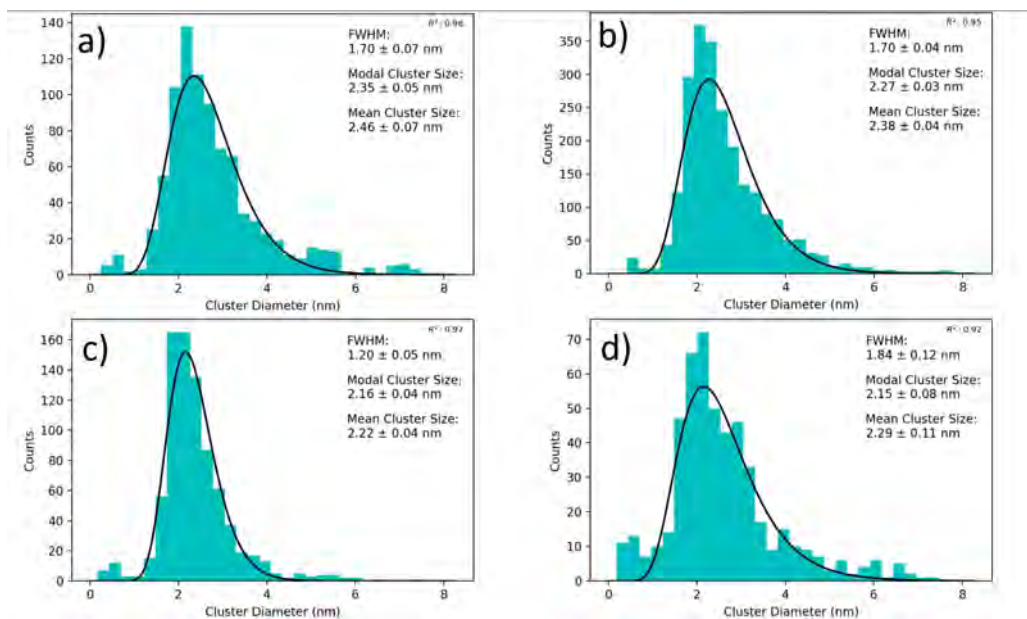


Figure 5.13: Size distributions based on Canny analysis of STEM images of PdMo/Al₂O₃ samples after CO chemisorption showing a) PdMo0, b) PdMo1, c)PdMo2, d)PdMo3

indicate some Smoluchowski ripening has also occurred. It appears that clusters are immobilised more effectively when deposited on or surrounded by molybdenum structures. These results are compared with the original samples as shown in table 5.1 and summarised in table 5.3.

Sample	Mean ϕ (nm)	Δ Mean(nm)	FWHM(nm)	Δ FWHM(nm)
PdMo0	1.65 ± 0.03	0.81 ± 0.03	0.79 ± 0.03	0.91 ± 0.06
PdMo1	1.38 ± 0.04	1.00 ± 0.03	0.95 ± 0.03	0.75 ± 0.04
PdMo2	1.58 ± 0.08	0.64 ± 0.05	1.05 ± 0.03	0.15 ± 0.01
PdMo3	1.83 ± 0.09	0.46 ± 0.07	0.93 ± 0.33	0.91 ± 0.11

Table 5.3: Summary of the catalyst damage caused by carbon monoxide chemisorption showing mean cluster size and distribution width before chemisorption and their changes as a result of the process. Errors are calculated by error on the fit as well as numerical error and propagated by fractional addition in quadrature.

From table 5.3, we can see that the largest change in diameter is observed in PdMo1, however referring to figure 5.13 we see that all samples end up with similar average cluster sizes, indicating that the relatively lower change in size observed in PdMo0 may be due to its larger initial size. This indicates that a stable cluster size may be reached under the reduction conditions the samples were exposed to. This could also be due to PdMo1 requiring two reduction cycles, though final mean cluster sizes do indicate a point of stability has been reached. In general the addition of molybdenum appears to inhibit agglomeration if there is a sub-monolayer quantity of Mo. Of significant note is the change in distribution width with PdMo1 and PdMo2 demonstrating a more homogeneous damage mechanism as expected by the anchoring of palladium clusters at the Mo/Al₂O₃ interface. Of the two methods, surrounding the clusters appears to be far more effective than anchoring them. This is understandable, as the dominant ripening mechanism appears to be Ostwald which is likely to be largely unaffected by a central anchoring point. The central molybdenum anchoring point may also increase the strain of palladium particles, decreasing their stability, thus accelerating their ripening, though there is not enough evidence from these results to comment on whether or not this is occurring. Also of consideration is the mobility of atomic species over the surface of the support. Higher mobility will lead to increased damage, and this could be seen as causing the difference between PdMo0 and PdMo3. While these samples demonstrate similar final cluster sizes, and increases in distribution width, the layer like structures observed in PdMo3 appear to indicate a strong binding between the support and mobile atoms. PdMo3 also demonstrates the lowest agglomeration though this result is somewhat

discounted, due to the structures observed in figure 5.11 which are not suited to this analysis.

5.4 Catalysis

As with previous samples, the PdMo/Al₂O₃ samples were tested for their activity in the oxidation of carbon monoxide and the selective hydrogenation of 1-pentyne to 1-pentene. In order to keep results as consistent as possible with previous results, Pd quantity remains normalised at 2.4 μ g in the reactor across all samples. Mo/Al₂O₃ samples were found to be inactive for both reactions and as such Mo was not considered in this normalisation. As these samples are significantly higher loading than those in chapters 3 and 4, this requires \sim 5mg of catalyst in the reactor, which results in a sub 1mm bed depth. In turn, this produces poor catalytic behaviour for both reactions in terms of maximal conversion, presumably due to small channels forming within the catalyst bed and a proportion of gas failing to interact with the catalyst. As such samples for 1-pentyne hydrogenation were diluted to 60mg in the reactor with blank support ensuring similar bed characteristics to previous work. Due to time constraints on the vapour phase catalysis rig, this was not possible for carbon monoxide oxidation.

5.4.1 Carbon Monoxide Oxidation

The oxidation of carbon monoxide was performed as before in a tube furnace, vapour phase reactor, with the catalyst bed supported on quartz wool. The temperature is read \sim before the gas passes through the catalyst bed. See

section 4.7.1 on page 110 for further details. Gas flow rate was fixed at 200mlmin^{-1} .

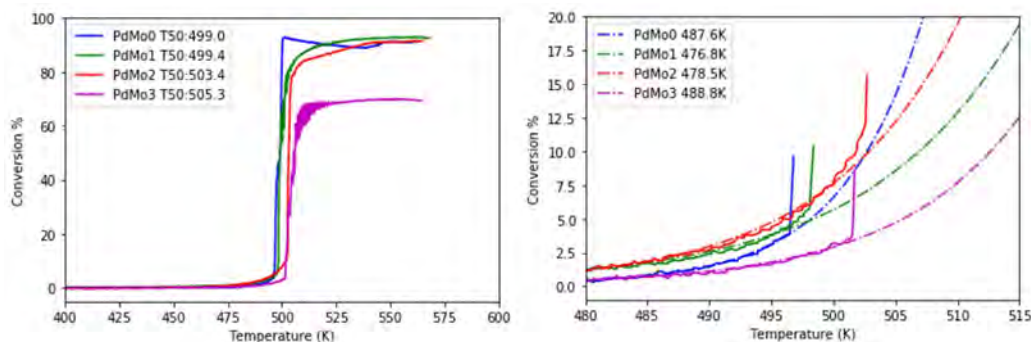


Figure 5.14: The progression of carbon monoxide oxidation over PdMo/ Al_2O_3 catalysts at 200mlmin^{-1} 1% CO as a function of temperature. Showing (left) The overall reaction progression showing temperatures at 50% conversion in the legend and (right) the point of light off with data cut after each reaction goes critical. Fits show pre-critical reaction progress with fit offsets listed in the legend.

Figure 5.14 shows the samples' activity for the oxidation of carbon monoxide. As mentioned in the introduction to this section, all samples demonstrate shallow bed characteristics with oscillations in the conversion and no samples reaching full conversion. This is the case, despite steep light off gradients and normalised Pd quantity in the reactor, as such the shallow bed conclusion appears to be reasonable. This could be partially corrected by re-scaling of the data, but this does not affect our conclusions and as such is omitted. As the concentration of molybdenum increases, so does the temperature required for 50% conversion (T50). This is attributed to the area of exposed palladium being reduced marginally at higher molybdenum loadings, considering that the surface has likely undergone similar sintering and alloying to that seen in figure 5.11. When considering how each sample

lights off the grouping appears to be structural. PdMo0 and PdMo3 initiate approximately 10K after PdMo1 and PdMo2. The significant difference between these pairs of samples is the formation, with PdMo1 and PdMo2 comprising clusters formed on the Mo/Al₂O₃ boundary. As such this is tentatively attributed to the lower offset temperatures of these samples, possibly due to the strain of a mixed material boundary. However this is in direct contradiction to the previous conclusion, which relies on the agglomeration of palladium and molybdenum and destruction of these well defined structures. As such, no significant conclusion can be reached in the way each sample lights off other than the addition of molybdenum appears to have a very small effect on the catalytic behaviour of these samples for the oxidation of carbon monoxide.

5.4.2 1-Pentyne Hydrogenation

As before, samples were tested for their activity and selectivity in the selective hydrogenation of 1-pentyne hydrogenation. Due to the intrinsic link between activity and selectivity in these reactions, samples were diluted to 60mg using the same ground Al₂O₃ used for the initial deposition. The effect on the catalyst is shown in figure 5.15

As can be seen in figure 5.15 dilution allows the reaction to approach completion, and becomes comparable with previous results.

As shown in figure 5.16, samples again demonstrate decreasing activity as the quantity of molybdenum is increased, with the exception of PdMo1 which demonstrates a ~1% increase in conversion over PdMo0. With the

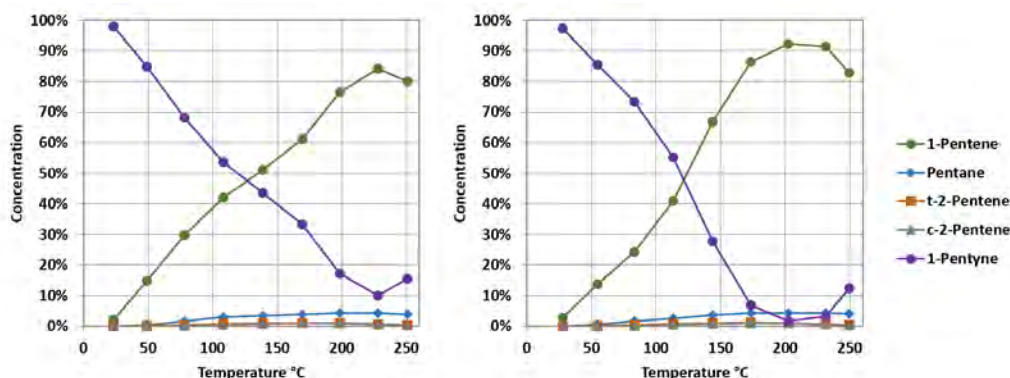


Figure 5.15: The effect of catalyst bed dilution using blank Al_2O_3 . Showing PdMo0 ($\text{Pd}/\text{Al}_2\text{O}_3$) without dilution (left) and with dilution (right)

exception of PdMo1, these results directly match those of the hydrogen TPD shown in figure 5.9 in terms of hydrogen quantity adsorbed. In contrast to previous samples, all secondary products are fully hydrogenated pentane rather than cis or trans 2-pentene as observed in chapters 3 and 4, attributed to the increased density of deposited material, allowing for multiple local hydrogenation reactions. All samples demonstrate 94% selectivity to the production of 1-pentene.

5.5 Summary and Conclusion

The samples in this chapter have focused on production of structures at a large scale. Molybdenum Palladium binary catalysts were produced by deposition of 0.3, 0.8 and >1 monolayers of molybdenum, taking advantage of its layer plus island growth mode to influence the structures formed on the surface. The results of these PdMo binary formation parameters are palladium nucleated on molybdenum (PdMo1), molybdenum surrounded

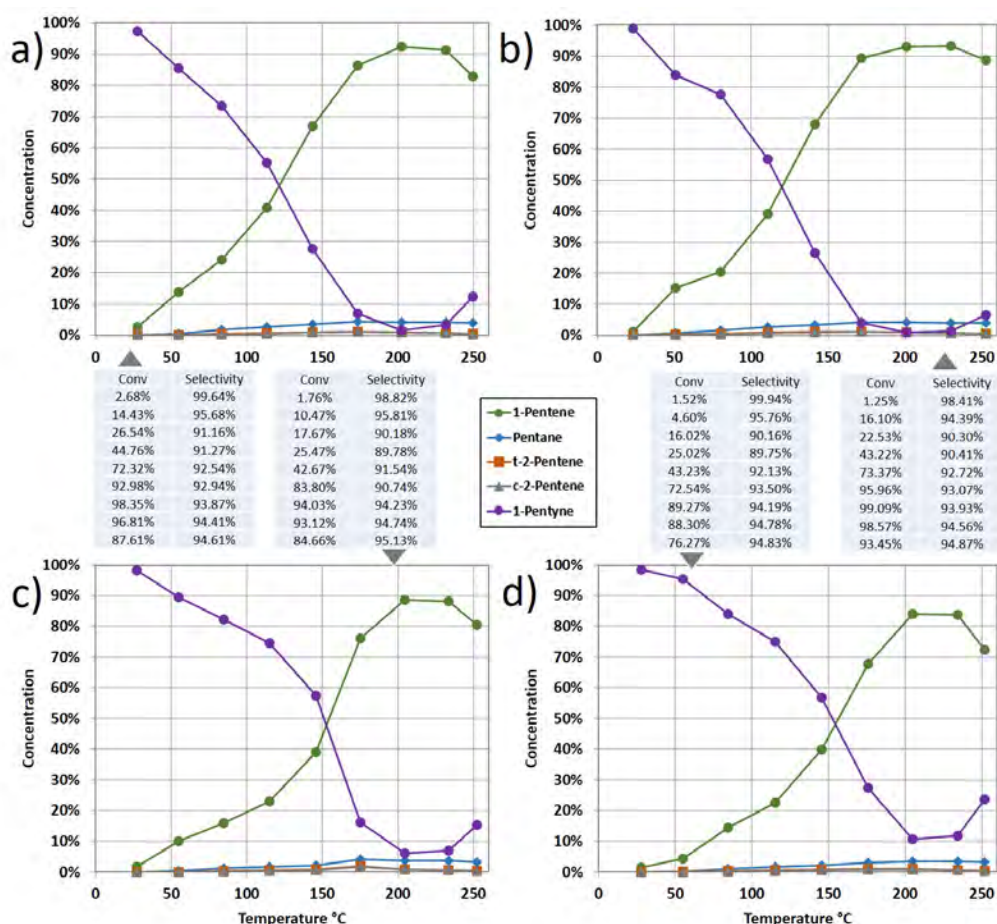


Figure 5.16: The results of 1-pentyne hydrogenation of MoPd samples showing samples with $2.4\mu\text{g}$ Pd in the reactor. All samples are diluted to 60mg with blank Al_2O_3 . Graphs show concentrations of reactant and products as a function of temperature in the reactor. Showing a) MoPd0, b) MoPd1, c) MoPd2, d) MoPd3. Selectivity tables apply to graphs as indicated

palladium nanoparticles (PdMo_2) and palladium nanoparticles formed on a molybdenum layer (PdMo_3). These are then compares to a $\text{Pd}/\text{Al}_2\text{O}_3$ control sample (PdMo_0). Surfaces appear to be consistent and as expected throughout the samples according to STEM images: figures 5.4 to 5.7, with a small increase in cluster size observed as Mo content increases. In order

to achieve significant signals from surface measurement methods, these samples were produced on glass ground $\alpha\text{Al}_2\text{O}_3$ with a surface area of $10\text{m}^2\text{g}^{-1}$ and an associated increase in metal was deposited. The homogeneity of the samples was also measured using macroscopic surface methods: the temperature programmed desorption of hydrogen, and the chemisorption of carbon monoxide, very low signals are observed. For H₂ TPD these signals are close to the instrument resolution, but are present and indicate a reduction in hydrogen adsorption as a function of molybdenum content. This shows that the Molybdenum should not be active for hydrogenation within the $30 - 750^\circ\text{C}$ temperature window measured as expected, and the Mo content appears to inhibit the adsorption either by altering the structure of the palladium nanoparticles or by physical obstruction, possibly assisted by sintering and PdMo alloy formation. Due to the high desorption temperatures of $\sim 680^\circ\text{C}$ the hydrogen peak is attributed to subsurface hydrogen absorption when compared with existing literature. Carbon monoxide chemisorption demonstrates similarly small results, indicating an area of $\sim 0.06\text{m}^2\text{g}^{-1}$ as opposed to the $\sim 5\text{m}^2\text{g}^{-1}$ that might be expected from STEM images. This remains unresolved, but due to the consistency of STEM images throughout the entirety of the project, this is attributed to unexpected behaviour from small palladium particles prepared in this way. When the surface area of each sample is normalised by metal content, PdMo0 demonstrates approximately 1/5 of the other samples, and thus apparently larger particles. As such, damage to the samples was analysed after CO chemisorption by repeat STEM imaging. In contrast to the chemisorption results, all samples appeared to have very similar damaged size distributions with the notable exception of

PdMo₂ (molybdenum surrounded palladium nanoparticles) which demonstrates a narrow size distribution, attributed to the well defined defect sites formed in the molybdenum layer. Molybdenum surrounded and molybdenum nucleated clusters also show decreased evidence of Smoluchowski ripening likely due to their well defined anchoring/defect sites. Samples demonstrate familiar activity and selectivity in the oxidation of carbon monoxide and the selective hydrogenation of 1-pentyne to 1-pentene. No significant change in activity or selectivity is observed in conjunction with the increasing quantity of molybdenum and differing structure, other than a minor decrease in activity at higher quantities of Mo. In conclusion, we have shown that this technique is effective at making simple structures over large surface areas using materials that would be challenging chemically. We have also shown that it is possible to make samples somewhat more resistant to sintering without significantly affecting their catalytic behaviour in alkyne hydrogenation or carbon monoxide oxidation by forming active palladium clusters on a molybdenum modified support.

Chapter 6

Conclusions

This project has been focused on the application of surface science methodology to catalyst production. Due to the background of the researchers involved the project began as a scale up of the Matrix Assembly Cluster Source (MACS); a cluster source built around the sputtering of a synthetic rare gas/metal matrix formed on a cryogenic copper plate. This source was scaled up and used to produce a range of palladium and gold nanoparticles on aluminium oxide and silicon dioxide powders using an agitated cup to achieve an even coating on the powder particles. Produced samples demonstrate approximately 1.6nm diameter particles with distribution widths of approximately 1.8nm (offset due to log normal distribution). All samples' metallic structures appear similar independent of the support or metal used, though gold samples demonstrate noticeable cluster size bimodality, indicating cluster-cluster agglomeration. Samples were produced at $\sim 0.05\text{wt}\%$ metal, as further deposition would lead to significant agglomeration. Samples were tested for their catalytic activity and selectivity in the oxidation

of carbon monoxide, selective hydrogenation of 1-pentyne, and the reduction of 4-nitrophenol. Samples demonstrated similar catalytic activity to impregnated analogues when the quantity of active metal was normalised. MACS samples demonstrated lower activity in the oxidation of carbon monoxide, higher normalised activity in the reduction of 4-nitrophenol and higher selectivity (linked to a lower specific activity) in the selective hydrogenation of 1-pentyne. Aluminium oxide was found to be the favoured support for both oxidation and hydrogenation, with no clear preference for the reduction reaction. Gold samples were found to be inactive for hydrogenation. These samples serve as a proof of principle study, showing that the MACS can be used for catalyst production at the gram scale, and that produced catalysts demonstrate activity for a range of reactions as expected. MACS samples also appear to demonstrate exceptionally high selectivity in the hydrogenation of 1-pentyne to 1-pentene. During the course of this work, a sample was produced without the formation of a matrix, as such, this sample was simply formed by direct sputtering and surface agglomeration. It was found to demonstrate a similar cluster size distribution despite a noticeable change in surface structure and an identical catalytic response. Samples were later found to demonstrate ~20metal% copper content from the matrix support. This copper content was shown to cause no significant effect in future work, but naturally complicates the results, making the technique far less desirable for model catalyst investigations.

Due to necessity, the course of the project was altered at this point. Based on the results from the final matrixless sample, it was determined that direct sputtering would be an acceptable method for catalyst produc-

tion. As such, a new system was designed and built to sputter metal films onto piezo-fluidised powder particles. This system was named the Clean Catalyst Source (CCS). By tipping support particles between two covered hoppers, we ensure that each particle is exposed for a similar amount of time across multiple transits under the metal beam. Due to this process not requiring matrix formation, sputter currents and thus deposition rates can be significantly higher than the MACS system. This factor, as well as the removal of the cooling and matrix formation steps, makes the process much less time consuming, reducing formation times from $\sim 10\text{h/g}$ to $\sim 10\text{min/g}$ with scope for further reduction at higher throughput. This method was shown to produce well dispersed homogeneous metal nanoparticle structures across powder particles and was used to produce palladium and palladium/copper binary samples on aluminium oxide supports. These materials were chosen to be comparable to samples made using the MACS to gain an appreciation of the effect of copper addition to palladium samples. Gold samples were discontinued to focus primarily on selective hydrogenation, as this reaction gives the most sensitive response to catalyst changes, has produced promising results with MACS samples, and is arguably the most interesting, being (at time of writing) challenging to catalyse at high selectivity and throughput. Silica supports are also abandoned as these produced lower activity, but otherwise similar samples, and the focus for this work is on metal structures. CCS samples showed similar activity and selectivity to the production of 1-pentene from 1-pentyne as MACS samples as well as far higher activity for carbon monoxide oxidation despite similar light off temperatures. Palladium copper binary particles were shown to be marginally less selective than

their monometallic equivalents, but do not demonstrate any significant differences. As such, it is determined that the selective nature of these catalysts comes primarily from their in-vacuum synthesis, and partially due to their low loading. In terms of methodology, the direct sputtering of metal onto fluidised powder is presented a superior method to cluster deposition if the desired outcome is catalyst production. This is due to the problem of cluster/cluster agglomeration in cluster beam systems, as well as the increased complexity and hence reduced flux, that would make powder management systems such as the hopper to hopper system used in the CCS unfeasible due to the quantity of wasted metal. Direct deposition, however falls short of cluster deposition when considering the range of structures available for testing. Significant work has been invested in production of structured nanoclusters by gas aggregation with the potential for application in catalysis [141], however the quantity of such production is not conducive to lab scale catalysis, being limited to in-situ analysis[142]. Along side of certain cluster production systems capable of high fluxes [24] direct deposition appears to be promising for generic ‘catalyst production’ whether isolation of solvent effects is desired, or use of materials that may be challenging chemically. All direct deposition methods (i.e: deposition of neutral species) suffer from lower support interaction which the difference in selectivity is in general attributed to. The monolayer structures found in impregnated samples, attributed to ion exchange as seen in figure 3.9 on page 62 may also have an effect on selectivity. With this in mind, the project moved onto unique surfaces that it might be possible to engineer using direct deposition techniques. To achieve some control over surfaces at this scale, it is necessary to control the self

assembly of material layers. As such we choose molybdenum for its layer plus island growth mode, as well as the challenges associated with chemical production of molybdenum catalysts. As a highly reactive and high melting point metal, molybdenum also promises certain anchoring and damage resistant properties that other metals may be unable to provide.

As such, the final section of this project was to develop surfaces, albeit simple ones, as may be done in the world of surface science on a larger scale. These surfaces would then be tested for their catalytic activity and compared with those made previously. From initial tests performed on amorphous carbon electron microscopy grids, it was determined that it would be possible to manipulate the quantity and thus the structure of a pre-deposited molybdenum monolayer to form small seeds or nucleation points with a ~ 0.2 monolayer deposition, a holey ~ 0.8 monolayer film and a >1 monolayer film. When these structures are coated with a consistent quantity of palladium, clusters appear to form on molybdenum seeds, inside holes in the monolayer and on top of the monolayer respectively. These structures were reproduced reliably on powder particles with a total area of $\sim 30m^2$. When tested for hydrogen retention by hydrogen temperature programmed desorption, samples demonstrate small peaks at $\sim 650^\circ C$ are observed and attributed to subsurface adsorption. Peaks are in line with impregnated samples of similar loading. This behaviour does not appear to influence hydrogenation results, besides possibly limiting hydrogen availability within the catalysts' operating temperature. Calibrated carbon monoxide chemisorption was used to estimate the surface area of samples with all samples demonstrating a low $\sim 0.05m^2g^{-1}$. Due to the consistency and weight of STEM data this area is attributed to

the bonding characteristics of carbon monoxide with these samples, however these results remain in direct opposition. Alternative resolutions of these values could be that STEM data is not representative of the entire sample, or that samples are not effectively reduced under the 200°C under a 10% hydrogen environment. It was found that increasing the temperature of the reduction led to a decrease in measured surface area, attributed to a sintering effect, and confirmed with STEM. This results in the aforementioned conclusion, possibly due to re-oxidation of the metal by oxygen donation from the support. When samples are analysed after CO chemisorption, molybdenum is found to decrease sintering with a higher molybdenum content resulting in a smaller average increase in cluster size. Molybdenum surrounded palladium clusters demonstrate a significantly decreased change in distribution width, with molybdenum nucleated palladium clusters demonstrating a similar, though less pronounced broadening decrease.

Finally, all molybdenum/palladium samples demonstrate similar activity for the oxidation of carbon monoxide and the selective hydrogenation of 1-pentyne as previous samples. The addition of molybdenum results in a marginal decrease in activity, likely due to simple coverage restriction as samples sinter over the course of the reaction. The addition of molybdenum shows the potential of the use of a metal with a different growth mode to influence the structural formation of a sample, with a view to increase a catalyst's robustness without affecting its catalytic behaviour. This work also highlights how well dispersed powder deposition can give enough control to form surface structures over large surface areas for catalytic testing.

Both the MACS and CCS methods have been shown to produce simi-

lar structures and hence catalysts. These catalysts have been found to be comparable to analogous impregnated samples with some increased selectivity, and somewhat lower activity attributed to the chemical composition of the boundary between support and metal caused by the presence or absence of ion exchange. Well controlled direct deposition may also be suitable for reproduction of surface structures on a large scale to observe their effects, though control has been sacrificed for scale, as it often is. We submit that these methods deserve their place in catalyst production and may serve to bridge the gap somewhat between surface science and catalysis.

Outlook

As discussed through this work, there are two potential avenues for progression of these methods. It may be possible to scale up known surface structures from literature in order to observe and modify their behaviour for application in catalysis. For example, these techniques would be effective for the creation of polymer coated palladium nanoparticles for hydrogen storage [143] or whether a reasonable gold hydrogenation catalyst can be formed based on the observations in [144] possibly by stabilisation using molybdenum. Applications will naturally vary depending on specific areas of expertise, and while this may be a specialised technique it appears to be ideal for such applications, particularly those requiring small $\sim 1\text{nm}$ clusters. The alternative avenue for advancement with these techniques is as a catalyst production tool used in conjunction with more standard methods. Due to the lack of high temperature reduction and calcination, somewhat smaller clus-

ters are feasible for similarly low temperature reactions. This fact combined with the simplicity of a one-step process, the associated low turnaround time of samples, and a solvent free synthesis may earn physical deposition a larger place in the catalytic chemist's repertoire of techniques. The continuation of this work is therefore likely best undertaken by those with experience and access to catalytic testing and measurement equipment as deciphering the fundamental differences in catalysts produced by these methods may help refine their niche.

Bibliography

- [1] G. Ertl and H. J. Freund, “Catalysis and surface science,” *Physics Today*, vol. 52, no. 1, pp. 32–38, 1999.
- [2] N. Takehiro, P. Liu, A. Bergbreiter, J. K. Nørskov, and R. J. Behm, “Hydrogen adsorption on bimetallic PdAu(111) surface alloys: Minimum adsorption ensemble, ligand and ensemble effects, and ensemble confinement,” *Physical Chemistry Chemical Physics*, vol. 16, no. 43, pp. 23930–23943, 2014.
- [3] I. Cabria, M. J. López, S. Fraile, and J. A. Alonso, “Adsorption and dissociation of molecular hydrogen on palladium clusters supported on graphene,” *Journal of Physical Chemistry C*, vol. 116, no. 40, pp. 21179–21189, 2012.
- [4] L. Salvati, L. E. Makovsky, J. M. Stencel, F. R. Brown, and D. M. Hercules, “Surface spectroscopic study of tungsten-alumina catalysts using X-ray photoelectron, ion scattering, and Raman spectroscopies,” *Journal of Physical Chemistry*, vol. 85, no. 24, pp. 3700–3707, 1981.
- [5] Y. T. Tsu and Y. W. Chen, “Preparation of gold-containing binary metal clusters by co-deposition-precipitation method and for hydrogenation of chloronitrobenzene,” *AIMS Materials Science*, vol. 4, no. 3, pp. 738–754, 2017.
- [6] M. Haruta, “Size- and support-dependency in the catalysis of gold,” *Catalysis Today*, vol. 36, no. 1, pp. 153–166, 1997.
- [7] H. Wang, Y. Jia, W. Hu, H. Jiang, J. Zhang, and L. Zhang, “Effect of preparation conditions on the size and encapsulation properties of mPEG-PLGA nanoparticles simultaneously loaded with vincristine sulfate and curcumin,” *Pharmaceutical development and technology*, vol. 18, no. 3, pp. 694–700, 2013.

- [8] P. R. Ellis, C. M. Brown, P. T. Bishop, J. Yin, K. Cooke, W. D. Terry, J. Liu, F. Yin, and R. E. Palmer, "The cluster beam route to model catalysts and beyond," *Faraday Discussions*, vol. 188, no. January, pp. 39–56, 2016.
- [9] S. Pratontep, S. J. Carroll, C. Xirouchaki, M. Streun, and R. E. Palmer, "Size-selected cluster beam source based on radio frequency magnetron plasma sputtering and gas condensation," *Review of Scientific Instruments*, vol. 76, no. 4, 2005.
- [10] K.-j. Hu, *Structural variation of size-selected metal clusters in chemical reactions by*. PhD thesis, University of Birmingham (UK), 2015.
- [11] Y. Cao, Z. Sui, Y. Zhu, X. Zhou, and D. Chen, "Selective Hydrogenation of Acetylene over Pd-In/Al₂O₃ Catalyst: Promotional Effect of Indium and Composition-Dependent Performance," *ACS Catalysis*, vol. 7, no. 11, pp. 7835–7846, 2017.
- [12] P. R. Ellis, C. M. Brown, P. T. Bishop, D. Ievlev, J. Yin, K. Cooke, and R. E. Palmer, "High-selectivity palladium catalysts for the partial hydrogenation of alkynes by gas-phase cluster deposition onto oxide powders," *Catalysis, Structure and Reactivity*, vol. 4, no. 2, pp. 1–8, 2018.
- [13] I. Lee, F. Delbecq, R. Morales, M. A. Albiter, and F. Zaera, "Tuning selectivity in catalysis by controlling particle shape," *Nature Materials*, vol. 8, no. 2, pp. 132–138, 2009.
- [14] M. A. Watzky and R. G. Finke, "Transition metal nanocluster formation kinetic and mechanistic studies. A new mechanism when hydrogen is the reductant: Slow, continuous nucleation and fast autocatalytic surface growth," *Journal of the American Chemical Society*, vol. 119, no. 43, pp. 10382–10400, 1997.
- [15] K. N. Houk and P. H. Y. Cheong, "Computational prediction of small-molecule catalysts," *Nature*, vol. 455, no. 7211, pp. 309–313, 2008.
- [16] L. D. Marks and L. Peng, "Nanoparticle shape, thermodynamics and kinetics," *Journal of Physics Condensed Matter*, vol. 28, no. 5, p. 053001, 2016.
- [17] L. Pavan, K. Rossi, and F. Baletto, "Metallic nanoparticles meet metadynamics," *Journal of Chemical Physics*, vol. 143, no. 18, pp. 1–7, 2015.

- [18] M. Vopsaroiu, M. J. Thwaites, G. V. Fernandez, S. Lepadatu, and K. O’Grady, “Grain size effects in metallic thin films prepared using a new sputtering technology,” *Journal of Optoelectronics and Advanced Materials*, vol. 7, no. 5, pp. 2713–2720, 2005.
- [19] S. Yatsuya, T. Kamakura, K. Yamauchi, and K. Mihama, “A new technique for the formation of ultrafine particles by sputtering,” *Japanese Journal of Applied Physics*, vol. 25, no. 1, pp. L42–L44, 1986.
- [20] K. J. Hu, S. R. Plant, P. R. Ellis, C. M. Brown, P. T. Bishop, and R. E. Palmer, “The effects of 1-pentyne hydrogenation on the atomic structures of size-selected AuN and PdN ($N = 923$ and 2057) nanoclusters,” *Physical Chemistry Chemical Physics*, vol. 16, no. 48, pp. 26631–26637, 2014.
- [21] S. R. Plant, L. Cao, and R. E. Palmer, “Atomic structure control of size-selected gold nanoclusters during formation,” *Journal of the American Chemical Society*, vol. 136, no. 21, pp. 7559–7562, 2014.
- [22] B. Von Issendorff and R. E. Palmer, “A new high transmission infinite range mass selector for cluster and nanoparticle beams,” *Review of Scientific Instruments*, vol. 70, no. 12, pp. 4497–4501, 1999.
- [23] P. R. Ellis, C. M. Brown, P. T. Bishop, J. Yin, K. Cooke, W. D. Terry, J. Liu, F. Yin, and R. E. Palmer, “The cluster beam route to model catalysts and beyond,” *Faraday Discussions*, vol. 188, pp. 39–56, 2016.
- [24] R. Cai, P. R. Ellis, J. Yin, J. Liu, C. M. Brown, R. Griffin, G. Chang, D. Yang, J. Ren, K. Cooke, P. T. Bishop, W. Theis, and R. E. Palmer, “Performance of Preformed Au/Cu Nanoclusters Deposited on MgO Powders in the Catalytic Reduction of 4-Nitrophenol in Solution,” *Small*, vol. 14, no. 13, pp. 1–10, 2018.
- [25] B. N. Chichkov, C. Momma, S. Nolte, F. von Alvensleben, and A. Tünnermann, “Femtosecond, picosecond and nanosecond laser ablation of solids,” *Applied Physics A: Materials Science & Processing*, vol. 63, no. 2, pp. 109–115, 1996.
- [26] S. Hamad, G. K. Podagatlapalli, V. S. Vendamani, S. V. Nageswara Rao, A. P. Pathak, S. P. Tewari, and S. Venugopal Rao, “Femtosecond ablation of silicon in acetone: Tunable photoluminescence from generated nanoparticles and fabrication of surface nanostructures,” *Journal of Physical Chemistry C*, vol. 118, no. 13, pp. 7139–7151, 2014.

- [27] S. Vučković, M. Svanqvist, and V. N. Popok, “Laser ablation source for formation and deposition of size-selected metal clusters,” *Review of Scientific Instruments*, vol. 79, no. 7, 2008.
- [28] J. Zhang, G. Chen, M. Chaker, F. Rosei, and D. Ma, “Gold nanoparticle decorated ceria nanotubes with significantly high catalytic activity for the reduction of nitrophenol and mechanism study,” *Applied Catalysis B: Environmental*, vol. 132-133, pp. 107–115, 2013.
- [29] L. Cao, *Lu’s Thesis*. PhD thesis, University of Birmingham, 2016.
- [30] W. Terry, *Cluster Production in the Matrix Assembly Cluster Source*. PhD thesis, University of Birmingham, 2016.
- [31] R. E. Palmer, L. Cao, and F. Yin, “Note: Proof of principle of a new type of cluster beam source with potential for scale-up,” *Review of Scientific Instruments*, vol. 87, no. 4, pp. 1–046103, 2016.
- [32] P. Sigmund, “Theory of Sputtering. I. Sputtering Yield of Amorphous and Polycrystalline Targets,” *Physical Review*, vol. 184, no. 2, pp. 383–416, 1969.
- [33] R. S. Nelson, “An investigation of thermal spikes by studying the high energy sputtering of metals at elevated temperatures,” *Philosophical Magazine*, vol. 11, no. 110, pp. 291–302, 1965.
- [34] A. M. Reddy, A. S. Reddy, K. S. Lee, and P. S. Reddy, “Growth and characterization of NiO thin films prepared by dc reactive magnetron sputtering,” *Solid State Sciences*, vol. 13, no. 2, pp. 314–320, 2011.
- [35] L. Wang, C. Gu, X. Ge, J. Zhang, H. Zhu, and J. Tu, “Highly Efficient Bifunctional Catalyst of NiCo₂O₄@NiO@Ni Core/Shell Nanocone Array for Stable Overall Water Splitting,” *Particle and Particle Systems Characterization*, vol. 34, no. 11, pp. 1–9, 2017.
- [36] B. Zhu, I. C. Ouz, and H. Guesmi, “Investigation of finite-size effects in chemical bonding of AuPd nanoalloys,” *Journal of Chemical Physics*, vol. 143, no. 14, 2015.
- [37] C. Cheng, X. Zhang, M. Wang, S. Wang, and Z. Yang, “Single Pd atomic catalyst on Mo₂CO₂ monolayer (MXene): Unusual activity for CO oxidation by trimolecular Eley-Rideal mechanism,” *Physical Chemistry Chemical Physics*, vol. 20, no. 5, pp. 3504–3513, 2018.

- [38] D. M. Foster, R. Ferrando, and R. E. Palmer, “Experimental determination of the energy difference between competing isomers of deposited, size-selected gold nanoclusters,” *Nature Communications*, vol. 9, no. 1, 2018.
- [39] C. D. Chudasama, J. Sebastian, and R. V. Jasra, “Pore-size engineering of zeolite A for the size/shape selective molecular separation,” *Industrial and Engineering Chemistry Research*, vol. 44, no. 6, pp. 1780–1786, 2005.
- [40] J. M. Bolivar, I. Eisl, and B. Nidetzky, “Advanced characterization of immobilized enzymes as heterogeneous biocatalysts,” *Catalysis Today*, vol. 259, pp. 66–80, 2016.
- [41] A. Biabani-Ravandi, M. Rezaei, and Z. Fattah, “Catalytic performance of Ag/Fe₂O₃ for the low temperature oxidation of carbon monoxide,” *Chemical Engineering Journal*, vol. 219, pp. 124–130, 2013.
- [42] Y. G. Wang, D. C. Cantu, M. S. Lee, J. Li, V. A. Glezakou, and R. Rousseau, “CO Oxidation on Au/TiO₂: Condition-Dependent Active Sites and Mechanistic Pathways,” *Journal of the American Chemical Society*, vol. 138, no. 33, pp. 10467–10476, 2016.
- [43] P. Aich, H. Wei, B. Basan, A. J. Kropf, N. M. Schweitzer, C. L. Marshall, J. T. Miller, and R. Meyer, “Single-Atom Alloy Pd-Ag Catalyst for Selective Hydrogenation of Acrolein,” *Journal of Physical Chemistry C*, vol. 119, no. 32, pp. 18140–18148, 2015.
- [44] M. Haruta, N. Yamada, T. Kobayashi, and S. Iijima, “Gold catalysts prepared by coprecipitation for low-temperature oxidation of hydrogen and of carbon monoxide,” *Journal of Catalysis*, vol. 115, no. 2, pp. 301–309, 1989.
- [45] C. M. Aikens, “Modelling small gold and silver nanoparticles with electronic structure methods,” *Molecular Simulation*, vol. 38, no. 8-9, pp. 607–614, 2012.
- [46] D. Teschner, E. Vass, M. Hävecker, S. Zafeirotos, P. Schnörch, H. Sauer, A. Knop-Gericke, R. Schlögl, M. Chamam, A. Wootsch, A. S. Canning, J. J. Gamman, S. D. Jackson, J. McGregor, and L. F. Gladden, “Alkyne hydrogenation over Pd catalysts: A new paradigm,” *Journal of Catalysis*, vol. 242, no. 1, pp. 26–37, 2006.

- [47] S. D. Jackson, C. A. Hamilton, G. J. Kelly, and D. De Bruin, "The hydrogenation of C-5 alkynes over palladium catalysts," *Reaction Kinetics and Catalysis Letters*, vol. 73, no. 1, pp. 77–82, 2001.
- [48] I. Z. Jones, R. A. Bennett, and M. Bowker, "CO oxidation on Pd(110): a high-resolution XPS and molecular beam study," *Surface Science*, vol. 439, no. 1-3, pp. 235–248, 1999.
- [49] B. M. Weiss and E. Iglesia, "Mechanism and site requirements for NO oxidation on Pd catalysts," *Journal of Catalysis*, vol. 272, no. 1, pp. 74–81, 2010.
- [50] K. Suttiponparnit, J. Jiang, M. Sahu, S. Suvachittanont, T. Charinpanitkul, and P. Biswas, "Role of Surface Area, Primary Particle Size, and Crystal Phase on Titanium Dioxide Nanoparticle Dispersion Properties," *Nanoscale Research Letters*, vol. 6, no. 1, pp. 1–8, 2011.
- [51] A. Satsuma, M. Yanagihara, K. Osaki, Y. Saeki, H. Liu, Y. Yamamoto, S. Arai, and J. Ohyama, "Promotion of low-temperature oxidation of CO over Pd supported on titania-coated ceria," *RSC Advances*, vol. 4, no. 97, pp. 54187–54193, 2014.
- [52] D. Widmann, A. Krautsieder, P. Walter, A. Brückner, and R. J. Behm, "How temperature affects the mechanism of CO oxidation on Au/TiO₂: A combined EPR and TAP reactor study of the reactive removal of TiO₂ surface lattice oxygen in Au/TiO₂ by CO," *ACS Catalysis*, vol. 6, no. 8, pp. 5005–5011, 2016.
- [53] J. H. Den Otter, S. R. Nijveld, and K. P. De Jong, "Synergistic Promotion of Co/SiO₂ Fischer-Tropsch Catalysts by Niobia and Platinum," *ACS Catalysis*, vol. 6, no. 3, pp. 1616–1623, 2016.
- [54] G. Korotcenkov, V. Brinzari, and B. K. Cho, "What restricts gold clusters reactivity in catalysis and gas sensing effects: A focused review," *Materials Letters*, vol. 147, pp. 101–104, 2015.
- [55] M. Centeno, C. Portales, I. Carrizosa, and J. A. Odriozola, "Gold supported CeO₂/Al₂O₃ catalysts for CO oxidation: Influence of the ceria phase," *Catalysis Letters*, vol. 102, no. 3-4, pp. 289–297, 2005.
- [56] Z. Y. Deng, T. Fukasawa, M. Ando, G. J. Zhang, and T. Ohji, "High-Surface-Area Alumina Ceramics Fabricated by the Decomposition of Al(OH)₃," *Journal of the American Ceramic Society*, vol. 84, no. 3, pp. 485–491, 2001.

- [57] L. Qi and J. Li, “Adsorbate interactions on surface lead to a flattened Sabatier volcano plot in reduction of oxygen,” *Journal of Catalysis*, vol. 295, pp. 59–69, 2012.
- [58] H. J. Freund, G. Meijer, M. Scheffler, R. Schlögl, and M. Wolf, “CO oxidation as a prototypical reaction for heterogeneous processes,” *Angewandte Chemie - International Edition*, vol. 50, no. 43, pp. 10064–10094, 2011.
- [59] G. Avgouropoulos, T. Ioannides, C. Papadopoulou, J. Batista, S. Hocevar, and H. K. Matralis, “A comparative study of Pt/ γ -Al₂O₃, Au/ α -Fe₂O₃ and CuO-CeO₂ catalysts for the selective oxidation of carbon monoxide in excess hydrogen,” *Catalysis Today*, vol. 75, no. 1–4, pp. 157–167, 2002.
- [60] M. Haruta, “When gold is not noble: Catalysis by nanoparticles,” *Chemical Record*, vol. 3, no. 2, pp. 75–87, 2003.
- [61] T. Engel and G. Ertl, “A molecular beam investigation of the catalytic oxidation of CO on Pd (111),” *The Journal of Chemical Physics*, vol. 69, no. 3, pp. 1267–1281, 1978.
- [62] T. Schalow, B. Brandt, M. Laurin, S. Schauermaun, J. Libuda, and H. J. Freund, “CO oxidation on partially oxidized Pd nanoparticles,” *Journal of Catalysis*, vol. 242, no. 1, pp. 58–70, 2006.
- [63] T. Schalow, B. Brandt, M. Laurin, S. Schauermaun, S. Guimond, H. Kuhlenbeck, J. Libuda, and H. J. Freund, “Formation of interface and surface oxides on supported Pd nanoparticles,” *Surface Science*, vol. 600, no. 12, pp. 2528–2542, 2006.
- [64] T. Schalow, B. Brandt, D. E. Starr, M. Laurin, S. K. Shaikhutdinov, S. Schauermaun, J. Libuda, and H. J. Freund, “Particle size dependent adsorption and reaction kinetics on reduced and partially oxidized Pd nanoparticles,” *Physical Chemistry Chemical Physics*, vol. 9, no. 11, pp. 1347–1361, 2007.
- [65] A. Satsuma, K. Osaki, M. Yanagihara, J. Ohyama, and K. Shimizu, “Activity controlling factors for low-temperature oxidation of CO over supported Pd catalysts,” *Applied Catalysis B: Environmental*, vol. 132–133, pp. 511–518, 2013.

- [66] P. Hervés, M. Pérez-Lorenzo, L. M. Liz-Marzán, J. Dzubiella, Y. Lu, and M. Ballauff, “Catalysis by metallic nanoparticles in aqueous solution: Model reactions,” *Chemical Society Reviews*, vol. 41, no. 17, pp. 5577–5587, 2012.
- [67] S. Wunder, F. Polzer, Y. Lu, Y. Mei, and M. Ballauff, “Kinetic analysis of catalytic reduction of 4-nitrophenol by metallic nanoparticles immobilized in spherical polyelectrolyte brushes,” *Journal of Physical Chemistry C*, vol. 114, no. 19, pp. 8814–8820, 2010.
- [68] Y. Khalavka, J. Becker, and C. Sönnichsen, “Synthesis of rod-shaped gold nanorattles with improved plasmon sensitivity and catalytic activity,” *Journal of the American Chemical Society*, vol. 131, no. 5, pp. 1871–1875, 2009.
- [69] M. Guo, J. He, Y. Li, S. Ma, and X. Sun, “One-step synthesis of hollow porous gold nanoparticles with tunable particle size for the reduction of 4-nitrophenol,” *Journal of Hazardous Materials*, vol. 310, pp. 89–97, 2016.
- [70] T. Aditya, A. Pal, and T. Pal, “Nitroarene reduction: A trusted model reaction to test nanoparticle catalysts,” *Chemical Communications*, vol. 51, no. 46, pp. 9410–9431, 2015.
- [71] A. N. R. Bos, E. Hof, and W. Kuper, “THE BEHAVIOUR OF A SINGLE CATALYST PELLET FOR THE SELECTIVE HYDROGENATION OF ETHYNE IN ETHENE,” *Chemical Engineering Science*, vol. 48, no. 11, pp. 1959–1969, 1993.
- [72] A. L. Bugaev, O. A. Usoltsev, A. A. Guda, K. A. Lomachenko, I. A. Pankin, Y. V. Rusalev, H. Emerich, E. Groppo, R. Pellegrini, A. V. Soldatov, J. A. Van Bokhoven, and C. Lamberti, “Palladium Carbide and Hydride Formation in the Bulk and at the Surface of Palladium Nanoparticles,” *Journal of Physical Chemistry C*, vol. 122, no. 22, pp. 12029–12037, 2018.
- [73] N. R. Sassen, A. J. Den Hartog, F. Jongerius, J. F. Aarts, and V. Ponec, “Adsorption and reactions of ethyne: Effects of modifiers and formation of bimetallics,” *Faraday Discussions of the Chemical Society*, vol. 87, pp. 311–320, 1989.
- [74] G. Webb, “The formation and role of carbonaceous residues in metal-catalysed reactions of hydrocarbons,” *Catalysis Today*, vol. 7, no. 2, pp. 139–155, 1990.

- [75] A. S. Al-Ammar and G. Webb, "Hydrogenation of Acetylene over Supported Metal Catalysts," *Journal of the Chemical Society, Faraday Transactions 1: Physical Chemistry in Condensed Phases*, vol. 74, no. 74, pp. 195–205, 1977.
- [76] D. R. Kennedy, G. Webb, S. D. Jackson, and D. Lennon, "Propyne hydrogenation over alumina-supported palladium and platinum catalysts," *Applied Catalysis A: General*, vol. 259, no. 1, pp. 109–120, 2004.
- [77] C. Mottet, J. Goniakowski, F. Baletto, R. Ferrando, and G. Treglia, "Modeling free and supported metallic nanoclusters: Structure and dynamics," *Phase Transitions*, vol. 77, no. 1-2, pp. 101–113, 2004.
- [78] T. Kawasaki, T. Miura, Z. Cui, and T. Tanji, "Environmental TEM Observation of Deformations of Catalytic Gold Nanoparticles under Reaction Gas Condition," *Microscopy and Microanalysis*, vol. 18, no. S2, pp. 1182–1183, 2012.
- [79] J. E. Greene, "Review Article: Tracing the recorded history of thin-film sputter deposition: From the 1800s to 2017," *Journal of Vacuum Science & Technology A: Vacuum, Surfaces, and Films*, vol. 35, no. 5, p. 05C204, 2017.
- [80] J. E. Greene, "Tracing the 5000-year recorded history of inorganic thin films from 3000 BC to the early 1900s AD," *Applied Physics Reviews*, vol. 1, no. 4, p. 041302, 2014.
- [81] W. R. Grove, "On the electrolysis of gases," *Nature*, vol. 52, no. 1349, pp. 451–455, 1895.
- [82] T. Edison, "Art of Plating one Material With Another," 1894.
- [83] J. P. Wilcoxon and P. P. Provencio, "Heterogeneous growth of metal clusters solutions of seed nanoparticles," *Journal of the American Chemical Society*, vol. 126, no. 20, pp. 6402–6408, 2004.
- [84] N. Lümmen and T. Kraska, "Homogeneous nucleation of iron from supersaturated vapor investigated by molecular dynamics simulation," *Journal of Aerosol Science*, vol. 36, no. 12, pp. 1409–1426, 2005.
- [85] K. H. Heinig, T. Müller, B. Schmidt, M. Strobel, and W. Möller, "Interfaces under ion irradiation: Growth and taming of nanostructures," *Applied Physics A: Materials Science and Processing*, vol. 77, no. 1, pp. 17–25, 2003.

- [86] J. A. Venables, G. D. Spiller, and M. Hanbucken, "Nucleation and growth of thin films," *Reports on Progress in Physics*, vol. 47, no. 4, pp. 399–459, 1984.
- [87] R. Collette, Y. Wu, A. Olafsson, J. P. Camden, and P. D. Rack, "Combinatorial Thin Film Sputtering AuxAl_{1-x} Alloys: Correlating Composition and Structure with Optical Properties," *ACS Combinatorial Science*, vol. 20, no. 11, pp. 633–642, 2018.
- [88] H. Sato, T. Minami, S. Takata, and T. Yamada, "Transparent conducting p-type NiO thin films prepared by magnetron sputtering," *Thin Solid Films*, vol. 236, no. 1-2, pp. 27–31, 1993.
- [89] U. Diebold, J. M. Pan, and T. E. Madey, "Ultrathin metal film growth on TiO₂(110): an overview," *Surface Science*, vol. 331-333, no. PART B, pp. 845–854, 1995.
- [90] M. Haruta, "Spiers Memorial Lecture: Role of perimeter interfaces in catalysis by gold nanoparticles," *Faraday Discussions*, vol. 152, pp. 11–32, 2011.
- [91] V. K. Guda, P. H. Steele, V. K. Penmetsa, and Q. Li, "Fast Pyrolysis of Biomass: Recent Advances in Fast Pyrolysis Technology," *Recent Advances in Thermochemical Conversion of Biomass*, pp. 177–211, 1 2015.
- [92] D. M. Baechle, J. D. Demaree, J. K. Hirvonen, and E. D. Wetzel, "Magnetron sputter deposition onto fluidized particle beds," *Surface and Coatings Technology*, vol. 221, pp. 94–103, 2013.
- [93] N. Kanbe, Y. Tomikawa, and T. Takano, "Powder-feeding device using hollow cylindrical piezoelectric ceramics," *Japanese Journal of Applied Physics*, vol. 32, no. 5S, pp. 2405–2407, 1993.
- [94] A. Nagy, A. Bortolon, D. M. Mauzey, E. Wolfe, E. P. Gilson, R. Lunsford, R. Maingi, D. K. Mansfield, R. Nazikian, and A. L. Roquemore, "A multi-species powder dropper for magnetic fusion applications," *Review of Scientific Instruments*, vol. 89, no. 10, 2018.
- [95] P. Bidare, R. R. Maier, R. J. Beck, J. D. Shephard, and A. J. Moore, "An open-architecture metal powder bed fusion system for in-situ process measurements," *Additive Manufacturing*, vol. 16, pp. 177–185, 2017.

- [96] M. Mracek and J. Wallaschek, “A system for powder transport based on piezoelectrically excited ultrasonic progressive waves,” *Materials Chemistry and Physics*, vol. 90, no. 2-3, pp. 378–380, 2005.
- [97] G. Xu, P. Lu, M. Li, C. Liang, P. Xu, D. Liu, and X. Chen, “Investigation on characterization of powder flowability using different testing methods,” *Experimental Thermal and Fluid Science*, vol. 92, no. October 2017, pp. 390–401, 2018.
- [98] S. Robinson and R. Kaufman, “Broad-beam ion source technology and applications,” *Microelectronics Reliability*, vol. 30, no. 5, p. 1016, 1990.
- [99] W. Ensinger, “Ion sources for ion beam assisted thin-film deposition,” *Review of Scientific Instruments*, vol. 63, no. 11, pp. 5217–5233, 1992.
- [100] C. D. Child, “Discharge from hot platinum wires,” *Science*, vol. 15, no. 379, pp. 553–554, 1902.
- [101] Z. Li, *Scanning transmission electron microscopy studies of mono- and bimetallic nanoclusters*, vol. 3. Elsevier Ltd, 1 ed., 2012.
- [102] G. Nageswaran, Y. S. Choudhary, and S. Jagannathan, “Inductively Coupled Plasma Mass Spectrometry,” *Spectroscopic Methods for Nanomaterials Characterization*, vol. 2, pp. 163–194, 2017.
- [103] R. Gilstrap, *A colloidal nanoparticle form of indium tin oxide : system development and characterization SYSTEM DEVELOPMENT AND CHARACTERIZATION Presented to The Academic Faculty by Richard Allen Gilstrap Jr . In Partial Fulfillment of the Requirements for the Degree*. PhD thesis, Georgia Institute of Technology, 2018.
- [104] M. Moldovan, E. M. Krupp, A. E. Holliday, and O. F. Donard, “High resolution sector field ICP-MS and multicollector ICP-MS as tools for trace metal speciation in environmental studies: A review,” *Journal of Analytical Atomic Spectrometry*, vol. 19, no. 7, pp. 815–822, 2004.
- [105] S. Stuckenholtz, C. Büchner, H. Ronneburg, G. Thielsch, M. Heyde, and H. J. Freund, “Apparatus for low temperature thermal desorption spectroscopy of portable samples,” *Review of Scientific Instruments*, vol. 87, no. 4, 2016.
- [106] M. B. Fichtl and O. Hinrichsen, “On the temperature programmed desorption of hydrogen from polycrystalline copper,” *Catalysis Letters*, vol. 144, no. 12, pp. 2114–2120, 2014.

- [107] P. a. Webb, "Introduction to Chemical Adsorption Analytical Techniques and their Applications to Catalysis," *MIC Technical Publications*, vol. 13, no. January, pp. 1–4, 2003.
- [108] I. N. B. Ahrlund, S. Grenthe, "Acta_Vol_14.P1059-1076.Pdf," *Acta Chemica Scandinavia*, vol. 1, no. 14, pp. 1059–1076, 1960.
- [109] G. W. Sears, "Determination of Specific Surface Area of Colloidal Silica by Titration With Sodium Hydroxide," *Analytical Chemistry*, vol. 28, no. 12, pp. 1981–1983, 1956.
- [110] S. Ivanova, V. Pitchon, Y. Zimmermann, and C. Petit, "Preparation of alumina supported gold catalysts: Influence of washing procedures, mechanism of particles size growth," *Applied Catalysis A: General*, vol. 298, no. 1-2, pp. 57–64, 2006.
- [111] A. J. Perez-Unzueta, J. H. Beynon, and M. G. Gee, "Effects of surrounding atmosphere on the wear of sintered alumina," *Wear*, vol. 146, no. 1, pp. 179–196, 1991.
- [112] M. G. Gee, "The formation of aluminium hydroxide in the sliding wear of alumina," *Wear*, vol. 153, no. 1, pp. 201–227, 1992.
- [113] M. Bowker, A. Nuhu, and J. Soares, "High activity supported gold catalysts by incipient wetness impregnation," *Catalysis Today*, vol. 122, no. 3-4, pp. 245–247, 2007.
- [114] S. D. Lin, M. Bollinger, and M. A. Vannice, "Low temperature CO oxidation over Au/TiO₂ and Au/SiO₂ catalysts," *Catalysis Letters*, vol. 17, no. 3-4, pp. 245–262, 1993.
- [115] A. S. Ivanova, E. M. Slavinskaya, R. V. Gulyaev, V. I. Zaikovskii, O. A. Stonkus, I. G. Danilova, L. M. Plyasova, I. A. Polukhina, and A. I. Boronin, "Metal-support interactions in Pt/Al₂O₃ and Pd/Al₂O₃ catalysts for CO oxidation," *Applied Catalysis B: Environmental*, vol. 97, no. 1-2, pp. 57–71, 2010.
- [116] F. Rumpf, H. Poppa, and M. Boudart, "Oxidation of Carbon Monoxide on Palladium: Role of The Alumina Support," *Langmuir*, vol. 4, no. 3, pp. 722–728, 1988.
- [117] G. A. Somorjai, A. M. Contreras, M. Montano, and R. M. Rioux, "Clusters, surfaces, and catalysis," *Proceedings of the National Academy of Sciences of the United States of America*, vol. 103, no. 28, pp. 10577–10583, 2006.

- [118] P. Deka, R. C. Deka, and P. Bharali, "In situ generated copper nanoparticle catalyzed reduction of 4-nitrophenol," *New Journal of Chemistry*, vol. 38, no. 4, pp. 1789–1793, 2014.
- [119] H. Wang, X. K. Gu, X. Zheng, H. Pan, J. Zhu, S. Chen, L. Cao, W. X. Li, and J. Lu, "Disentangling the size-dependent geometric and electronic effects of palladium nanocatalysts beyond selectivity," *Science Advances*, vol. 5, no. 1, pp. 1–9, 2019.
- [120] H. L. Jiang, T. Akita, T. Ishida, M. Haruta, and Q. Xu, "Synergistic catalysis of Au@Ag core-shell nanoparticles stabilized on metal-organic framework," *Journal of the American Chemical Society*, vol. 133, no. 5, pp. 1304–1306, 2011.
- [121] D. Belić, R. L. Chantry, Z. Y. Li, and S. A. Brown, "Ag-Au nanoclusters: Structure and phase segregation," *Applied Physics Letters*, vol. 99, no. 17, pp. 28–31, 2011.
- [122] T. W. Liao, A. Yadav, K. J. Hu, J. Van Der Tol, S. Cosentino, F. D'Acapito, R. E. Palmer, C. Lenardi, R. Ferrando, D. Grandjean, and P. Lievens, "Unravelling the nucleation mechanism of bimetallic nanoparticles with composition-tunable core-shell arrangement," *Nanoscale*, vol. 10, no. 14, pp. 6684–6694, 2018.
- [123] S. Matsusaka, M. Urakawa, and H. Masuda, "Micro-feeding of fine powders using a capillary tube with ultrasonic vibration," *Advanced Powder Technology*, vol. 6, no. 4, pp. 283–293, 1995.
- [124] Y. Yang and X. Li, "Experimental and analytical study of ultrasonic micro powder feeding," *Journal of Physics D: Applied Physics*, vol. 36, no. 11, pp. 1349–1354, 2003.
- [125] M. Miura, T. Tsuda, T. Satoh, S. Pivsa-Art, and M. Nomura, "Oxidative Cross-Coupling of N-(2-Phenylphenyl)benzene-sulfonamides or Benzoic and Naphthoic Acids with Alkenes Using a Palladium-Copper Catalyst System under Air," *Journal of Organic Chemistry*, vol. 63, no. 15, pp. 5211–5215, 1998.
- [126] M. Gholinejad, N. Jeddi, and B. Pullithadathil, "Agarose functionalized phosphorus ligand for stabilization of small-sized palladium and copper nanoparticles: Efficient heterogeneous catalyst for Sonogashira reaction," *Tetrahedron*, vol. 72, no. 19, pp. 2491–2500, 2016.

- [127] M. Khanuja, B. R. Mehta, and S. M. Shivaprasad, "Two approaches for enhancing the hydrogenation properties of palladium: Metal nanoparticle and thin film over layers," *Journal of Chemical Sciences*, vol. 120, no. 6, pp. 573–578, 2008.
- [128] J. P. Boitiaux, J. Cosyns, and S. Vasudevan, "Hydrogenation of highly unsaturated hydrocarbons over highly dispersed palladium catalyst. Part I: behaviour of small metal particles," *Applied Catalysis*, vol. 6, no. 1, pp. 41–51, 1983.
- [129] T. Fu, T. Wang, H. Sun, Y. Xu, Z. Dong, X. Guo, L. Peng, Y. Zhu, Z. Chen, and W. Ding, "Carbon nitride with encapsulated nickel for semi-hydrogenation of acetylene: pyridinic nitrogen is responsible for hydrogen dissociative adsorption," *Science China Chemistry*, vol. 61, no. 8, pp. 1014–1019, 2018.
- [130] H. Park, D. A. Reddy, Y. Kim, S. Lee, R. Ma, M. Lim, and T. K. Kim, "Hydrogenation of 4-nitrophenol to 4-aminophenol at room temperature: Boosting palladium nanocrystals efficiency by coupling with copper via liquid phase pulsed laser ablation," *Applied Surface Science*, vol. 401, pp. 314–322, 2017.
- [131] S. Pétigny, B. Domenichini, H. Mostéfa-Sba, E. Lesniewska, A. Steinbrunn, and S. Bourgeois, "Molybdenum deposition on TiO₂ (110) surfaces with different stoichiometries," *Applied Surface Science*, vol. 142, no. 1, pp. 114–119, 1999.
- [132] Z. Jiang, W. Huang, Z. Zhang, H. Zhao, D. Tan, and X. Bao, "Molybdenum deposition on the thin alumina film: A combinatorial investigation by HREELS, XPS and UPS," *Chemical Physics Letters*, vol. 439, no. 4-6, pp. 313–317, 2007.
- [133] M. Neurock, "First-principles analysis of the hydrogenation of carbon monoxide over palladium," *Topics in Catalysis*, vol. 9, no. 3-4, pp. 135–152, 1999.
- [134] T. K. Yamada Taro, Onishi Takaharu, "Adsorption-desorption kinetics of carbon monoxide on palladium polycrystalline surfaces," *Surface Science*, vol. 133, pp. 533–546, 1983.
- [135] Y. T. Wong and R. Hoffmann, "Chemisorption of carbon monoxide on three metal surfaces: nickel(111), palladium(111), and platinum(111): a comparative study," *The Journal of Physical Chemistry*, vol. 95, no. 2, pp. 859–867, 1991.

- [136] R. J. Behm, K. Christmann, and G. Ertl, "Adsorption of hydrogen on Pd(100)," *Surface Science*, vol. 99, no. 2, pp. 320–340, 1980.
- [137] I. Witońska, S. Karski, M. Frajtek, N. Krawczyk, and A. Królak, "Temperature-programmed desorption of H₂ from the surfaces of Pd/support and Pd-Ag/support catalysts (support = Al₂O₃, SiO₂)," *Reaction Kinetics and Catalysis Letters*, vol. 93, no. 2, pp. 241–248, 2008.
- [138] K. J. Leary, J. N. Michaels, and A. M. Stacy, "Penetration of Hydrogen into Subsurface Sites of Silica-Supported Palladium during Temperature-Programmed Desorption," *Langmuir*, vol. 4, no. 6, pp. 1251–1257, 1988.
- [139] D. Jose and B. R. Jagirdar, "Nature of hydrogen atom trapped inside palladium lattice," *International Journal of Hydrogen Energy*, vol. 35, no. 13, pp. 6804–6811, 2010.
- [140] S. P. Chakraborty, S. Banerjee, I. G. Sharma, and A. K. Suri, "Development of silicide coating over molybdenum based refractory alloy and its characterization," *Journal of Nuclear Materials*, vol. 403, no. 1-3, pp. 152–159, 2010.
- [141] S. Gholhaki, S. H. Hung, D. J. Cant, C. E. Blackmore, A. G. Shard, Q. Guo, K. P. McKenna, and R. E. Palmer, "Exposure of mass-selected bimetallic Pt-Ti nanoalloys to oxygen explored using scanning transmission electron microscopy and density functional theory," *RSC Advances*, vol. 8, no. 48, pp. 27276–27282, 2018.
- [142] J. Laskin, G. E. Johnson, and V. Prabhakaran, "Soft Landing of Complex Ions for Studies in Catalysis and Energy Storage," *Journal of Physical Chemistry C*, vol. 120, no. 41, pp. 23305–23322, 2016.
- [143] M. Yamauchi, R. Ikeda, H. Kitagawa, and M. Takata, "Nanosize effects on hydrogen storage in palladium," *Journal of Physical Chemistry C*, vol. 112, no. 9, pp. 3294–3299, 2008.
- [144] T. Fujitani, I. Nakamura, T. Akita, M. Okumura, and M. Haruta, "Hydrogen dissociation by gold clusters," *Angewandte Chemie - International Edition*, vol. 48, no. 50, pp. 9515–9518, 2009.